COMPUTATION OF STEADY AND UNSTEADY
QUASI—ONE—DIMENSIONAL VISCOUS/INVISCID INTERACTING
INTERNAL FLOWS AT SUBSONIC, TRANSONIC, AND SUPERSONIC
MACH NUMBERS

eirs

ENGINEERING & INDUSTRIAL RESEARCH STATION

By

TIMOTHY W. SWAFFORD
DAVID H. HUDDLESTON
JUDY A. BUSBY
AND
B. LAWRENCE CHESSER

NSF ENGINEERING RESEARCH CENTER FOR COMPUTATIONAL FIELD SIMULATION
MISSISSIPPI STATE UNIVERSITY

JUNE 1992

MSSU-EIRS-ERC-92-1

COMPUTATION OF STEADY AND UNSTEADY QUASI-ONE-DIMENSIONAL VISCOUS/INVISCID INTERACTING INTERNAL FLOWS AT SUBSONIC, TRANSONIC, AND SUPERSONIC MACH NUMBERS

by

Timothy W. Swafford
David H. Huddleston
Judy A. Busby
and
B. Lawrence Chesser

Engineering Research Center for Computational Field Simulation
Mississippi State University

FINAL REPORT

June 1992

TABLE OF CONTENTS

ACKNOWLEDGEMENTS

ABSTRACT

Computations of viscous–inviscid interacting internal flowfields are presented for steady and unsteady quasi–one–dimensional (Q1D) test cases. The unsteady Q1D Euler equations are coupled with integral boundary–layer equations for unsteady, two–dimensional (planar or axisymmetric), turbulent flow over impermeable, adiabatic walls. The coupling methodology differs from that used in most techniques reported previously in that the above mentioned equation sets are written as a complete system and solved simultaneously; that is, the coupling is carried out directly through the equations as opposed to coupling the solutions of the different equation sets. Solutions to the coupled system of equations are obtained using both explicit and implicit numerical schemes for steady subsonic, steady transonic, and both steady and unsteady supersonic internal flowfields. Computed solutions are compared with measurements as well as Navier–Stokes and inverse boundary–layer methods. An analysis of the eigenvalues of the coefficient matrix associated with the quasi–linear form of the coupled system of equations indicates the presence of complex eigenvalues for certain flow conditions. It is concluded that although reasonable solutions can be obtained numerically, these complex eigenvalues contribute to the overall difficulty in obtaining numerical solutions to the coupled system of equations.

I. INTRODUCTION

The study and analysis of internal flows has received significant attention over the past several decades because the operation of many physical devices, particularly regarding aerospace–related hardware, depend upon proper designs to achieve near–optimum operating characteristics. Examples of such devices include any configuration where the flow is confined and an exchange between pressure and kinetic energy is desired (engine inlets, wind tunnel diffusers, rocket nozzles, etc.). There devices can be geometrically complex as well as very viscous–flow dominated. Moreover, certain configurations and conditions can result in unsteady flow (e.g., inlet buzz).

In the past, the design of these devices has, for the large part, depended upon empirically based methodologies. More recently, computational techniques have played an increasingly important role in the design process as hardware becomes less conservative and is required to operate "near the edge" of the design envelop. As evidenced above, perhaps the most important physical flowfield characteristics which need to be considered when attempting to computationally address internal flows are effects associated with unsteadiness, viscosity, and multi–dimensions. Of course, the relative contributions of these effects are dependent upon the geometry as well as which physical flowfield parameters are required to provide the "answers" for a given problem. For example, if the performance (e.g., static pressure rise) of a subsonic axisymmetric diffuser is desired, it is very important that viscous effects be well represented because diffuser performance is very sensitive, for example, to the incoming blockage caused by the presence of the boundary layer. For this case, it can be argued that unsteadiness and multidimensional effects play a secondary role. However, for cases where boundary–layer separation is possible, significant unsteadiness may be present. For these cases the capability to capture this unsteadiness within computation is important in order to gain engineering insight into the physics. On the other hand, it is easy to identify cases where all of the above effects play an important part in shaping the overall flowfield structure (e.g., a moving shock within an S–shaped, asymmetric duct).

A thorough computational investigation of flowfields of this type requires solution of the full Reynolds–averaged, multidimensional, time–dependent, Navier–Stokes equations. Of course, solu-

tion of these equations produces essentially all pertinent flowfield parameters. Therefore, assuming that these solutions are of acceptable accuracy, it possible to perform parametric studies of a proposed geometry/flowfield combination which could be used to significantly reduce the risk associated with new hardware design. Unfortunately, obtaining numerical solutions to these equations for complex geometries and unsteady flowfields is expensive and time–consuming, even using today's largest and fastest supercomputers. Therefore, it is important to investigate alternative means of performing compute–based parametric studies of proposed new hardware designs. However, it is equally important that these alternative techniques be capable of capturing as much of the critical physics as possible to avoid "throwing the baby out with the bath water." Consequently, identifying the physical aspects which tend to dominate the behavior of the flowfield associated with a particular geometry is vital to the success of the alternative computational procedure.

It is obvious that some compromises must be made to reduce these computational requirements while simultaneously retaining the desired physics. Deciding upon which compromise requires answering the following question: "What are desired physics?" or stated another way, "Which physical flowfield characteristics are we willing to approximate in order to reduce the overall computational resource demands?" Unfortunately, the answer to either question is very problem dependent. For example, elimination of viscosity effects from the Navier–Stokes equations results in the Euler equations. Obviously, this reduced–equation set by itself can never be used to simulate the flow of a viscous fluid, but can, however, be used to generate "reasonable" solutions for unsteady flow about extremely complex, three–dimensional geometries, as demonstrated by Whitfield, et al[1] who computed the unsteady flow about three–dimensional transonic propfans using the Euler equations. The precise meaning of "reasonable" relates to the above question(s). That is, an assumption was made in Ref. 1, a priori, that viscous effects could be neglected for the configurations and flow conditions to be investigated. Comparisons between measured and computed performance parameters[1] indicated that this assumption was indeed "reasonably" valid. Therefore, it could be argued that the compromise made to exclude viscous effects from the analysis did not contaminate the computed solutions to the point of being unusable. However, it should be pointed out that this conclusion is based

on the original stipulation that (as an example) effects of viscosity and the ensuing ramifications of its presence were of lower priority in the simulation.

Of the three aforementioned physical characteristics under consideration, the one likely to have the most significant impact upon computational resource requirements concerns that of multidimensions. This can be argued from the standpoint that the number of floating point operations required for a given simulation is roughly proportional to $(n^{ndim})(2 + ndim)^2$, where n is the number of grid points and $ndim$ is the number of spatial dimensions. Of course, this proportionality is greatly dependent upon the numerical scheme used to solve the equations, but at least gives an indication of how quickly the cost of performing multidimensional simulations escalates. Similar to the arguments given above for three–dimensional viscous and inviscid flows, the validity of compromise (i.e., reduction) in the number of independent spatial variables is problem dependent and is difficult to judge, a priori, whether the resulting simulation adequately represents reality. As stated by Hirsch[2], "In all cases, however, the final word with regard to the validity of a given model is the comparison with experimental data or with computations at a higher level of approximation." Therefore, it is the reduction in effects associated with multi–dimensions, while retaining effects of unsteadiness and viscosity, and solution of the resulting equations (for internal flows) which forms the basis and underlying motivation of the present effort. In particular, the development of an engineering tool through which preliminary estimates of unsteady internal flow processes can be generated using available workstation–based hardware is sought.

One approach to achieve this is to seek solutions to the unsteady, two–dimensional Navier–Stokes equations, or the unsteady two–dimensional Euler equations coupled with the steady (or unsteady), two–dimensional boundary–layer equations. While these are valid approaches, even the two–dimensional equations can result in nontrivial computational time requirements, particularly for unsteady flow. However, use of the coupling approach (e.g., Euler coupled with boundary layer) has significant resource–saving advantages over that associated with solving the full Navier–Stokes equations because of relaxed grid requirements in viscous regions[3]. Hence, the coupling approach is adopted here, where equation sets valid for a particular region of the flowfield are used. Specifi-

cally, the Euler equations written for unsteady, quasi–one–dimensional (Q1D) flow are coupled with integral boundary–layer equations for unsteady, two–dimensional turbulent flow over adiabatic walls. The assumption is made that solutions to the coupled equations will yield results of engineering accuracy. It must be emphasised[4] that the validity of using the simplified equations is very problem dependent and, similar to other analytical or computational techniques, requires experience and engineering judgement with regard to whether the approach and/or computed solutions represent reality. No attempts are made at quantifying specific classes of problems for which the approach presented herein can be used. Attempts are made to quantify the validity of these assumptions (or lack thereof) through comparisons with available experimental and computational sources.

An additional assumption fundamental to the coupling approach applied to internal flows is that the flowfield within the channel contains an inviscid "core" (i.e., not fully developed) of fluid which is allowed to interact with the viscous region near the wall. A schematic of this type configuration is shown in Fig. 1. The displacement of mass caused by the presence of this viscous region has a thickness of δ^*, defined by

$$\varrho_e u_e \delta^* = \int_0^\infty (\varrho_e u_e - \varrho u) \, dy$$

which is exact for planar flow, but is only approximate for the axisymmetric case. However, the above expression approaches the true mass defect length for axisymmetric flow when the local boundary layer is thin compared to the local body radius[5,6]. Therefore, the analysis presented herein is valid only for those cases where the boundary layer is small relative to the local body radius.

Results ensuing from this analysis is reported here in two parts. Part 1 is essentially a continuation of efforts reported in Refs. 4 and 7 where an explicit numerical scheme was used to solve the system of equations formed by writing the viscous and inviscid equations as one complete system. This coupling methodology differs from those reported previously (e.g., [3,8,9]) where the coupling was performed between the *solutions* to the equation sets *rather than the equations themselves*. As discussed in Refs. 4 and 7, this approach is motivated by the observation that coupling the solutions results in a scheme which can have convergence difficulties and is often not robust, particularly for

4

"strong" interaction cases. In addition, previous coupling schemes which use the steady, direct form of the boundary–layer equations to solve for the viscous region for cases where boundary–layer separation occurs fail because this form of the boundary–layer equations are singular at or near separation[3]. (It should be noted though that the singularity can be avoided by using the so–called inverse form of the equations[3]. However, because the formulation of the unsteady inverse form is not unique, coupling of the viscous and inviscid equation sets is less than straight–forward[10]). As shown by Moses, et al[11], however, a simultaneous solution procedure (using the steady form of the laminar boundary–layer equations and Laplace equation for the stream function) apparently removes the separation singularity which makes the computation of separated flows possible using the direct form of the boundary–layer equations. In an analogous manner, the present approach simultaneously solves the unsteady forms of the Q1D Euler equations and the unsteady integral boundary–layer equations for turbulent flow for steady subsonic (both separated and attached) flows, as well as unsteady supersonic (attached) flow cases. However, as discussed in subsequent sections, several of the disadvantages which the present direct coupling approach sought to overcome have been replaced with other, perhaps more disheartening ones with regard to seeking numerical solutions of the complete system of equations.

II. PART 1 — SUBSONIC AND SUPERSONIC FLOWS

a. Formulation of Equations

Much of the following material is given in Refs. 4 and 7 but is repeated here to provide the necessary background for the analysis presented in Part 2, and also for convenience to the reader not familiar with previous efforts[4,7]

The equations which form the basis of the present analysis are the unsteady momentum and mean–flow kinetic energy integral boundary–layer equations for turbulent flow (for the viscous region, Eqs. (1) and (2)) and the unsteady Q1D Euler equations for no work and adiabatic flow (for the inviscid region, Eqs. (3), (4), and (5)), and are written as a complete system as[4,7]:

$$\frac{\partial}{\partial t}(\varrho_e u_e \delta^*) - u_e \frac{\partial}{\partial t}(\varrho_e \theta_\varrho) + \frac{1}{R^k}\frac{\partial}{\partial x}\left(\varrho_e u_e^2 R^k \theta\right) + \varrho_e u_e \delta^* \frac{\partial u_e}{\partial x} - \varrho_e u_e^2 \frac{c_f}{2} = 0 \tag{1}$$

$$\frac{\partial}{\partial t}\left[\varrho_e u_e^2(\theta + \delta^* - \theta_\varrho)\right] + 2\varrho_e u_e(\theta_\varrho - \delta_u^*)\frac{\partial u_e}{\partial t} + \frac{1}{R^k}\frac{\partial}{\partial x}(R^k \varrho_e u_e^3 \theta^*)$$
$$+ 2\varrho_e u_e^2(\delta^* - \delta_u^*)\frac{\partial u_e}{\partial x} - 2\varrho_e u_e^3 \frac{c_D}{2} = 0 \tag{2}$$

$$\frac{\partial}{\partial t}(\varrho_e A) + \frac{\partial}{\partial x}(\varrho_e u_e A) = 0 \tag{3}$$

$$\frac{\partial}{\partial t}(\varrho_e u_e A) + \frac{\partial}{\partial x}\left[(\varrho_e u_e^2 + p_e)A\right] - p_e \frac{\partial A}{\partial x} = 0 \tag{4}$$

$$\frac{\partial}{\partial t}(E_e A) + \frac{\partial}{\partial x}[(u_e(E_e + p_e)A] + p_e \frac{\partial A}{\partial t} = 0 \tag{5}$$

where A = area, ϱ = density, u = velocity, p = pressure, E = total energy, t = time, and x = axial distance. Subscript e has been added to the gas dynamic variables to denote "edge" values, taken to be those associated with the inviscid core. It should be noted that the area A, by definition, represents that part of the flow region which contains inviscid fluid. These equations have been non–dimensionalized using the dimensional parameters $\hat{R}_{ref}$(length), $\hat{\varrho}_{0,\infty}$ (density), and $\hat{a}_{0,\infty}$ (velocity) where a is the speed of sound and subscript 0, ∞ indicates upstream stagnation conditions, and ^ denotes a dimensional quantity. In Eqs. (1) and (2), k = 0 for planar flow or 1 for axisymmetric flow, where the following integral length definitions have been used:

6

$$\delta^* = \int_0^\infty \left(1 - \frac{\varrho u}{\varrho_e u_e}\right) dy \tag{6a}$$

$$\theta = \int_0^\infty \frac{\varrho u}{\varrho_e u_e}\left(1 - \frac{u}{u_e}\right) dy \tag{6b}$$

$$\theta^* = \int_0^\infty \frac{\varrho u}{\varrho_e u_e}\left(1 - \frac{u^2}{u_e^2}\right) dy \tag{6c}$$

$$\delta_u^* = \int_0^\infty \left(1 - \frac{u}{u_e}\right) dy \tag{6d}$$

$$\theta_\varrho = \int_0^\infty \left(1 - \frac{\varrho}{\varrho_e}\right) dy \tag{6e}$$

The skin friction and dissipation integral are given by

$$c_f = \frac{2\tau_w}{\varrho_e u_e^2} \tag{7}$$

$$D = \int_0^\infty \frac{\tau}{\tau_w}\frac{\partial}{\partial y}\left(\frac{u}{u_e}\right) dy \tag{8}$$

where τ and τ_w are the local and wall shear stress, respectively.

To place the system of equations in a form amenable to numerical solution using explicit schemes, the temporal derivatives of Eqs. (1) through (5) are isolated, i.e.,

$$\frac{\partial}{\partial t}(\varrho_e u_e \delta^*) - u_e \frac{\partial}{\partial t}(\varrho_e \theta_\varrho) = b_1 \tag{9}$$

$$\frac{\partial}{\partial t}\left[(\varrho_e u_e^2(\theta + \delta^* - \theta_\varrho)\right] - 2\varrho_e u_e(\theta_\varrho - \delta_u^*)\frac{\partial u_e}{\partial t} = b_2 \tag{10}$$

$$\frac{\partial}{\partial t}(\varrho_e A) = b_3 \tag{11}$$

$$\frac{\partial}{\partial t}(\varrho_e u_e A) = b_4 \tag{12}$$

$$\frac{\partial}{\partial t}(E_e A) + p_e \frac{\partial A}{\partial t} = b_5 \tag{13}$$

where b_1 through b_5 are defined by referring to Eqs. (1) through (5), respectively.

Reducing the equations further requires choosing a dependent variable vector. In Refs. 4 and 7, the dependent variables used were

7

$$q = (\varrho_e \quad u_e \quad M_e \quad \theta \quad \overline{H})^T \tag{14}$$

Once this choice is made, the temporal derivatives are expanded and the ensuing terms algebraically manipulated to form a system of five simultaneous partial differential equations, which can be written as:

$$L\frac{\partial q}{\partial t} = b \tag{15}$$

where L is a 5 x 5 matrix, and b is the right–hand–side vector containing spatial derivatives. Here M_e is the edge Mach number, θ is the momentum thickness (Eq. 6b), and $\overline{H}$ is a shape factor defined using integral lengths formed with kinematic properties, i.e.,

$$\overline{H} = \frac{\overline{\delta}^*}{\overline{\theta}} \tag{16}$$

where

$$\overline{\delta}^* = \delta_u^* \tag{17a}$$

$$\overline{\theta} = \int_0^\infty \frac{u}{u_e}\left(1 - \frac{u}{u_e}\right) dy \tag{17b}$$

The number of unknown parameters in Eq. (15) is ten, including those contained in the right–hand–side vector b. Closure of the system of equations requires that all variables be expressed in terms of the dependent variables. This was partially accomplished in Ref. 7 (and here as well) through the use of several auxiliary relations involving boundary–layer integral length shape factors and the perfect gas equation of state. Complete closure was accomplished in Ref. 7 by using the relation

$$\frac{\hat{T}_{0,e}}{\hat{T}_e} = 1 + \frac{\gamma - 1}{2}M_e^2 \tag{18}$$

which is justified so long as the gas is thermally perfect and that the gas is in a state of equilibrium at each cross–section. To illustrate how the above relation was used in Ref. 7, consider the following expression for the total (stagnation) energy, written in dimensional form as

$$\hat{E}_e = \hat{\varrho}_e\hat{e}_e + \frac{1}{2}\hat{\varrho}_e\hat{u}_e^2 \tag{19}$$

where $\hat{e}_e$ is the internal energy given by (for a perfect gas)

8

$$\hat{e}_e = \hat{c}_v \hat{T}_e \qquad (20)$$

and $\hat{c}_v$ is the constant–volume specific heat. It is obvious that the temperature must be expressed in terms of the dependent variables. This was performed in Ref. 7 as follows. In non–dimensional form, the internal energy becomes

$$\frac{\hat{e}_e}{\hat{a}_{0,\infty}^2} = \frac{\hat{c}_v \hat{T}_e}{\hat{a}_{0,\infty}^2} = \left[\frac{\hat{c}_v}{\gamma \hat{R}}\right] \frac{\hat{T}_e}{\hat{T}_{0,e}} \frac{\hat{T}_{0,e}}{\hat{T}_{0,\infty}} = \frac{1}{\gamma(\gamma-1)} \frac{\hat{T}_e}{\hat{T}_{0,e}} \frac{\hat{T}_{0,e}}{\hat{T}_{0,\infty}} \qquad (21)$$

where $\hat{T}_{0,e}$ is the local stagnation temperature and $\hat{R}$ is the perfect gas constant. Making the definitions

$$f_e = \frac{\hat{T}_{0,e}}{\hat{T}_e} = 1 + \frac{\gamma-1}{2} M_e^2 \qquad (22a)$$

$$\tilde{e}_e = [\gamma(\gamma-1)f_e]^{-1} \qquad (22b)$$

results in

$$\frac{\hat{e}_e}{\hat{a}_{0,\infty}^2} = \tilde{e}_e T_{0,e} \qquad (23)$$

Therefore, the non–dimensional expression for total energy can be written

$$E_e = \varrho_e \left(\tilde{e}_e T_{0,e} + \frac{1}{2} u_e^2\right) \qquad (24)$$

where

$$T_{0,e} = \frac{\hat{T}_{0,e}}{\hat{T}_{0,\infty}} \qquad (25)$$

Differentiating the above expression for total energy results in derivatives of the quantity $T_{0,e}$ which must be assumed constant or otherwise specified. Therefore, the assumption was made in Ref. 7 that *the ratio of local to reference stagnation temperature was equal to one (constant)*, thus eliminating these derivatives. In addition, the above ratio also appears in several terms within the elements of the matrix L. Although this is a good approximation for steady flows involving no heat transfer, the validity of the assumption becomes questionable for unsteady flows, even with no heat transfer. This can be seen by rewriting the energy equation (Eq. (5)) in terms of stagnation enthalpy,

$$\frac{\partial}{\partial t}(\varrho_e A h_0) + \frac{\partial}{\partial x}(\varrho_e u_e A h_0) = A\frac{\partial p_e}{\partial t} \qquad (26)$$

where h_0 is the stagnation enthalpy defined by

$$h_0 = h_e + \frac{1}{2}u_e^2 \qquad (27)$$

Use of the continuity equation results in

$$\frac{\partial h_0}{\partial t} + u_e\frac{\partial h_0}{\partial x} = \frac{1}{\varrho_e}\frac{\partial p_e}{\partial t} \qquad (28)$$

We can rewrite the left–hand–side of the above as a material derivative to finally arrive at

$$\frac{Dh_0}{Dt} = \frac{1}{\varrho_e}\frac{\partial p_e}{\partial t} \qquad (29)$$

which is valid in the absence of work and heat flux. By using the energy equation in this form, it is straight–forward to see that changes in static pressure due to unsteadiness results in corresponding changes in the stagnation enthalpy, and thus the stagnation temperature.

This situation can be avoided in at least two ways. One method is to express the internal energy instead as

$$\frac{\hat{e}_e}{\hat{a}_{0,\infty}^2} = \frac{\hat{c}_v}{\gamma\hat{R}}\frac{\hat{T}_e}{\hat{T}_{0,\infty}} = \frac{T_e}{\gamma(\gamma-1)} \qquad (30)$$

where

$$T_e = \frac{\hat{T}_e}{\hat{T}_{0,\infty}} \qquad (31)$$

From the definition of the sonic velocity

$$a_e^2 = \frac{\hat{a}_e^2}{\hat{a}_{0,\infty}^2} = \frac{\hat{T}_e}{\hat{T}_{0,\infty}} = T_e \qquad (32)$$

and using the Mach number, it follows that

$$\frac{\hat{e}_e}{\hat{a}_{0,\infty}^2} = \frac{u_e^2}{\gamma(\gamma-1)M_e^2} \qquad (33)$$

which is the desired result.

10

Another way to avoid making the constant stagnation temperature assumption is to replace Mach number with static pressure as a dependent variable. To illustrate this, consider the perfect gas equation of state given by

$$\hat{p}_e = \hat{\varrho}_e \hat{R} \hat{T}_e \tag{34a}$$

or, in non-dimensional form,

$$p_e = \frac{\varrho_e T_e}{\gamma} \tag{34b}$$

Therefore,

$$T_e = \frac{\gamma p_e}{\varrho_e} \tag{34c}$$

It follows that the Mach number can be computed as

$$M_e = \frac{\hat{u}_e}{\hat{a}_e} = \frac{u_e}{(T_e)^{1/2}} \tag{35}$$

which again permits closure of the system.

Results ensuing from numerical schemes based upon all three formulations are presented in this report. As discussed in subsequent sections, both explicit and implicit numerical methods have been implemented. Whereas an explicit scheme has been utilized in all formulations, the implicit method has been applied to only the formulation where pressure is used as a dependent variable.

Because of the possible ramifications regarding solutions computed using the original formulation which assumes constant stagnation temperature[7], a brief diversion will be taken at this point to investigate differences between computed steady and unsteady solutions resulting from the different formulations. As mentioned above, numerical computations involving all formulations have been performed using an explicit scheme (implementation of this scheme is discussed in Section II.c). To investigate differences in computed solutions ensuing from these formulations, results for a constant area axisymmetric duct (10 radii in length) with a fixed entrance Mach number of 2 and a reference Reynolds number of 5 million are presented. Converged (steady–state) solutions from these computations are shown in Figs. 2 and 3. Figure 2a presents time histories of exit Mach number and it can be seen that identical results are obtained at steady state for all formulations. Also, convergence

of both formulations which do not assume constant $T_{0,e}$ are seen to be essentially identical. Although not shown here, all other pertinent flowfield parameters converge in a similar manner. In addition, Fig. 2b illustrates convergence as measured by the root–mean–square residual of the velocity, defined as

$$\left(\frac{\delta u_e}{\delta t}\right)_{rms} \equiv \frac{1}{N_{max} - 2}\left[\sum_i \left(\frac{u_e^{n+1} - u_e^n}{\Delta t}\right)_i^2\right]^{1/2} \tag{36}$$

where N_{max} is the total number of grid points. It is of interest to note that although convergence to machine epsilon (using double–precision floating–point operations) is achieved in approximately 40 (non–dimensional) time units (corresponding to approximately 400 – 700 time steps at a CFL of 0.9), referring back to Fig. 2a indicates that the solution at the exit has stopped changing appreciably in less than half that time.

As expected, the different formulations do not give the same results for unsteady flows, although differences are observed not to be large, at least for the cases examined thus far. Computed solutions from all formulations for an unsteady flow are illustrated in Fig. 3. This is a contrived test case presented in Ref. 7 for the duct mentioned above, where now the entrance Mach number is sinusoidally varied at a non–dimensional frequency of 0.1 to yield an entrance Mach number with a mean value of 2.0 and an oscillatory magnitude of 0.2. Fig. 3a compares computed exit Mach number solutions based upon all formulations where the entrance (input) Mach number is also shown for comparison. It can be seen that solutions from formulations not involving the assumption of $T_{0,e}=$ *constant* are identical. Although these solutions are very similar to those from the original formulation, minimum and maximum values of computed Mach number are seen to vary. Also, there is a very slight phase shift regarding the (min,max) values of Mach number. However, as shown in Fig. 3b, differences in computed boundary–layer integral lengths are much less. The origin of these relatively small differences can be seen in Fig. 3c which illustrates the time variation of stagnation temperature at the duct entrance and exit, the former of which is constant, by definition. It can be seen that at this axial location, the maximum variation of stagnation temperature is approximately three to four

12

percent. Therefore, an assumption of $T_{0,e} = constant$ (used in the original formulation) is reasonable, at least for this degree of unsteadiness.

Although differences exist between computed unsteady solutions that are based upon different formulations of the system of equations, these differences are remarkably small, at least for the test case shown. However, because the formulation which assumes $T_{0,e} = constant$ is inconsistent with regard to the simulation of unsteady flows, either of the new formulations are the preferred methodologies in this regime. This is particularly true if the present coupling methodology is to be applied to cases involving both unsteady flow and added heat flux.

As discussed previously, the system of equations is written in terms of the coefficient matrix L, where the elements of L vary according to the particular formulation. Elements of the matrix L (as well as those of another matrix N, to be discussed next) are given in the Appendix for all formulations discussed herein.

b. Eigenvalue Structure of the System of Equations

In Refs. 4 and 7, the approach to solve the system of equations (14) was to use semi–discretization which results in a system of ordinary differential equations at each mesh point. The equations were then solved with a two–stage Runge–Kutta scheme using first–order backward spatial differencing throughout the computational domain. The exclusive use of upwinding was possible in Ref. 7 because for the cases considered, all eigenvalues of the coefficient matrix $L^{-1} N$ were found to be positive (as well as real, of course). The matrix $L^{-1} N$ results from writing the system of equations (14) in quasi–linear form

$$\frac{\partial q}{\partial t} + L^{-1}N\frac{\partial q}{\partial x} = L^{-1}d \tag{37}$$

where the matrix N is derived in similar fashion as is the matrix L. Also, the different formulations discussed previously result in differences in various elements of the matrix N (similar to the matrix L). Elements of the N matrix for all formulations are given in the Appendix.

It is of interest to examine the behavior of the eigenvalues over the expected range of the various parameters upon which elements of the matrix $L^{-1}N$ depend. Using isentropic relations between

13

local static and stagnation conditions, it is straight–forward to show that these elements (and thus the eigenvalues) can be expressed in terms of M_e, $\overline{H}$, and θ. Eigenvalue distributions as a function of Mach number are shown (as lines) in Fig. 4 with both $\overline{H}$ and θ used as parameters. The eigenvalues shown were computed using the elements of the L and N matrices resulting from the formulation where M_e was used as a dependent variable but $T_{0,e}$ was not assumed constant. (It is of interest to note that eigenvalues computed using the formulation where p_e is a dependent variable are virtually identical to those shown). Because of the algebraic complexity of the matrix $L^{-1}N$, the eignevalues were computed numerically using an iterative technique[12]. Also plotted in these figures (as symbols) are the eigenvalues associated with the Q1D Euler equations written as an isolated system (u_e, $u_e + a_e$, and $u_e - a_e$). It should be noted that Reynolds numbers were evaluated assuming reference (stagnation) temperature and pressure to be $520°R$ and 14.7 psia, respectively. This results in momentum thickness Reynolds numbers ranging from approximately 400 to 480,000 for $0.001 \le \theta \le 0.1$.

Figures 4a–4e ($\theta = 0.001$) illustrate eigenvalue behavior for $1.2 \le \overline{H} \le 6.0$. It can be seen that for shape factors less than approximately 2.0, all eigenvalues remain positive for Mach numbers greater than one thus confirming observations in Ref. 7. However, this is not the case for higher values of $\overline{H}$ as shown in Figs. 4d and 4e which indicate at least one eigenvalue becomes negative for $M_e >$ 1. Also, it is interesting to note that three eigenvalues of the complete system closely approximate those of the inviscid equations for all values of $\overline{H}$.

Perhaps the most interesting (or disturbing) aspect of eigenvalue behavior can be seen in Figs. 4d and 4e which indicate the appearance of complex conjugate pairs at high shape factors and supersonic Mach numbers, where the range of Mach numbers within which this occurs decreases with increasing $\overline{H}$. While only the real part is plotted, the imaginary part is observed to be at least one order of magnitude smaller than the real part. It should be noted that the appearance of complex eigenvalues seem to occur for shape factors high enough to be indicative of boundary–layer separation. Discussion regarding the ramifications of the appearance of complex eigenvalues is given at the end of this section.

One might hope that complex eigenvalues would occur only within a relatively small range of values associated with the various parameters. Unfortunately, this is not the case which is illustrated in Figs. 4f through 4o. In Figs. 4f–4j ($1.2 \leq \bar{H} \leq 6.0$, $\theta=0.01$), complex eigenvalues again appear, but only for shape factors high enough to cause boundary–layer separation (which generally occurs for $2.8 \leq \bar{H} \leq 3.0$, depending upon the Reynolds number). The range of Mach numbers over which this occurs is rather extensive at higher values of $\bar{H}$. It should also be noted that significant deviation from the inviscid eigenvalues has occurred at the higher values of momentum thickness, particularly for higher shape factors. In addition, negative eigenvalues occur over the entire range of Mach number, again for higher values of $\bar{H}$. This behavior is even more pronounced for very high values of momentum thickness as shown in Figs. 4k–4o ($1.2 \leq \bar{H} \leq 6.0$, $\theta=0.1$). However, one could argue that for $\theta=0.1$ we have violated one of the fundamental assumptions regarding use of the coupling approach; i.e., recalling that θ has been non–dimensionalized by a reference length (usually the inlet radius or half–height), a value of $\theta=0.1$ indicates that the local momentum thickness is 10% of the local radius. Assuming a shape factor of 1.5 and that the local radius variation is small compared to that of the inlet (which is consistent with the Q1D assumption) implies that the displacement thickness occupies 15% of the channel radius. Assuming further that the displacement thickness is approximately 1/6 of the total viscous region implies that the flow is essentially fully developed which, of course, violates our original stipulation that this not be the case. Therefore, Figs. 4k–4o should be interpreted as an illustration of how the eigenvalues behave toward the upper end of valid parameter space. On the other hand, values of θ in the range of 0.1 do not necessarily imply that the channel is fully developed. For separated flows, integral lengths have the tendency to grow rapidly because of the large, retarded flow region near the wall. However, the overall viscous region can remain small enough such that an inviscid core exits. Example of this are illustrated in subsequent sections.

The appearance of complex eigenvalues indicates that the system of equations in their present form cannot allow solutions as a well–posed initial/boundary–value problem by integration over time. This conclusion is based upon the work of Briley et al[13] who used the criterion set forth by Garabe-

dian[14] "that it is natural to require that every root of the characteristic equation be real, as this excludes solutions that may grow exponentially with the time–like variable"[13]. Therefore, exponential growth in solutions of a system of equations (which supposedly represent certain physics) can be attributed to numerical instability of the unsteady solution algorithm and/or to a mathematical set of equations which is ill–posed for solutions as an initial value problem in time[15]. Differentiating between these two areas of concern for the present effort requires that the problem be separated into its individual pieces, namely, physics, mathematics, and numerics. That is, the objective is to obtain a valid mathematical representation (equations) of the physics and to numerically solve these equations in a stable manner to a specified order of accuracy. With regard to the physics of the inviscid flow, it has been well established that the Euler equations represent a very good approximation to the motion of a fluid in regions where effects of viscosity are neglible. However, with regard to the physics of the boundary–layer flow, Whitfield[16] encountered complex eigenvalues in seeking solutions to the unsteady integral boundary–layer equations where time was used as an iterative parameter to reach steady state. In addition, similar eigenvalue behavior was encountered in Refs. 10 and 17 in dealing with the unsteady, three–dimensional integral boundary–layer equations which, however, did not preclude obtaining reasonable numerical solutions[10,17]. Along these same lines, the integral boundary–layer equations of the type used herein have been shown to yield good engineering approximations to viscous flows in regions where the usual boundary–layer assumptions are valid for both steady and unsteady regimes[6,18].

Based upon the above discussion, it is reasonable to conclude that it is the approximate governing equations which are the origin of the observed anomalies. While the system of equations used in the present effort does not generally exclude solutions exhibiting exponential growth due to ill–posedness, it is shown in subsequent sections that numerical solutions of engineering accuracy can be obtained for those cases where either: (a) no complex eigenvalues are encountered, or (b) if complex eigenvalues do appear, unbounded growth can occur but can be very slow, thus allowing reasonable solutions to be computed.

Because the method presented herein uses many of the same shape factor correlations and auxiliary relations employed in Refs. 10 and 16, it is believed that the appearance of complex eigenvalues can be attributed to the approximations introduced by these empirical and analytical relations; i.e., these empirical relations and approximations are insufficient to define a well–posed set of approximate governing equations. Of course, this situation calls for an analysis similar to that performed by Briley[13] to attempt to locate the specific relations which cause the observed eigenvalue behavior. Unfortunately, time and resource limitations preclude pursuing such an analysis.

c. Numerical Method

Based upon the preceding discussion, a numerical scheme utilizing spatial difference operators other than purely one–sided is required for the general case unless, of course, a completely upwind method which uses spatial differences whose type depends upon local flowfield characteristics (eigenvalues) is used (note this approach is not even applicable for situations resulting in complex eigenvalues). Because of the algebraic complexity of the governing system of equations and the above concerns regarding well–posedness, an upwind approach was deemed inappropriate. Therefore, in the interest of simplicity, the predictor–corrector MacCormack scheme[19] was utilized for the present effort.

MacCormack's scheme can be applied to a scalar (or system of) conservation law(s)

$$\frac{\partial u}{\partial t} + \frac{\partial f}{\partial x} = 0 \tag{38}$$

and is written as:

$$u_i^{\overline{n+1}} = u_i^n - \Delta t \nabla f_i^n \tag{39a}$$

$$u_i^{n+1} = \frac{1}{2}\left(u_i^n + u_i^{\overline{n+1}}\right) - \frac{1}{2}\Delta t \Delta \overline{f_i^{n+1}} \tag{39b}$$

where subscript "i" and superscript "n" denote spatial and temporal indices, respectively. Also, ∇ and Δ denote first–order backward and forward difference operators, respectively. In an analogous manner, we can rewrite the present system of equations as

$$\frac{\partial q}{\partial t} + b' = 0 \tag{40a}$$

where

17

$$b' = -L^{-1}b \tag{40b}$$

MacCormack's scheme is then implemented as:

$$q_i^{\overline{n+1}} = q_i^n + \Delta t dq_i^n \tag{41a}$$

$$q_i^{n+1} = \frac{1}{2}\left(q_i^n + q_i^{\overline{n+1}}\right) + \frac{1}{2}\Delta t dq_i^{\overline{n+1}} \tag{42}$$

where, for example,

$$dq_i^n = b'_i{}^n = -(L^{-1}b)_i^n \tag{43}$$

In the predictor step, the vector function dq is evaluated using dependent variables computed at time level n and inverting the matrix L at each mesh point. This inversion is carried out using an efficient LU factorization[12]. Spatial derivatives in the vector b are approximated (conservatively) using first-order backward differences where variables are again evaluated at the nth time level. Similar computations are performed during the corrector step, except that predicted values at time level $\overline{n+1}$ are used to perform the matrix inversion, and first-order forward spatial differences are used to approximate spatial derivatives. Because this is a central spatial difference scheme, additional numerical dissipation must be added to suppress unwanted oscillations. A simple fourth-order model used by Warming and Beam[20] was used and implemented by modifying the corrector step Eq. (32b) above to give:

$$q_i^{n+1} = \frac{1}{2}\left(q_i^n + q_i^{\overline{n+1}}\right) + \frac{1}{2}\Delta t dq_i^{\overline{n+1}} + c_s c_\omega \delta^4 q_i^n \tag{44a}$$

where[20]

$$\delta^4 q_i^n = q_{i+2}^n - 4q_{i+1}^n + 6q_i^n - 4q_{i-1}^n + q_{i-2}^n \tag{44b}$$

$$c_s = -\frac{1}{8} \tag{44c}$$

$$c_\omega = 1 - CFL^2 \tag{44d}$$

where $CFL \leq 1$ for stability. All solutions computed with this scheme were obtained with a CFL number of 0.9.

d. Boundary Conditions

For supersonic inflow and outflow, all dependent variables were specified and extrapolated, respectively. Conditions at subsonic inflow and outflow boundaries were treated by considering the invis-

cid and viscous equations separately. That is, for subsonic outflow, pressure was specified and density, velocity, and boundary–layer parameters were extrapolated. Mach number was then determined from velocity and the computed sonic speed. For subsonic inflow, the method proposed by Cooper et al[21] was used for the inviscid equations. By specifying inflow stagnation conditions, this method iteratively solves for the variables T_e, p_e, and u_e using the equations (non–dimensional)

$$T_{0,e} = T_e + \frac{\gamma - 1}{2}u_e^2 \tag{45a}$$

$$p_e = p_{0,e}\left(\frac{T_e}{T_{0,e}}\right)^{\gamma/\gamma - 1} \tag{45b}$$

$$C = u_e - \frac{p_e}{\varrho_e a_e} \tag{45c}$$

where T is the temperature and a is the speed of sound. C used in Eq. (35c) is a "characteristic–like" variable and is computed from information at the first mesh point inside the boundary[21]. Boundary–layer parameters θ and H are specified and held fixed at the inflow boundary.

e. Results

The objective of this section is to present comparisons between computations obtained using the present interaction technique and measurements, as well as other computations. Subsonic and supersonic results are reported in separate sections where subsonic comparisons are all for steady diffuser flows, whereas supersonic computations are for both steady and unsteady channel flows. In all computations shown here, 51 equally spaced points were used in the axial direction.

1. Subsonic Diffuser

Axisymmetric subsonic diffuser flowfields investigated by Little et al[22] are compared with those computed using the present scheme (designated BL1D) in Figs. 5 and 6. The physical configuration consisted of several inlet pipe lengths (to give constant inlet boundary–layer thicknesses) and diffuser half–angles, although only comparisons for the 12 degree, 21 inch configuration for inlet boundary layer heights of $\delta^*/R_{inlet} = 0.0034$ (thinner inlet boundary layer) and $\delta^*/R_{inlet} = 0.0190$ (thicker inlet boundary layer) are reported here. It is almost embarrassing to report that computa-

19

tions resulting from the present interaction method required up to 30,000 time iterations to achieve convergence. However, it was suspected beforehand that this would be the case using an explicit numerical scheme for subsonic internal flows. Because the interaction methodology was of primary interest for the present effort (in particular, obtaining converged solutions which included boundary–layer separation), large iteration counts were considered an acceptable compromise between simplicity and efficiency. No attempt was made to optimize the code which was executed on a Silicon Graphics, Inc. Personal IRIS 4d/30TG at a rate of 0.0016 cpu–seconds per time step per grid point. Therefore, a test case with 51 grid points requiring 10,000 time iterations resulted in approximately 14 minutes of execution time.

Also shown for comparison are computed parameters using a more classical interaction technique (herein designated as DUCFLO) where the inverse form of the steady integral boundary–layer equations are iterated with edge velocity obtained from the constant mass–flow constraint. The inverse boundary–layer method used to obtain these results is that reported by Whitfield, et al[23], although the DUCFLO interaction code (written by Whitfield), and findings generated by this code, have not been reported elsewhere. It should be noted further that this code can achieve converged solutions much more quickly than that using BL1D. However, the DUCFLO formulation is valid only for subsonic, steady flow and for this class of problems is generally the preferred technique with regard to computational resource requirements.

Thinner Inlet Boundary Layer

Figs. 5a–5e present comparisons between measured and computed distributions of static pressure, displacement thickness, momentum thickness, shape factor, and skin friction through the diffuser for the thinner inlet boundary layer case (integral lengths were formed using only kinematic properties). Fig. 5a compares measured and computed static pressures (normalized by the inlet stagnation value), where the exit pressure (in BL1D) was adjusted until that at the inlet station matched the measured value. Except for the region where diffuser diverence begins, computed pressures (from both BL1D and DUCFLO) are seen to compare favorably with those measured. It should be noted that the computed inlet pressure using BL1D was somewhat sensitive to the specified exit pressure. That

is, the exit pressure used to obtain the distribution shown in Fig. 5a was approximately 0.905, giving in inlet pressure of 0.60. Increasing the exit pressure to approximately 0.92 resulted in an inlet pressure of approximately 0.66. Therefore, cases reported in this section (using BL1D) were obtained by adjusting the exit pressure to match that at the inlet.

Figs. 5b and 5c compare measured and computed "incompressible" displacement and momentum thickness distributions through the diffuser. It can be seen that both computational techniques over-predict and underpredict $\overline{\delta^*}$ and $\overline{\theta}$, respectively, although this agreement is considered reasonable. As a result of this over– and underprediction, computed shape factors are correspondingly high, as shown in Fig. 5d. It is reported in Ref. 22 that boundary–layer separation was not present in the experiment and none is predicted by the computations. This is illustrated in Fig. 5e which presents computed skin friction distributions (no measurements were available). However, exit shape factors in the range shown in Fig. 5d are an indication that considerable retardation in the velocity profile is present (i.e., the boundary layer is close to separation). This is illustrated in Fig. 5e which compares measured and computed (from BL1D) velocity profiles at the diffuser exit, where measured profiles were obtained at three circumferential positions 120° apart. Although agreement between measured and computed velocities is not particularly good at this axial location, considerable scatter exists in the data. Nonetheless, the computed profile is too thin and is also more retarded near the wall. However, as stated above, both measured and computed profiles are seen to be close to separation.

Thicker Inlet Boundary Layer
Fig. 6 presents comparisons between distributions of measured and computed (BL1D and DUCFLO) diffuser parameters for the thicker inlet boundary–layer case. As stated previously, the exit pressure was adjusted until the computed inlet pressure approximated the measured value. Similar to the thinner inlet boundary–layer case, good agreement between measured and computed pressure distributions is indicated in Fig. 6a, although there is a "kink" in that computed by DUCFLO. This is apparently due to boundary–layer separation which is predicted by both BL1D and DUCFLO. It can be seen in Fig. 6b that good agreement between measured and computed displacement thick-

ness is obtained (except near the diffuser exit), although computed values are again slightly high. Similar comments can be made regarding measured and computed distributions of momentum thickness shown in Fig. 6c, although DUCFLO again exhibits a marked "kink" within the separated region which is not evident in the BL1D computation. As expected, computed shape factors are again too high corresponding to overpredicted displacement thickness. The extent of boundary–layer separation is shown in Fig. 6e which presents computed skin friction distributions for the thicker inlet boundary–layer case. The DUCFLO computations indicate a larger separated region than BL1D in that separation and reattachment occurs farther upstream and downstream, respectively, than does BL1D (again, no measurements were available). Figure 6f gives comparisons between measured and computed velocity profiles at the diffuser exit. Again, measurements were obtained at three circumferential positions around the diffuser exit. The computed velocity profile shows no reverse flow at this axial location (the computed boundary layer has reattached), whereas at least one set of these measurements indicate that the flow is separated. However, the agreement between measured and computed velocity profiles is considered reasonable.

2. Supersonic Channel

Steady and unsteady computations from BL1D for supersonic channel flows are compared to Navier–Stokes calculations in this section. Although supersonic nozzle flow calculations were reported previously[7], the test case reported in Ref. 7 was for steady flow and compared only measured and computed wall static pressures. Attempts are made here to extend such comparisons to include the boundary layer, particularly for unsteady flow.

Justification for comparing results ensuing from one computational technique to those of another comes from Hirsh[2] in reference to comments made in the Introduction; that is, computations resulting from a Navier–Stokes analysis represent a higher level of approximation than those associated with the present methodology. The supposition here is that the technique employing the higher level of approximation is a better representation of the physics. While comparisons such as these are common within the technical community, favorable agreement does not necessarily mean that results from the more approximate method represent reality; it just means that the two computations agree

with each other. The pitfall here is that while techniques utilizing a higher degree of approximation (i.e. more complete mathematics), may indeed represent more complete physics, the numerical method used to solve the resulting equations may be such that these physics are masked or otherwise lost. Therefore, in keeping with previous comments regarding distinctions between physics, mathematics, and numerics, there can be no doubt that the Navier–Stokes equations are a more complete mathematical representation of the physics associated with supersonic internal channel flows. However, we are assuming here that the numerical scheme used to give approximate solutions is yielding these physics to an acceptable level of accuracy which, of course, results in a better representation of the physics.

The Navier–Stokes method used to obtain viscous solutions presented herein is that developed by Whitfield[24] and co-workers[25–26]. The particular version used most closely resembles that reported in Ref. 26 which has been modified to include explicit evaluation of viscous terms and extension of the solution algorithm to the so-called "modified two–pass scheme". This code has as its basis an Euler solver which is an implicit finite–volume, formulation applying Roe's[27] approximate Riemann solver, and the higher–order extensions of Osher and Chakravarthy[28], to compute the inviscid flux terms. The implicit operator is formed using Steger's[29] flux vector splitting with the resulting system of equations inverted by application of Whitfield's[30] two–pass or modified two–pass algorithm. The modified two–pass algorithm was applied in these computations. A brief description of the numerical scheme is included in the Appendix and the reader is encouraged to seek out the noted references for more details about the algorithm and the implementation.

Comparison between BL1D and Navier–Stokes computations were made for two test configurations. The geometry analyzed was a transonic nozzle used as an AGARD[31] test case originally designed for evaluation of Navier–Stokes simulation capability relative to shock/boundary–layer interaction. To maintain isentropic, supersonic core flow, the nozzle pressure ratio was maintained below the second critical design pressure for the present computations.

Comparisons were made on this geometry for two test cases. The first comparison is made for steady supersonic flow subject to fixed inlet total pressure and total temperature and prescribed exit static pressure. The second case is for an unsteady flow and is created by linearly increasing the inlet total pressure as a function of time, whereas inlet total temperature is held constant and exit static pressure is again maintained near second critical design pressure. The geometry is shown in Fig. 7a.

It should be pointed out that a problem arises when making comparisons between the Q1D analysis and the two–dimensional Navier–Stokes analysis. In the Q1D computation all flow–field parameters at a particular instant vary only as a function of axial location. However, each Navier–Stokes simulation produces a two–dimensional flow–field and determination of equivalent one–dimensional flow parameters for comparison is at best ambiguous. This results from the observation that determination of the boundary layer edge is not unique for a complex velocity profile.

Steady Case

For Navier–Stokes analysis, the AGARD transonic nozzle[31] was modeled using 153 X 30 mesh points in the axial and vertical directions, respectively. The grid spacing at the viscous wall, $\Delta y/h$ is approximately .0002 (where h is the channel half–height). This corresponds to a y^+ value of approximately 4. The Reynolds number based upon reference conditions and channel half–height is approximately 1.0×10^6. The grid used and the boundary conditions specified in this simulation is shown in Fig. 7b.

Identical boundary conditions and nozzle area variation were used to preform a corresponding simulation with the BL1D code beginning at axial location x=90mm, where inlet boundary conditions were taken from the Navier–Stokes simulation. Comparisons of computed distributions of Mach number, density, momentum thickness, and shape factor are shown in Figs. 8a–8d. Generally, agreement between computed core parameters from the two methods is considered good. However, momentum thickness and shape factor do not agree as well, where the largest disagreement occurs for 150mm $\leq x \leq$ 250mm. Fig. 8e shows velocity profiles in the nozzle region which illustrates that a unique definition of the boundary–layer edge is not possible thus causing the wide variations in

boundary–layer parameters computed from the Navier–Stokes results. This illustrates how the definition of quantities such as momentum thickness and shape factor lose their significance in the context of complex velocity profiles such as those shown in Fig. 8e.

Unsteady Case

The AGARD nozzle geometry was modified for use as an unsteady test case. To produce a larger region within which comparisons could be made, the nozzle geometry was arbitrarily extended (in the axial direction) 4 nozzle heights as shown in Fig. 9. This geometry was then modeled with a 185 X 30 grid similar to the grid used for the steady test case (Fig. 7b). Boundary conditions were as shown in Fig. 9. As stated previously, unsteady flow through the nozzle was initiated through temporal variation of the reservoir total pressure, shown in Fig. 10a. A uniform time step was selected such that the CFL number in the centerline region was near unity. This produced a maximum CFL number in the viscous layer in excess of 10^3. This is expected to adversely affect temporal accuracy of the simulation, but was deemed necessary in order to obtain results in a reasonable amount of CPU time. The impact of high CFLs occurring within large regions of the viscous flow field was not analyzed.

A portion of the nozzle geometry (shown in Fig. 9) was analyzed with BL1D for comparison purposes. The Navier–Stokes simulation was used to define temporal boundary conditions at the inlet of the "BL1D nozzle" (Fig. 9); these variations at x = 300 mm are shown in Fig. 10b. Comparisons between computed distributions of Mach number, density, momentum thickness, and shape factor at non–dimensional times of approximately 500, 1000, 2000, and 3000 are shown in Figs. 11 through 14, respectively. At all time levels, agreement between computed inviscid core parameters (a and b parts of Figs. 11 through 14) is considered very good. However, computed boundary–layer integral lengths do not agree nearly as well, although the overall qualitative trends of boundary–layer behavior computed by BL1D are in good agreement with the Navier–Stokes results.

The reader should note the "waves" and "wiggles" in the Navier–Stokes results shown in these figures. As mentioned above, transforming two–dimensional results ensuing from the Navier–Stokes

25

analysis has proved to be somewhat challenging. These difficulties can be traced fundamentally to one's definition of the boundary–layer "edge"; i.e., where the viscous region "ends" and the inviscid core "begins". Integral lengths computed from the Navier–Stokes solution presented herein were generated by starting a search at the wall for the first maximum value of velocity (at a particular axial location and instant in time) which was then defined as the boundary–layer edge. Values of velocity, density, and Mach number at this y–location were then used to generate the various integrals. However, significantly different values of edge quantities are obtained using another definition. For example, Fig. 15 compares computed momentum thickness distributions from the Navier–Stokes results at the 1000 time–level (this corresponds to Fig. 12d) using two different edge condition definitions. For the second definition, the search discussed above was again performed to locate the first u_{max} in a particular profile. This value of velocity was then multiplied by 0.99 and another search conducted, again starting from the wall. The first index where the velocity exceeded the $0.99u_{max}$ value was then defined as the edge. This results in considerably different values of various edge quantities, the result of which is illustrated in Fig. 15.

Therefore, although differences exist between computed unsteady core and boundary–layer quantities resulting from Navier–Stokes and BL1D analyses, it appears that the Q1D approach is valid for this type configuration, at least for the conditions investigated. Again, however, additional efforts are warranted to investigate more consistent methods to interpret two–dimensional physics from a one–dimensional perspective.

III. PART 2 —— TRANSONIC FLOWS

All previous discussion has been concerned with taking the system of equations (Eqs. (1) – (5)) and algebraically manipulating various terms in order to recast the original system in a form amenable for solution using relatively simple explicit numerical schemes. Although this approach has been shown to be capable of quickly yielding solutions of reasonable accuracy (at least for the cases presented herein), the scheme possesses several distinct disadvantages. For example, many attempts to compute solutions containing near–discontinuous behavior of the dependent variables (i.e., shocks) with the explicit method have been unsuccessful, regardless of the type artificial dissipation model used (including that used in the following implicit scheme–see Section III. c). Because the ability to capture flows of this type is vital to any flow model which must operate in the transonic regime, it was evident that another approach must be pursued.

Although not reported here, other explicit schemes have also been implemented, but again were not capable of capturing solutions with steep gradients. Therefore, the decision was made to implement an implicit scheme because of the inherent gains in stability bounds over those typically associated with explicit methods. It should be noted that this decision was originally prompted by the issue of *numerical* stability. It is recognized that if difficulties exist in obtaining numerical solutions for an ill–posed initial/boundary–value problem, it is probable that one's choice of numerical scheme is not relevant. As stated previously, the present system of equations exhibit complex eigenvalues in flow regimes where shape factors (H) are high enough to induce boundary–layer separation. However, the magnitudes of the imaginary part of these complex eigenvalues are observed to be very small (one or two orders of magnitude less than the real part). One could interpret this as meaning that the eigenvalue is "almost real" thus making the system "almost well–posed". Nonetheless, as stated above, obtaining solutions using any scheme (especially those which are explicit) remains difficult and therefore we cannot discard the possibility that the system is fundamentally ill–posed in certain flow regimes. Obviously, additional study is needed in this area.

The algebraic complexities of the present system of equations limit the number of implicit schemes which can be used. For example, implicit schemes of Briley and McDonald[32] or Beam and Warm-

ing[33] can not be easily applied to this system because it cannot be written in fully conservative form. However, using a Newton–based implicit solver circumvents this limitation by discretizing the system in both time and space and then iterates the resulting system to convergence. The following discussion describes the Newton formulation as well as other issues resulting from its use.

a. Formulation of the Newton Scheme

Following the analysis presented by Whitfield[30], a classical implementation of Newton's method for finding roots to a nonlinear scalar function $f(x) = 0$ can be written as

$$f'(x^m)\ (x^{m+1} - x^m) = -f(x^m) \tag{46a}$$

where m is an iteration parameter and

$$f' = \frac{df}{dx} \tag{46b}$$

Now consider a system of nonlinear equations (each a function of several variables) written in very general form as[29]

$$F_1(x_1, x_2, ..., x_n) = 0$$
$$F_2(x_1, x_2, ..., x_n) = 0$$
$$\vdots \tag{47}$$
$$F_n(x_1, x_2, ..., x_n) = 0$$

If we consider F to be a vector function comprised of $F_1, F_2, ..., F_n$, and x to be a vector function comprised of $x_1, x_2, ..., x_{n}$, then the above system of equations can be written simply as

$$F(x) = 0 \tag{48}$$

Newton's method for such a vector $F(x)$ can be written analogous to that for a scalar equation and solved as

$$x^{m+1} = x^m - [F'(x^m)]^{-1}\ F(x^m) \tag{49}$$

In the above equation, $F'(x)$ is the Jacobian matrix of the vector $F(x)$ given by

$$F'(x) = \begin{bmatrix} a_{11}(x) & a_{12}(x) & \cdots & a_{1n}(x) \\ a_{21}(x) & a_{22}(x) & \cdots & a_{2n}(x) \\ \vdots & \vdots & & \vdots \\ a_{n1}(x) & a_{n2}(x) & \cdots & a_{nn}(x) \end{bmatrix} \tag{50}$$

where the elements of the Jacobian matrix are given by

$$a_{ij}(x) = \frac{\partial F_i(x)}{\partial x_j} \tag{51}$$

That is, the $(ij)^{th}$ element of the Jacobian is given by the change in the ith element of the vector function $F(x)$ for a given change in the jth dependent variable. Because it is usually impractical to obtain the matrix inverse as the iteration proceeds, Newton's method is usually implemented as[30]

$$F'(x^m)(x^{m+1} - x^m) = -F(x^m) \tag{52}$$

Now consider the vector function $F(x)$ to instead be $F(q)$, where the function $F(q)$ is given by Eqs. (1) – (5). For example, the first element of $F(q)$ is given by

$$F_1 = \frac{\partial}{\partial t}(\varrho_e u_e \delta^*) - u_e \frac{\partial}{\partial t}(\varrho_e \theta_\varrho) + \frac{1}{R^k}\frac{\partial}{\partial x}(\varrho_e u_e^2 R^k \theta) + \varrho_e u_e \delta^* \frac{\partial u_e}{\partial x} - \varrho_e u_e^2 \frac{c_f}{2} = 0 \tag{53}$$

In implementing the implicit scheme, the formulation involving pressure (p_e) as a dependent variable was used. Thus, the dependent variable vector is given by

$$q = (\varrho_e \quad u_e \quad p_e \quad \theta \quad \overline{H})^T \tag{54}$$

The remaining elements of $F(q)$ are defined by referring to Eqs. (2) – (5). The approach is to now discretize these functions using first–order backward temporal differences (implicit Euler) and se-cond–order central spatial differences, where the spatial differences are written at the (implicit) n+1 time level. This results in

$$F_1 = \left[\frac{(\varrho_e u_e \delta^*)_i^{n+1} - (\varrho_e u_e \delta^*)_i^n}{\Delta t}\right] - (u_e)_i^{n+1}\left[\frac{(\varrho_e \theta_\varrho)_i^{n+1} - (\varrho_e \theta_\varrho)_i^n}{\Delta t}\right]$$

$$+ \left(\frac{1}{R^k}\right)_i^{n+1}\left[\frac{(\varrho_e u_e^2 R^k \theta)_{i+1}^{n+1} - (\varrho_e u_e^2 R^k \theta)_{i-1}^{n+1}}{x_{i+1} - x_{i-1}}\right] + (\varrho_e u_e \delta^*)_i^{n+1}\left[\frac{(u_e)_{i+1}^{n+1} - (u_e)_{i-1}^{n+1}}{x_{i+1} - x_{i-1}}\right]$$

$$- \left(\varrho_e u_e^2 \frac{c_f}{2}\right)_i^{n+1} = 0 \tag{55}$$

$$F_2 = \frac{[\varrho_e u_e^2(\theta + \delta^* - \theta_\varrho)]_i^{n+1} - [\varrho_e u_e^2(\theta + \delta^* - \theta_\varrho)]_i^n}{\Delta t} + \left(2\varrho_e u_e(\theta_\varrho - \delta_u^*)\right)_i^{n+1}$$

$$\left[\frac{(u_e)_i^{n+1} - (u_e)_i^n}{\Delta t}\right] + \left(\frac{1}{R^k}\right)_i^{n+1}\left[\frac{(\varrho_e u_e^3 R^k \theta^*)_{i+1}^{n+1} - (\varrho_e u_e^3 R^k \theta^*)_{i-1}^{n+1}}{x_{i+1} - x_{i-1}}\right]$$

$$+ \left(2\varrho_e u_e^2(\delta^* - \delta_u^*)\right)_i^{n+1}\left[\frac{(u_e)_{i+1}^{n+1} - (u_e)_{i-1}^{n+1}}{x_{i+1} - x_{i-1}}\right] - \left(2\varrho_e u_e^3 \frac{c_D}{2}\right)_i^{n+1} = 0 \tag{56}$$

$$F_3 = \frac{(\varrho_e A)_i^{n+1} - (\varrho_e A)_i^n}{\Delta t} + \frac{(\varrho_e u_e A)_{i+1}^{n+1} - (\varrho_e u_e A)_{i-1}^{n+1}}{x_{i+1} - x_{i-1}} = 0 \tag{57}$$

$$F_4 = \frac{(\varrho_e u_e A)_i^{n+1}}{\Delta t} + \frac{[(\varrho_e u_e^2 + p_e)A]_{i+1}^{n+1} - [(\varrho_e u_e^2 + p_e)A]_{i-1}^{n+1}}{x_{i+1} - x_{i-1}}$$

$$- (p_e)_i^{n+1}\left[\frac{(A)_{i+1}^{n+1} - (A)_{i-1}^{n+1}}{x_{i+1} - x_{i-1}}\right] = 0 \tag{58}$$

$$F_5 = \frac{(E_e A)_i^{n+1} - (E_e A)_i^n}{\Delta t} + (p_e)_i^{n+1}\left[\frac{(A)_i^{n+1} - (A)_i^n}{\Delta t}\right]$$

$$+ \frac{[u_e(E_e + p_e)A]_{i+1}^{n+1} - [u_e(E_e + p_e)A]_{i-1}^{n+1}}{x_{i+1} - x_{i-1}} = 0 \tag{59}$$

Of course, we assume that variables at time level n are known and we seek to solve for those at time level n+1. Therefore, within the framework of a Newton iteration, variables at the n time level are constant. However, each function $F(q)$ above depends upon values of the dependent variable vector at spatial grid points i, i+1, i–1, all at the n+1 time level. Thus, we can write

30

$$F(q^{n+1}) = F(q_{i-1}^{n+1}, \; q_i^{n+1}, \; q_{i+1}^{n+1}) \tag{60}$$

A Taylor's series expansion of $F\,(q^{n+1})$ in three variables results in the expression

$$F(q_{i+1}^{n+1} + \Delta q_{i+1}^{n+1}, \; q_i^{n+1} + \Delta q_i^{n+1}, \; q_{i-1}^{n+1} + \Delta q_{i-1}^{n+1})$$

$$= F(q_{i+1}^{n+1,m}, \; q_i^{n+1,m}, \; q_{i-1}^{n+1,m}) + \left(\frac{\partial F}{\partial q_{i+1}^{n+1}}\right)^m \Delta q_{i+1}^{n+1,m} + \left(\frac{\partial F}{\partial q_i^{n+1}}\right)^m \Delta q_i^{n+1,m}$$

$$+ \left(\frac{\partial F}{\partial q_{i-1}^{n+1}}\right)^m \Delta q_{i-1}^{n+1,m} \approx 0 \tag{61}$$

or

$$\left(\frac{\partial F}{\partial q_{i+1}^{n+1}}\right)^m \Delta q_{i+1}^{n+1,m} + \left(\frac{\partial F}{\partial q_i^{n+1}}\right)^m \Delta q_i^{n+1,m} + \left(\frac{\partial F}{\partial q_{i-1}^{n+1}}\right)^m \Delta q_{i-1}^{n+1,m}$$

$$= - F(q_{i+1}^{n+1,m}, q_i^{n+1,m}, q_{i-1}^{n+1,m}) \tag{62}$$

where

$$\Delta q^{n+1,m} \equiv q^{n+1,m+1} - q^{n+1,m} \tag{63}$$

Of course, the objective here is to perform sufficient iterations within a given time step such that

$$\Delta q^{n+1,m} \approx 0 \tag{64a}$$

which gives

$$q^{n+1,m+1} \approx q^{n+1,m} = q^{n+1} \tag{64b}$$

Eq. (62) is the Newton scheme used herein. It should perhaps be referred to as a discretized–Newton scheme because it is the discretized form of the equations to which the method is applied. The equation is written at each interior mesh point which results in a system of block tridiagonal equations, where each block is a 5x5 matrix. A block tridiagonal solver written by Whitfield[16] is used to solve the system of equations.

One should note that forming central differences on a non–uniform grid without the benefit of a curvilinear coordinate transformation has altered the formal second–order accuracy of the spatial discretization. This can be illustrated by considering a continuous function $f(x)$ defined at discrete points x_i and forming Taylor expansions for $f(x_{i+1})$ and $f(x_{i-1})$ about $f(x_i)$, or

31

$$f_{i+1} = f_i + (x_{i+1} - x_i)\left(\frac{\partial f}{\partial x}\right)_i + \frac{1}{2}(x_{i+1} - x_i)^2\left(\frac{\partial^2 f}{\partial x^2}\right)_i + O[(x_{i+1} - x_i)^3]$$

$$f_{i-1} = f_i - (x_i - x_{i-1})\left(\frac{\partial f}{\partial x}\right)_i + \frac{1}{2}(x_i - x_{i-1})^2\left(\frac{\partial^2 f}{\partial x^2}\right)_i - O[(x_i - x_{i-1})^3]$$

Subtracting the latter from the former results in

$$\left(\frac{\partial f}{\partial x}\right)_i = \frac{f_{i+1} - f_{i-1}}{x_{i+1} - x_{i-1}} - \frac{1}{2}\left[\frac{(x_{i+1} - x_i)^2 - (x_i - x_{i-1})^2}{x_{i+1} - x_{i-1}}\right]\left(\frac{\partial^2 f}{\partial x^2}\right)_i$$
$$+ O\left[\frac{(x_{i+1} - x_i)^3}{x_{i+1} - x_{i-1}}, \frac{(x_i - x_{i-1})^3}{x_{i+1} - x_{i-1}}\right]$$

For uniform spacing, the second term on the right–hand–side of the above vanishes and the usual central difference expression results. However, as evidenced by Eqs. (55) – (59), the present scheme simply uses the first term on the right–hand–side of the above and consequently incurs additional discretization error resulting from the non–uniform grid spacing. Fortunately, this additional "non–uniform spacing error" is typically smallest in regions where grid spacing is smallest, and larger elsewhere (at least using the stretching function discussed in Section III.d). Thererfore, the overall additional error will be counter–acted by the second derivative term which will be small if grid points having the largest spacing have been placed in regions where the function is not changing rapidly; i.e., $\partial f/\partial x \approx 0$.

As mentioned above, only the interior points are updated using the Newton iteration. Boundary points are updated in an explicit manner at the conclusion of each complete time step in a manner appropriate with conditions at the boundary (i.e., subsonic inflow, supersonic outflow, etc.), as discussed in Section II.d.

The overall block structure is due to the appearance of the Jacobian matrices. Because of the algebraic complexity of the vector function $F(q)$, the Jacobians are evaluated numerically. This procedure is discussed in the following section.

b. Computation of the Jacobian Matrices

Consider the following evaluation of a Jacobian using the dependent variable vector at the ith mesh point:

$$\left(\frac{\partial F}{\partial q}\right)_i = \frac{\partial (F_1, F_2, F_3, F_4, F_5)_i^T}{\partial (q_1, q_2, q_3, q_4, q_5)_i^T} \tag{65}$$

where

$$(q_1, q_2, q_3, q_4, q_5)^T = (\varrho_e, u_e, p_e, \theta, \bar{H})^T \tag{66}$$

Therefore, we can write the $(rs)^{th}$ element of the Jacobian at the ith grid point (at the mth iterate) as

$$\left(\frac{\partial F}{\partial q_i^{n+1}}\right)_{rs}^m = \frac{\partial F_r}{\partial q_{s,i}^{n+1}} = \frac{F_r(q_{s,i+1}^{n+1,m}, q_{s,i}^{n+1,m} + \varepsilon, q_{s,i-1}^{n+1,m}) - F_r(q_{s,i+1}^{n+1,m}, q_{s,i}^{n+1,m}, q_{s,i-1}^{n+1,m})}{\varepsilon} \tag{67}$$

The above relation states that at the ith axial location, the $(rs)^{th}$ element is computed by evaluating the change in the rth component of $F(q)$ due to a given change in the sth component of q, holding $q_{s,i+1}$, $q_{s,i-1}$ at their current m^{th}–iterate values.

The value of ε used to compute the Jacobians as described above was approximately one–half of the reliable digits associated with the machine on which the code is executed, as suggested by Whitfield[34]. All solutions using the discretized–Newton scheme presented in this section were obtained on a Silicon Graphics, Inc. 4d/460 Power IRIS using double–precision floating–point operations. Therefore, for the present effort, $\varepsilon \approx 10^{-6}$.

As might be anticipated, computation of the Jacobian matrices is rather expensive from an operation count point–of–view, particularly when considering that they appear within the Newton iteration; i.e., they should be recomputed at each m–iterate. However, it has been observed that convergence is not degraded significantly if the Jacobian updates occur infrequently. In fact, solutions presented here were obtained by updating the Jacobians about every five time–steps, where a time–step may include several m–iterations. This method of Jacobian updating drastically reduces the overall computational resource requirements. Note that this approximation only affects the convergence (i.e., to make $\Delta q^{n+1,m} \approx 0$) at a particular time step and has no effect upon the time accuracy of the

33

scheme. This is because the right–hand–side of Eq. (62) is only affected by the discretization error associated with the temporal and spatial difference operators used in the original discretization process (in this case, first–order in time and second–order in space).

c. Dissipation Model

As stated above, second–order central differences were used for spatial discretization. As such, insufficient numerical damping is present which results in significant under– and overshoots in regions where the dependent variables exhibit near–discontinuous behavior (e.g., shocks). Therefore, additional artificial dissipation was needed to suppress these unwanted oscillations.

Although several dissipation models have been tried (e.g., that used by Warming and Beam[20]), the model proposed by Davis[35] has been the only one which yields the desired results. This is a "TVD–based" (total variation diminishing) model which determines the level of added dissipation using local flowfield conditions. The development of this model was motivated by the need to improve shock capturing capabilities of explicit schemes while preserving the simplicity of these methods. Much improved solutions were reported by Davis[35] in solving the two–dimensional Euler equations, and also by Causon[36] who used the model in three–dimensional inviscid flows, where the MacCormack scheme was used in both studies[35,36].

For the present discretized–Newton scheme, the additional dissipation was added to the dependent variable vector at the end of each Newton iteration (i.e., after each m–iterate). Although adding the dissipation at various other stages was tried, it was determined that adding it after each Newton iteration was the most robust and gave the overall best results. The model as implemented herein is given by the following step–by–step procedure:

$$[q_i^{n+1,m+1}]_{smoothed} = [q_i^{n+1,m+1}]_{unsmoothed} + \delta q_{diss}^m \qquad (68)$$

where

34

$$\delta q^m_{diss} = (G_i^+ + G_{i+1}^-)(q^m_{i+1} - q^m_i) - (G_{i-1}^+ + G_i^-)(q^m_i - q^m_{i-1})$$

$$G_i^\pm = G(r_i^\pm) = 1/2C(v)[1 - \emptyset(r_i^\pm)]$$

$$C(v) = \begin{cases} v(1 - v), & v \leq 0.5 \\ 0.25, & v > 0.5 \end{cases}$$

$$v = v_i = (CFL)_i$$

$$(CFL)_i = |\lambda_i| \left(\frac{\Delta t}{\Delta x}\right)_i \qquad (69)$$

$$r_i^+ = \frac{\left\langle \left(q^m_{i+1} - q^m_i\right), \left(q^m_i - q^m_{i-1}\right)\right\rangle}{\left\langle \left(q^m_{i+1} - q^m_i\right), \left(q^m_{i+1} - q^m_i\right)\right\rangle}$$

$$r_i^- = \frac{\left\langle \left(q^m_{i+1} - q^m_i\right), \left(q^m_i - q^m_{i-1}\right)\right\rangle}{\left\langle \left(q^m_i - q^m_{i-1}\right), \left(q^m_i - q^m_{i-1}\right)\right\rangle}$$

$$\emptyset(r) = \min[\mathrm{mod}(2r, 1)] = \max(0, \min(2r, 1))$$

where $\langle$ a , b $\rangle$ is a scalar product of a and b, and λ is the maximum local eigenvalue.

d. Results

This section presents comparisons between measured[31] and computed results for steady, transonic converging–diverging planar channel flow for both symmetric and asymmetric configurations. In addition to results obtained by the present discretized–Newton scheme (hereafter designated BL1D–I), calculations ensuing from both Navier–Stokes (the same code previously discussed) and a Q1D Euler solver[37] are compared with the measurements. Solutions obtained with the discretized–Newton scheme were obtained using a Silicon Graphics, Inc. 4d/460 Power IRIS. Again, few attempts have been made to optimize the code for fast execution which proceeds at a rate of 0.018 cpu–sec per grid–point per time–step. Calculations from BL1D–I were obtained from an impulsive start by initializing the dependent variables to specified values and then marching in time to a steady–state.

With regard to the comparisons which follow, the reader should note that:

35

1. x = 0 refers to the beginning of the convergent section.

2. All lengths have been non–dimensionalized with h_t, where $h_t = 0.1$ meter for Case 1.2 and $h_t = 0.096$ meter for Case 1.3.

3. Static pressures are plotted as a ratio of local static to reference stagnation pressure (where $\hat{p}_{0,\infty} = 96$ kPA).

4. Velocities are non–dimensionalized by the quantity $u_{e,max}$, where $u_{e,max}=418$ meters/second for Case 1.2 and $u_{e,max}=403$ meters/second for Case 1.3.

Case 1.2 (Symmetric)

A schematic of the experimental apparatus (which is symmetric) is shown in Fig. 16a. In attempting to computationally simulate the flowfield within a given physical configuration, it is important that all pertinent information about the experiment be given. Unfortunately, a complete description of the test apparatus was not provided in Ref. 31. In particular, the length of the section between the reservoir and the beginning of the converging section, as well as the distance between the diverging section and second throat, were not specified. Therefore, certain lengths had to be estimated where both estimated and actual values are shown in Fig. 16a. Inlet stagnation pressure and temperature were specified as $\hat{p}_{0,\infty} = 96$ kPA and $\hat{T}_{0,\infty} = 300$ K, respectively. These conditions resulted in a reference unit Reynolds number of 5.345×10^5 per meter. Also, the reference length was defined to be $\hat{R}_{ref} = 50$ mm.

For the present computations, 51 axial points were used where the points were clustered in the region of the shock. The clustering was accomplished using a hyperbolic tangent stretching function given by

$$x' = 1 + \frac{\tanh[\delta(\xi - 1)]}{\tanh(\delta)}$$

where

$$\xi = \frac{x - 1}{N_{max} - 1}$$

Here δ is a scale factor that controls spacing and N_{max} is the number of axial grid points. Use of such a stretching function allows a significant reduction in the number of grid points while maintaining good resolution in regions of high gradients.

Comparisons between measured and computed wall static pressure distributions are shown in Fig. 16b. Symbols represent measured values whereas the solid line shows the computed distribution from the B11D–I code. Also shown for comparison is the computed pressure distribution using the inviscid method of Ref. 37. Both measurements and calculations indicate the presence of a shock of moderate strength. Similar to the subsonic calculations discussed in Section II, the exit static pressure in the computations was adjusted in order to match the measurements at some other axial location. In this case, the exit pressure was set such that the computed shock location was very near that indicated by the experimental data. Although both computational techniques show a reluctance to expand as quickly as do the measurements upstream of the shock, the inviscid calculations show a much higher rate of compression through and downstream of the shock than do those computed by the BL1D–I code. This "relaxing" effect is due to the presence of the boundary layer which, of course, the purely inviscid method cannot simulate.

Shown in Fig. 16c is the computed skin friction distribution for this case. Whereas no experimentally determined values are available for comparison, Navier–Stokes results are shown and are seen to qualitatively agree with those computed by BL1D–I, although the separation points and the regions over which separation occurs are considerably different. Note that the computed distributions of c_f from both computational techniques are not smooth. In BL1D–I, this is due to similar behavior of the calculated "incompressible" shape factor $\overline{H}$, which is shown in Fig. 16d along with the measured distribution of this parameter. Although the computed distribution of $\overline{H}$ appears fairly smooth in Fig. 16d, a scaled–up plot shows significant "wiggles" exist upstream of the shock (many attempts to eliminate such oscillations have thus far been unsuccessful). The regions of experimentally and computationally determined reverse flow are shown in Fig. 16d as the shaded and open areas, respectively. Further illustrations of this reverse flow are given in Fig. 16e which show measured and computed boundary–layer velocity profiles upstream and within the separated region, as well as at reattachment. Also shown for comparison are Navier–Stokes calculations for the same configuration. While the Navier–Stokes results show a clear superiority over those computed by BL1D–I, the latter technique is seen to capture the overall trends inferred by the measurements.

Finally, Fig. 16f presents a comparison of measured and computed displacement surfaces within the perspective of the experimental test section. It should be noted that the vertical and horizontal scales of this figure are different which gives a distorted view of the minimum area region. It can be seen that computed results indicate a displacement surface considerably larger than that measured, although the overall qualitative trends associated with rapid boundary–layer growth downstream of the shock are reasonable. One should note that the computed displacement thickness within the separated region grows to approximately 40% of the local channel half–height which implies that the viscous region occupies most of the channel (i.e., that the flow is fully developed). However, as shown by the velocity profiles in Fig. 16e, the rapid increase in displacement thickness can be attributed to the fact that the velocity ratio u/u_e is highly retarded over a significant distance from the wall, thus increasing the quantity $1-u/u_e$ used in computing the displacement thickness. Therefore, the flow should not be considered fully developed and that an inviscid core does exist (which can be verified from the velocity profiles shown in Fig. 16e).

Case 1.3 (Asymmetric)

The physical configuration for this case is similar to that given above except that the channel is now non–symmetric. Again, a complete description of the test apparatus was not provided, thus making it necessary to estimate the distance from the upstream reservoir to test section entrance. The experimental apparatus is presented in Fig. 17a which shows an airfoil–like blockage, but is on the lower wall only. Also shown in this figure is the computational domain used for the present calculations. In reality, this is a two–dimensional configuration which, of course, cannot be completely simulated using the Q1D approximation. However, because a large portion of internal flow configurations possess some asymmetries, it is of interest to compare results from non–symmetric measurements with those generated using the Q1D approximation in order to provide some measure of the validity with regard to using the Q1D approach, particularly for transonic flow.

Shown in Fig. 17b are the actual and equivalent nozzle contours. The equivalent contour was generated by using the actual area and deducing from this the required channel half–height distribution.

It can be seen that the effect of this "transformation" has been to lessen the wall slopes over the entire airfoil region, particularly at the aft end where the airfoil and tunnel wall coincide.

Illustrated in Fig. 17c are comparisons between measured and computed static pressures where the experimental data shown were obtained on the lower wall (refer to Fig. 17a) whereas those computed result from use of the equivalent channel as discussed above (Navier–Stokes results were not available for this case). Also shown for comparison are wall pressures computed using the inviscid equations[37]. Similar to the symmetric case, both computational schemes produce reasonable results upstream of the shock, and again the inviscid computations indicate a more rapid compression downstream of the shock than do those associated with the present interaction scheme. Computed pressures from the present scheme again exhibit "wiggles", but the oscillations seem to diminish axially downstream. It is important to note that the exit pressure for both inviscid and interaction calculations were adjusted such that the computed shock location approximated that observed on the lower wall. For both calculations, the use of an equivalent area distribution has the effect of under–expanding the flow in the region upstream of the shock. This is not surprising because the measured flowfield "sees" a larger disturbance on the lower wall than that within the equivalent channel.

Two–dimensional effects are shown in Fig. 17d which illustrates measured and computed pressures for both upper and lower walls. It can be seen that significant differences exist between measured upper and lower wall pressures and that the present calculations tend to represent an average of those measured, except with regard to shock location. This figure further amplifies the previous observation that the equivalent channel (Q1D) approximation has the effect of causing a weaker shock (at approximately the same axial location as that observed on the lower wall).

Similar to Case 1.2, a large region of separated flow was measured which is also predicted by the computations. Figure 17e shows computed skin friction which illustrates the region over which boundary–layer separation occurs in the calculations. The severity of the measured separation region is further illustrated in Fig. 17f which presents measured and computed shape factor ($\overline{H}$) distributions. It can be seen that the calculated values of this parameter fall short of those measured

within the separated region. The reason for this underprediction is shown in Fig. 17g which illustrates measured and computed velocity profiles as selected locations in the vicinity of the separated region. It can be seen that reverse flow regions associated with computed profiles are not as severe as those measured, thus accounting for the large shape factor. In addition, a correspondingly large displacement surface compared to the complications is shown in Fig. 17h. Whereas the computed displacement surface downstream of the shock is less than that measured, the calculations are considered reasonable. This is particularly true when one considers the level of approximation used in the computational method. Similar to Case 1.2, this case does not appear to be fully developed thus allowing the present interaction method to be applicable, at least for these flow conditions.

IV. SUMMARY AND CONCLUSIONS

Viscous–inviscid interacting internal flowfields have been computed for subsonic, transonic, and supersonic quasi–one–dimensional (Q1D) configurations. Viscous–inviscid interaction was achieved by directly coupling the unsteady Q1D Euler equations with integral boundary–layer equations for unsteady, two–dimensional, turbulent flow over impermeable, adiabatic walls. The coupling methodology differs from that used in the past in that the coupling is carried out directly through the equations as opposed to solutions of the different equation sets. Numerical solutions to the coupled system of equations were obtained using the explicit MacCormack scheme as well as an implicit discretized–Newton scheme. Computed solutions have been compared with measurements as well as Navier–Stokes and inverse boundary–layer methods. Although differences exist between measurements and solutions computed from the Q1D approach, and also between those computed by other methods, overall qualitative trends for both steady and unsteady test cases are predicted with reasonable reliability.

An analysis of the eigenvalues of the coefficient matrix associated with the quasi–linear form of the coupled system of equations used in the Q1D approach indicates the presence of complex eigenvalues for certain flow conditions (in particular, values of shape factor, H, high enough to cause boundary–layer separation) thus allowing exponential growth in the solution(s). Although reasonable solutions are obtained numerically, it is believed these complex eigenvalues contribute to the overall difficulty observed in obtaining numerical solutions to the coupled system of equations. It is further postulated that these complex eigenvalues are a result of empirical and analytical approximations used in the integral boundary–layer technique.

The original formulation of the system of equations[7] (for use in the explicit scheme) made the assumption that stagnation temperature was constant from the upstream reservoir reference state to that associated with local conditions. However, this assumption was shown to be inconsistent within the context of unsteady flow, even for the case of no heat transfer. As a result, new formulations of the equations were derived which do not depend upon an assumption of constant stagnation temperature. It was shown that the degree of error associated with the original formulation was small,

at least for the case considered. However, this error will increase in direct proportion with the degree of unsteadiness associated with a particular flowfield.

Comparisons between computations using the Q1D approach and those resulting from a Navier–Stokes analysis show generally good agreement with regard to the overall qualitative aspects of the flowfield. Some of the observed discrepancies can be attributed to improper interpretation of the two–dimensional Navier–Stokes results from the perspective of quasi–one–dimensional physics. In particular, locating the boundary–layer edge in a Navier–Stokes generated velocity profile proved to be the "Achilles heal" of the comparison process. Nevertheless, results generated from the Q1D approach for both steady and unsteady supersonic channel flows are considered good enough to provide preliminary estimates of internal flowfield behavior, at least for configurations of the type considered herein.

Implementation of an implicit discretized–Newton scheme for numerically solving the coupled system of equations was originally motivated from the standpoint of numerical stability. This was deemed necessary for the method to be capable of addressing transonic flow; i.e., flows with shocks. However, as stated above, appearance of complex eigenvalues for the coupled system gives rise to possible exponential solution growth due to the equations being ill–posed for solution in time as an initial/boundary–value problem, at least in certain flow regimes. In spite of this, reasonable steady–state solutions have been obtained, even for highly separated flows (i.e., for very high values of $\overline{H}$). It is concluded that even though the equations appear to be ill–posed in these regions, growth of error is slow enough to allow reasonable solutions.

It is acknowledged that "there's nothing more dangerous than answers that look about right," and that more study is warranted with regard to both unsteady and multi–dimensional flow, simulation using the Q1D approach. However, it is felt that the Q1D approach is valid and the tools generated by this effort are useful in the regimes which have been investigated, particularly when considering the computational resources required to generate results from other methods. For example, the Navier–Stokes code used in these studies executes at approximately 6.0×10^{-5} cpu–sec per time–step

per grid point on a CRAY Y–MP. Therefore, for 3,000 time steps and the grid used (185 x 30 x 2), this resulted in approximately 30 cpu minutes on this machine. As stated earlier, all Q1D–based codes were executed on engineering workstation–based hardware and required much less computational time to execute. As stated in the Introduction, whether or not the Q1D approach is appropriate is greatly problem dependent, as evidenced from the steady–state nozzle results which was inherently two–dimensional within the nozzle contraction/expansion region. If preliminary, engineering accuracy results will suffice, results shown herein indicate that this can be achieved using this approach.

REFERENCES

[1] Whitfield, D.L., Swafford, T.W., Janus, J.M., Mulac, R.A., and Belk, D.M., "Three–Dimensional Unsteady Euler Solutions for Propfans and Counter–Rotating Propfans in Transonic Flow," AIAA–87–1197, June 1987.

[2] Hirsch, C., *Numerical Computation of Internal and External Flows, Volume 1: Fundamentals of Numerical Discretization*, John Wiley and Sons, New York, 1988.

[3] Whitfield, D.L., Swafford, T.W., and Jacocks, J.L., "Calculation of Turbulent Boundary Layers with Separation and Viscous–Inviscid Interaction," *AIAA Journal*, Vol. 19, No. 10, October 1981, pp. 1315–1322.

[4] Swafford, T.W., "Computation of Unsteady Supersonic Quasi–One–Dimensional Viscous–Inviscid Interacting Internal Flowfields," *AIAA Journal*, to be published.

[5] Cebeci, T. and Smith, A.M.O., *Analysis of Turbulent Boundary Layers*, Academic Press, New York, 1974.

[6] Whitfield, D.L., "Integral Solution of Compressible Turbulent Boundary Layers Using Improved Velocity Profiles," AEDC–TR–78–42, Arnold AFB, TN, December 1978.

[7] Swafford, T.W., "Unsteady Viscous/Inviscid Interaction via Direct Coupling of the 1d–Euler and 2d–Integral Boundary–Layer Equations," Mississippi State Engineering and Industrial Research Station Report MSSU–EIRS–ERC–90–1, March 1991.

[8] Carter, J.E., "A New Boundary–Layer Inviscid Interaction Technique for Separated Flow," AIAA–79–1450, July 1979.

[9] Kuhn, G.D., "Calculation of Separated Turbulent Flows on Axisymmetric Afterbodies Including Exhaust Plume Effects," *AIAA Journal*, Vol. 18, March 1980, pp. 235–242.

[10] Swafford, T.W., "Time–Dependent, Inverse Solution of Three–Dimensional, Compressible, Turbulent, Integral Boundary–Layer Equations in Nonorthogonal Curvilinear Coordinates," *Lecture Notes in Physics*, Vol. 218, pp. 541–545, 1985.

[11] Moses, H.L., Jones III, R.R., and O'Brien Jr., W.F., "Simultaneous Solution of the Boundary Layer and Freestream with Separated Flow," *AIAA Journal*, Vol. 16, No.1, January 1978, pp. 61–66.

[12] Press, W.H., Flannery, B.P., Teukolsky, S.A., and Vettering, W.T., *Numerical Recipes: The Art of Scientific Computing*, Cambridge University Press, New York, pp. 365–376, 1986.

[13] Briley, W.R. and McDonald, H., "Three–Dimensional Viscous Flows with Large Secondary Velocity," *Journal of Fluid Mechanics*, Vol. 144, 1984, pp. 47–77.

[14] Garabedian, P.R., *Partial Differential Equations*, John Wiley and Sons, 1964.

[15] Briley, W.R., Engineering Research Center for Computational Field Simulation, Mississippi State University, June 1992, Private Communication.

[16] Whitfield, D.L., Engineering Research Center for Computational Field Simulation, Mississippi State University, June 1992, Private Communication.

[17] Swafford, T.W. and Whitfield, D.L., "Time–Dependent Solutions of Three–Dimensional Compressible Turbulent Integral Boundary–Layer Equations," *AIAA Journal*, Vol. 23, No. 7, pp. 1005–1013, July 1985.

[18] Donegan, T.L., "Unsteady Viscous–Inviscid Interaction Procedures for Transonic Airfoil Flows," MS Thesis, The University of Tennessee, Knoxville, TN, December 1983.

[19] MacCormack, R.W., "The Effect of Viscosity in Hypervelocity Impact Cratering," AIAA–69–354, 1969.

[20] Warming, R.F. and Beam, R.M., "Upwind Second–Order Difference Schemes and Applications in Aerodynamic Flows," *AIAA Journal*, Vol. 14, No. 9, pp. 1241–1249, September 1976.

[21]Cooper, G.K. and Sirbaugh, J.R., "The PARC Distinction: A Practical Flow Simulator," AIAA Paper No. 90–2002. AIAA 27th AIAA/SAE/ASME Joint Propulsion Conference, Orlando, Florida, 1990.

[22]Little, B.H., Jr. and Wilbur, Stafford, W., "Performance and Boundary–Layer Data from 12° and 23° Conical Diffusers of Area Ratio 2.0 at Mach Numbers Up To Choking and Reynolds Number Up To 7.5 X 10^6," NACA Report 1201, 1954.

[23]Whitfield, D.L., Swafford, T.W., and Donegan, T.L., "An Inverse Integral Computational Method for Compressible Turbulent Boundary Layers," *Recent Contributions to Fluid Mechanics*, Edited by W. Haase, Springer–Verlag, 1982, pp. 294–302.

[24]Whitfield, D.L., Janus, J.M, and Simpson, L.B., "Implicit Finite Volume High Resolution Wave–Split Scheme for Solving the Unsteady Three–Dimensional Euler and Navier–Stokes Equations on Stationary or Dynamic Grids," Engineering and Industrial Research Station Report MSSU–EIRS–ASE–88–2, Mississippi State University, February 1988.

[25]Simpson, L. Bruce and Whitfield, David L., "Flux–Difference Split Algorithm for Unsteady Thin–Layer Navier–Stokes Solutions," *AIAA Journal*, Vol. 30, No. 4, April 1992, pp. 914–922.

[26]Arabshahi, A. and Whitfield, D.L., "A Multiblock Approach to Solving the Three–Dimensional Unsteady Euler Equations about a Wing–Pylon–Store Configuration," AIAA–89–3401–CP, June 1989.

[27]Roe, P.L., "Approximate Riemann Solvers, Parameter Vector, and Difference Schemes," *Journal of Computational Physics*, Vol. 43, p. 357, 1981.

[28]Osher, S. and Chakravarthy, S., "Very High Order Accurate TVD Schemes," ICASE Report No. 84–44, Sept. 1984.

[29]Steger, J.L. and Warming, R.F., "Flux Vector Splitting of the Inviscid Gasdynamic Equations with Applications to Finite Difference Methods," *Journal of Computational Physics*, Vol. 40, pp. 263–293, 1981.

[30]Whitfield, D.L., "Newton–Relaxation Schemes for Nonlinear Hyperbolic Systems," Engineering and Industrial Research Station Report, Mississippi State University, No. MSSU–EIRS–ASE–90–3, October 1990.

[31]*Advisory Group for Aerospace Research and Development (AGARD)*, Air Intakes for High Speed Vehicles, Section 3.3.1, Test Case 1, Transonic Normal Shock/Boundary Layer Interactions, AGARD Advisory Report 270, Fluid Dynamics Panel Working Group 13, September 1991.

[32]Briley, W.R. and McDonald, H., "Solutions of the Multidimensional Compressible Navier–Stokes Equations by a Generalized Implicit Method," *Journal of Computational Physics*, Vol. 24, pp. 372–397, 1977.

[33]Beam, R.M. and Warming, R.F., "An Implicit Finite–Difference Algorithm for Hyperbolic Systems in Conservation Law Form," *Journal of Computational Physics*, Vol. 22, pp. 87–110, 1976.

[34]Whitfield, David L. and Taylor, Lafe K., "Discretized Newton–Relaxation Solution of High Resolution Flux–Difference Split Schemes," AIAA–91–1539–CP, June 1991.

[35]Davis, Stephen F., "TVD Finite Difference Schemes and Artificial Viscosity," NASA–CR–172373 (ICASE Report No. 84–20), June 1984.

[36]Causon, D.M., "A Total Variation Diminishing Scheme for Computational Aerodynamics," *Numerical Methods for Fluid Dynamics III*, Edited by K.W. Morton and M.J. Baines, Clarendon Press, Oxford, pp. 449–457, 1988.

[37]Stokes, M.L., "A Solution of The Euler Equations on An Unstructured Grid System," PhD Dissertation, The University of Tennessee, Knoxville, Tennessee, May 1990.

[38]Baldwin, B.S. and Lomax, H., "Thin Layer Approximation and Algebraic Model for Separated Turbulent Flows," AIAA Paper No. 78 –257, AIAA 16th Aerospace Sciences Meeting, Huntsville, Alabama, January 1978.

[39]Thomas, P.D., "Numerical Method for Predicting Flow Characteristics and Performance of Non-axisymmetric Nozzles–Theory," Langley Research Center, NASA CR 3147, September 1979.

Figure 1. Generic Channel Configuration
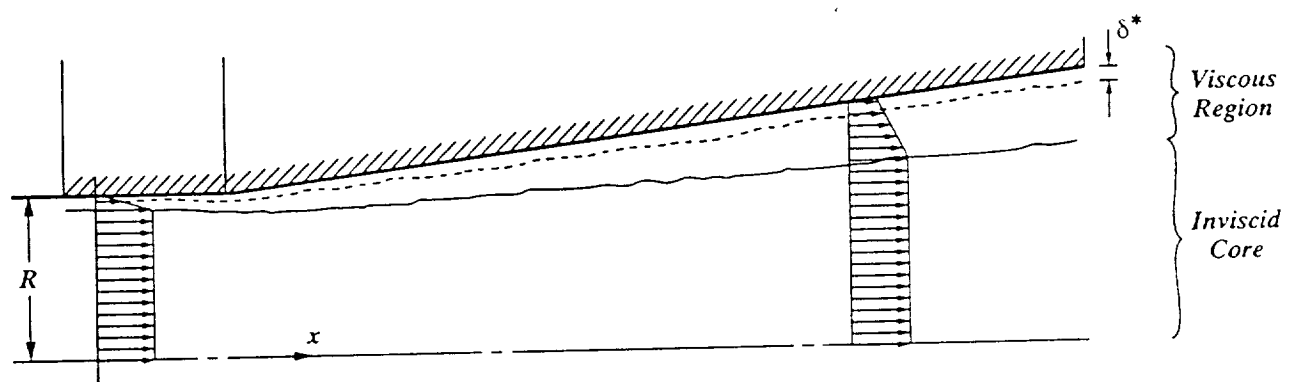
Figure 2. Convergence Histories for Supersonic, Constant-Area Duct (All Formulations)

(a). Mach Number
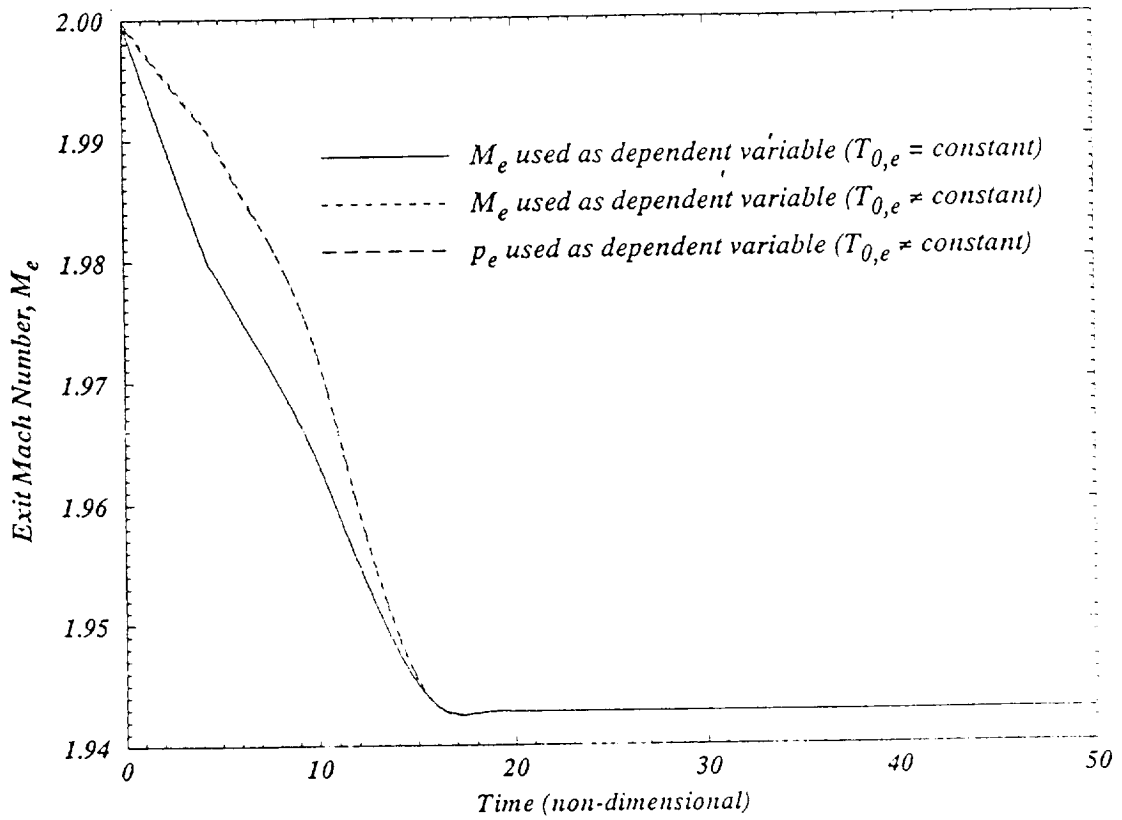
(b). RMS Residual of Velocity
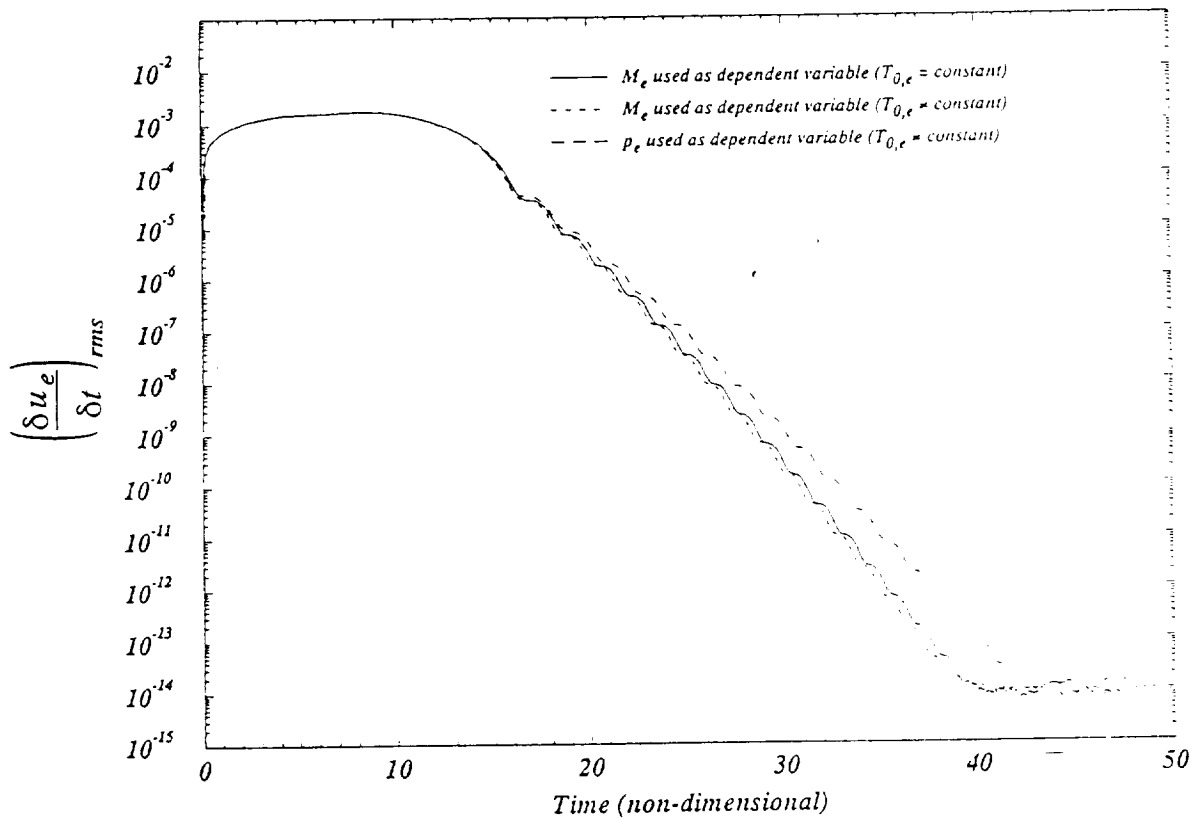
Figure 3. Computed Unsteady Flow Parameters (All Formulations)

(a). Entrance and Exit Core Mach Number
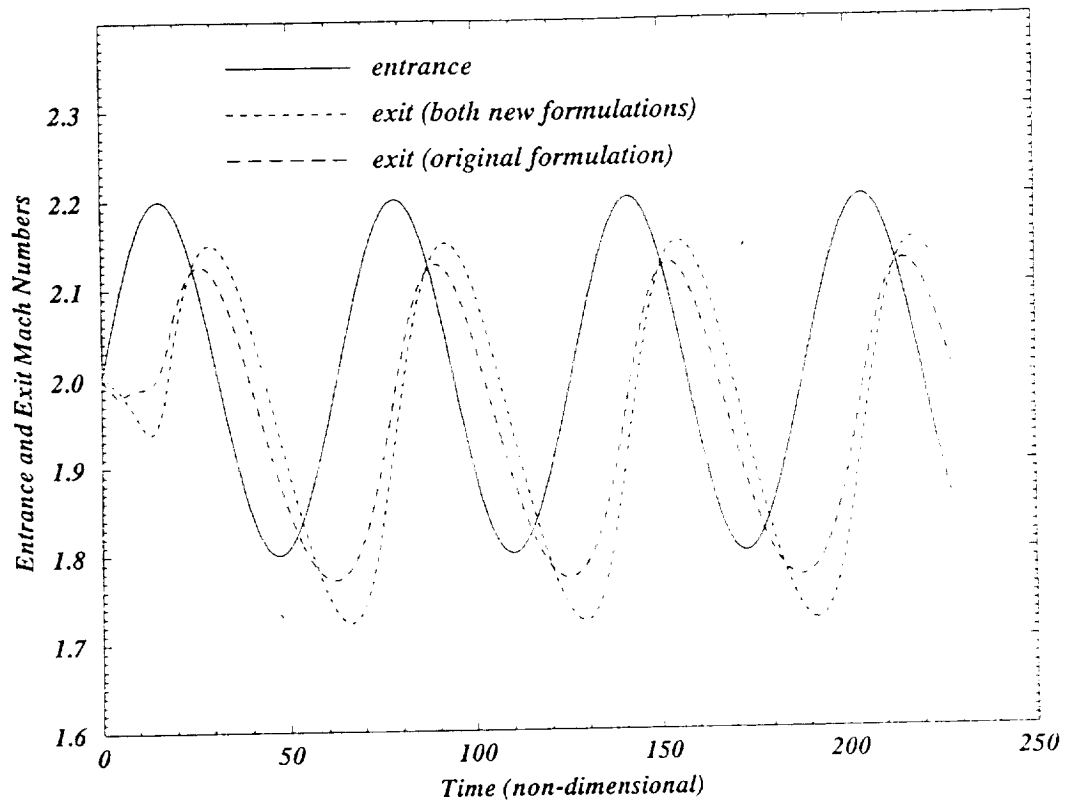
(b). Boundary-Layer Integral Lengths
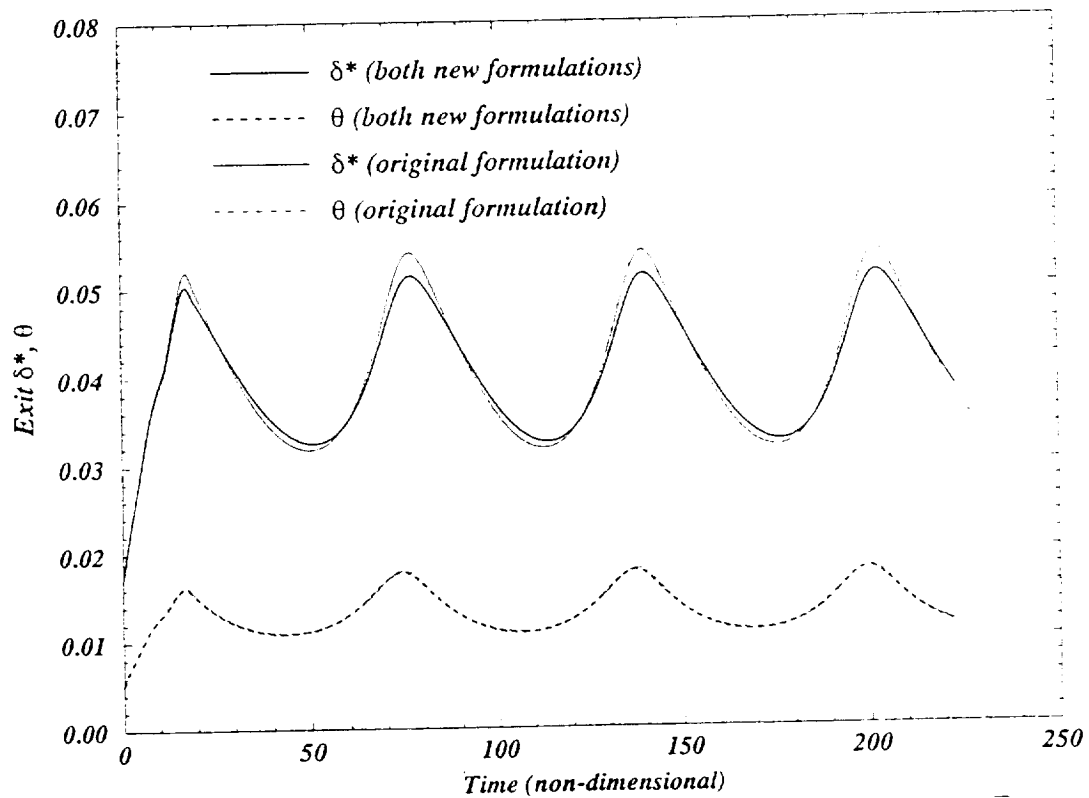
Figure 3. (Continued)

(c). Stagnation Temperature Variation
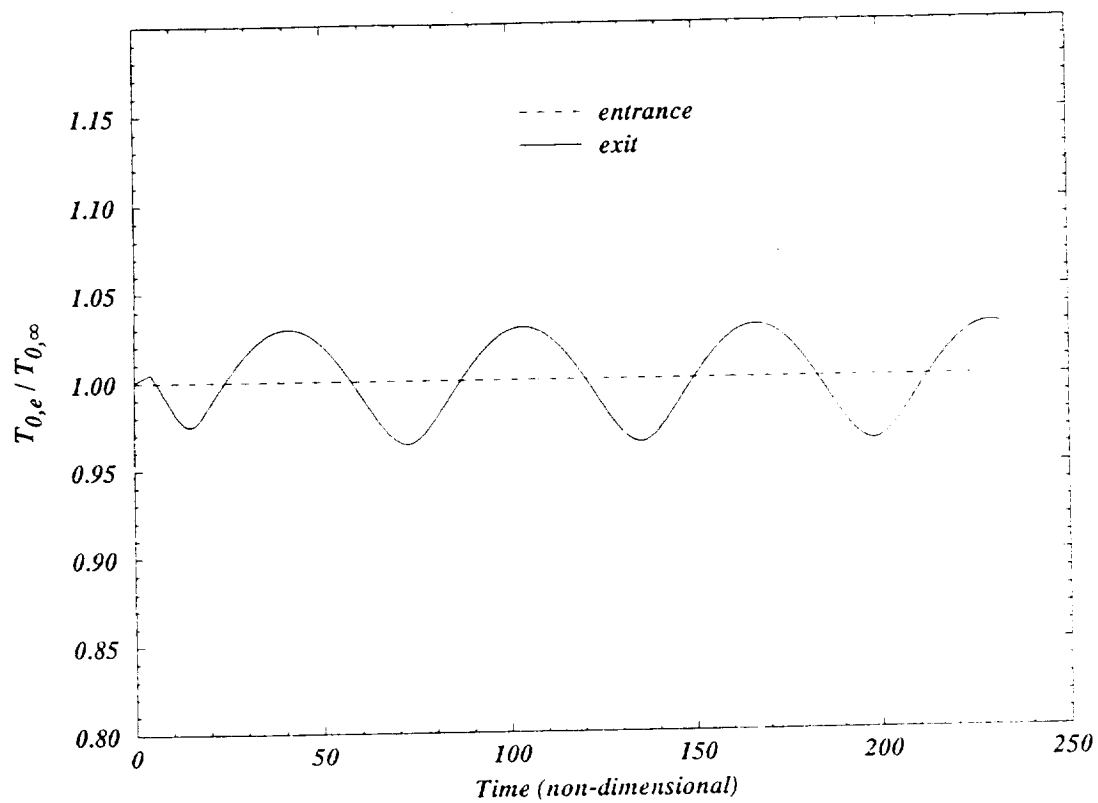
Figure 4. Eigenvalues of $L^{-1} N$ (lines denote eigenvalues of complete system, symbols denote u_e, $u_e + a_e$, $u_e - a_e$)

(a). $\bar{H} = 1.2$, $\theta = 0.001$

(b). $\bar{H} = 1.5$, $\theta = 0.001$

51
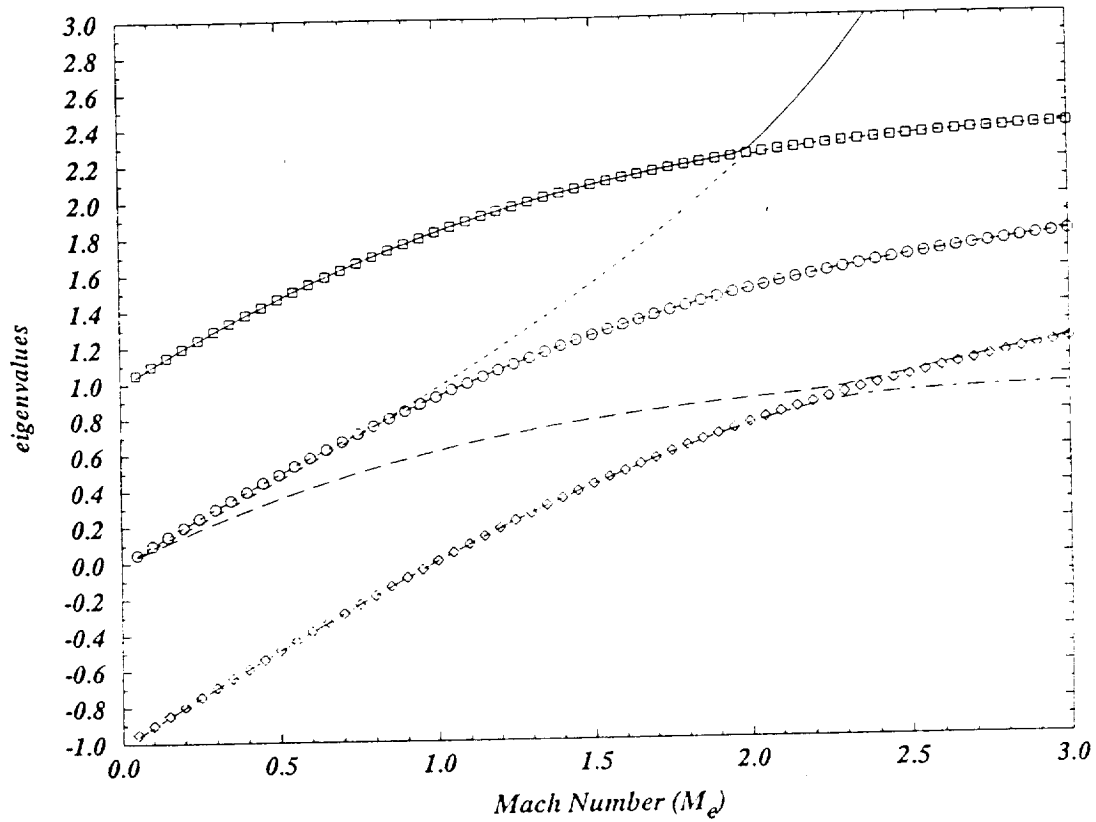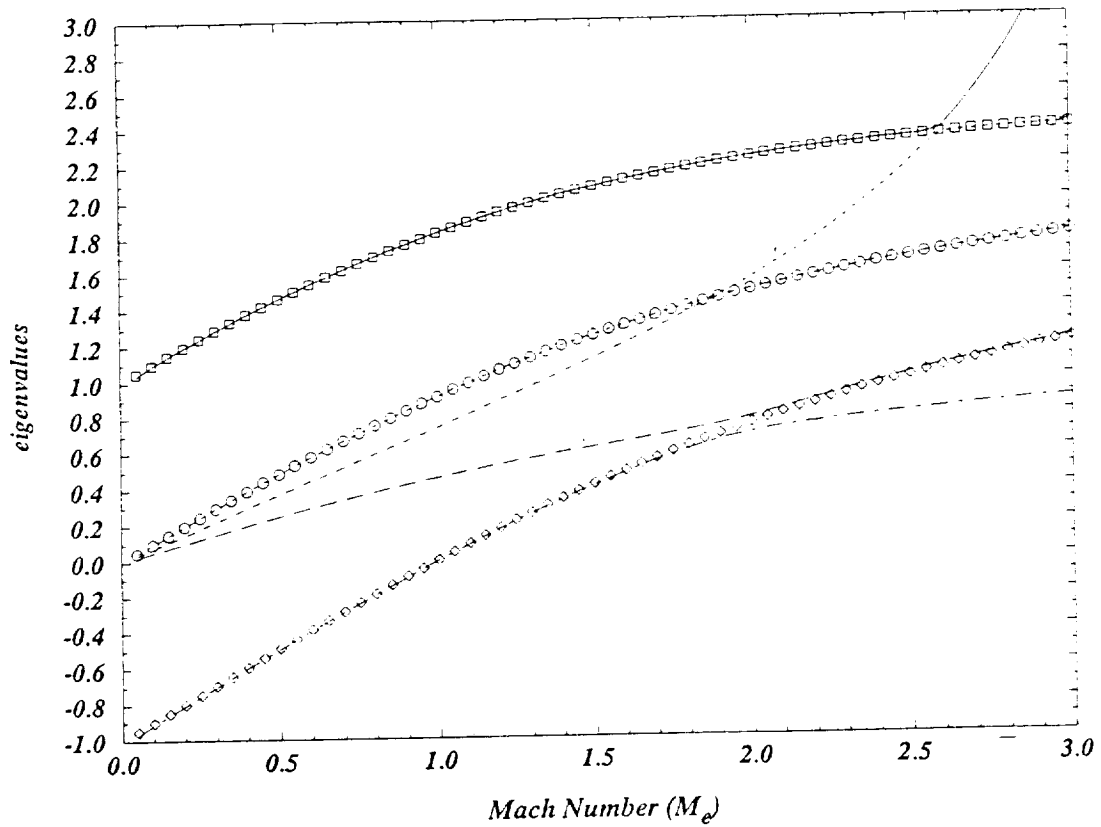
Figure 4. (Continued)

(c). $\bar{H} = 2.0$, $\theta = 0.001$

eigenvalues vs *Mach Number (M_e)*

(d). $\bar{H} = 3.0$, $\theta = 0.001$

complex eigenvalues

eigenvalues vs *Mach Number (M_e)*
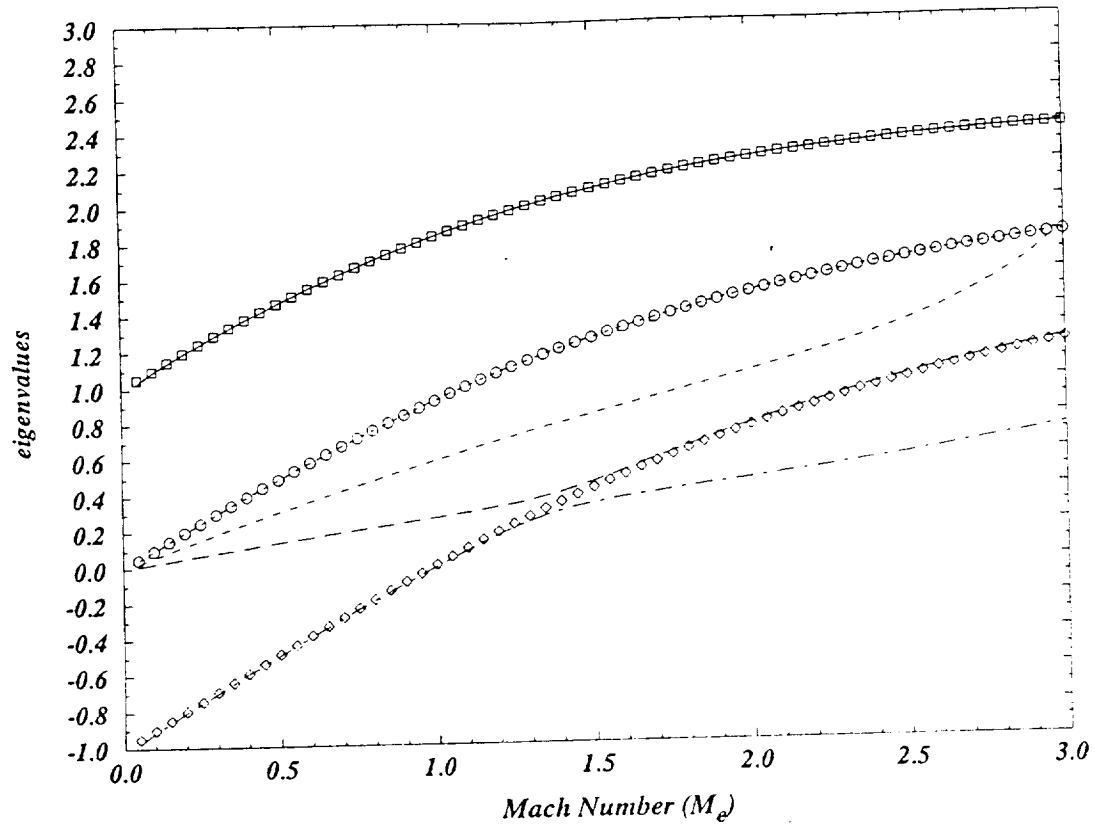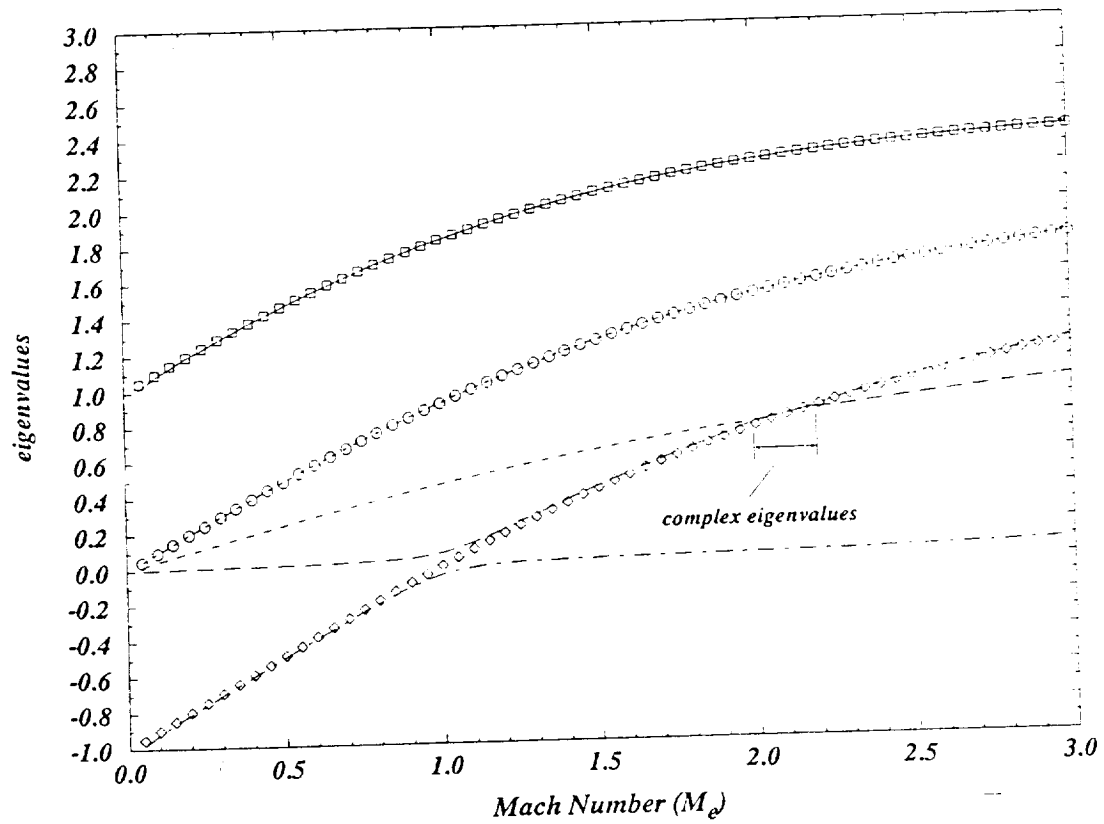
Figure 4. (Continued)

(e). $\bar{H} = 6.0$, $\theta = 0.001$

complex eigenvalues

(f). $\bar{H} = 1.2$, $\theta = 0.01$

53
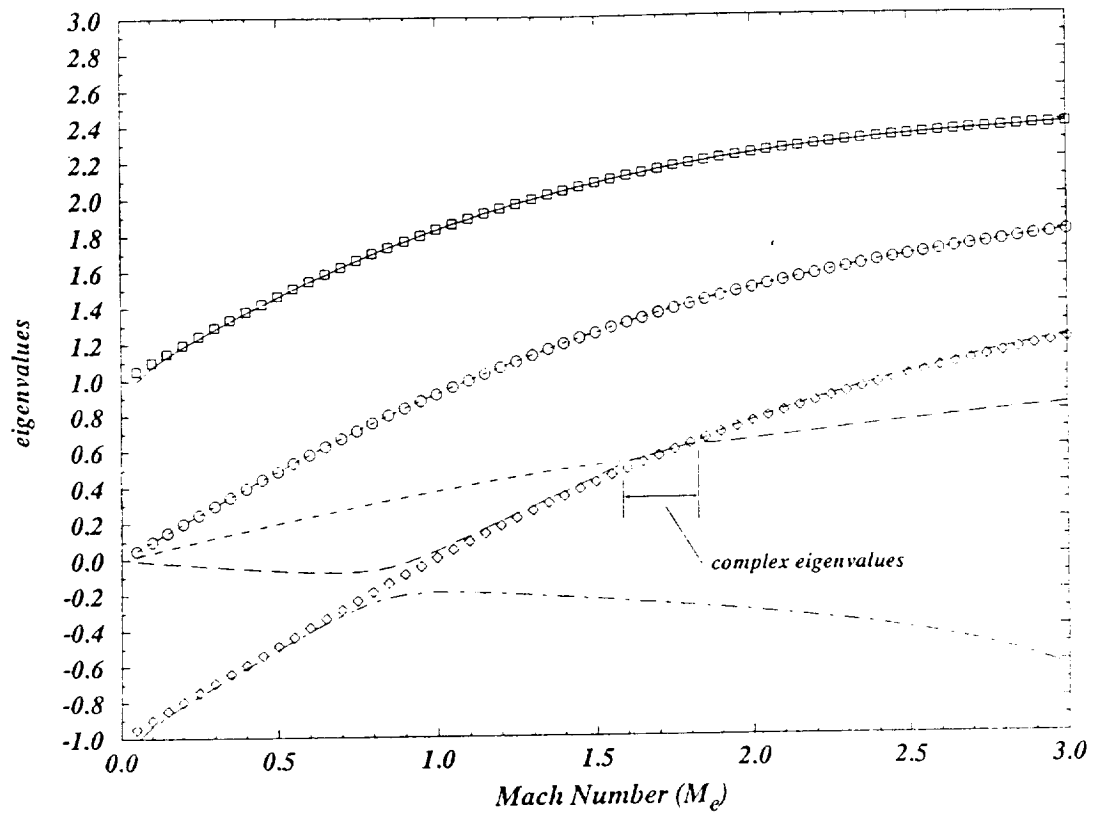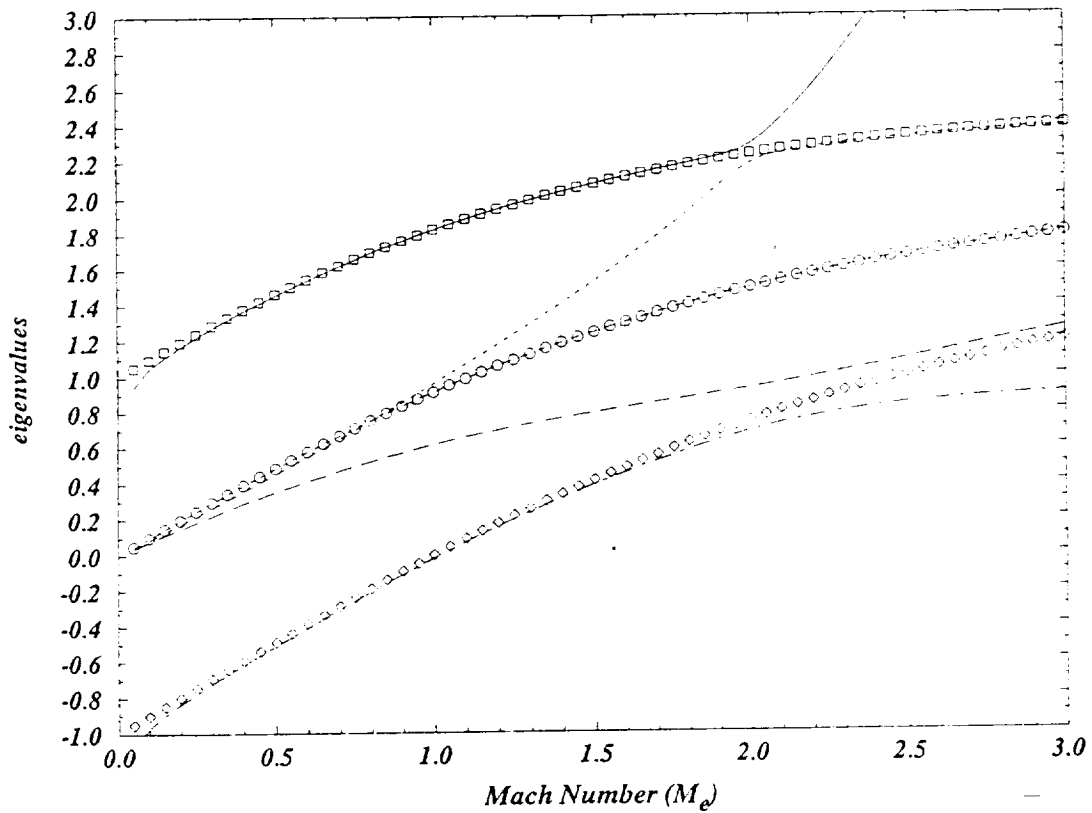
Figure 4. (Continued)

(g). $\bar{H} = 1.5$, $\theta = 0.01$
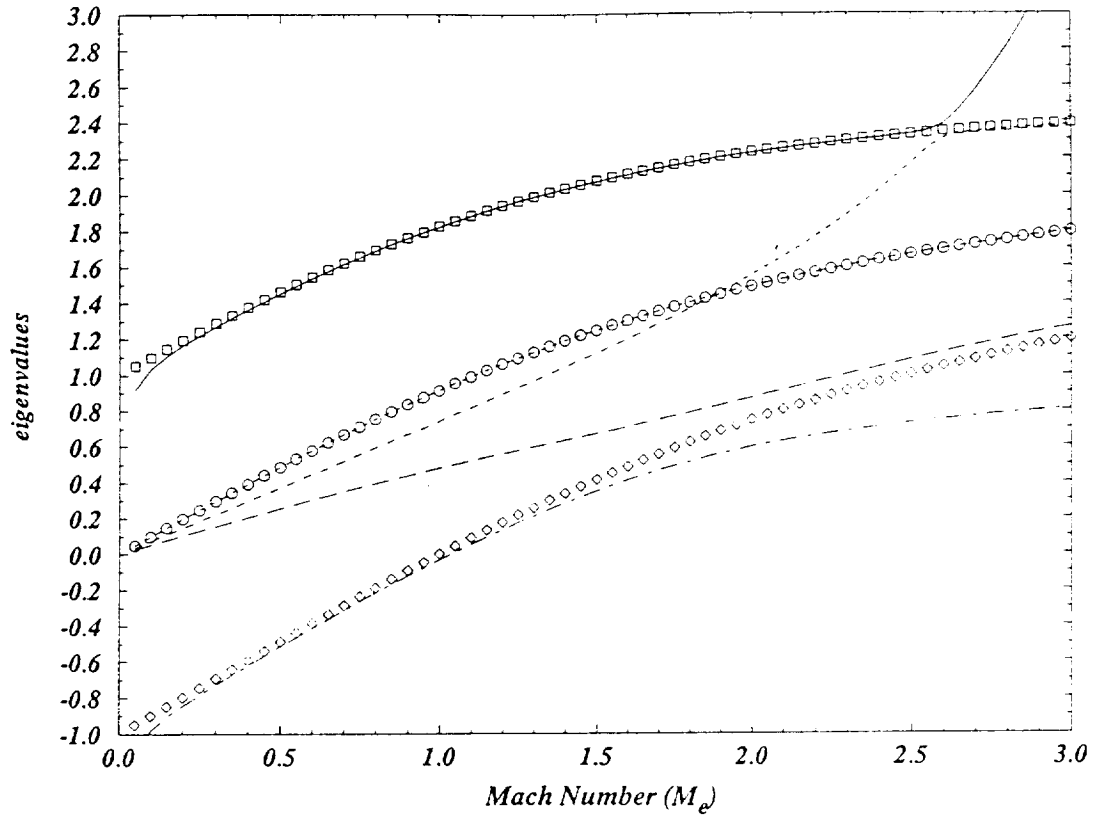
(h). $\bar{H} = 2.0$, $\theta = 0.01$
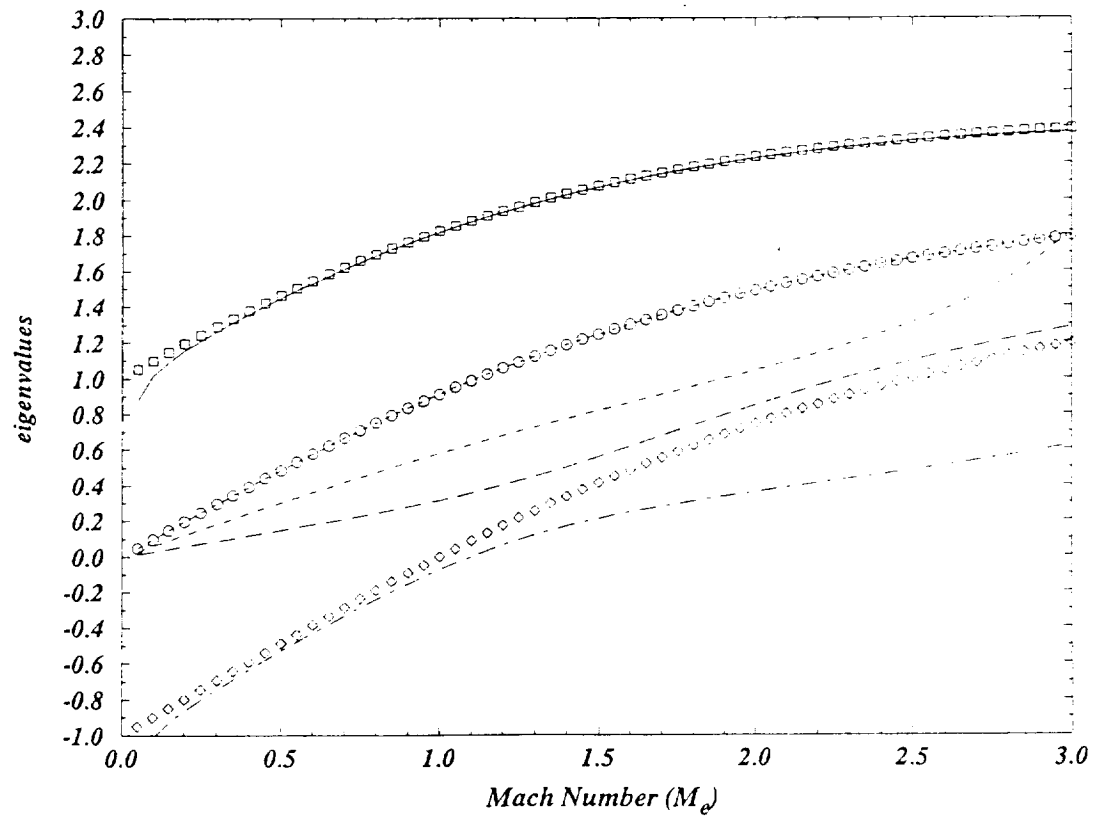
Figure 4. (Continued)

(i). $\bar{H} = 3.0$, $\theta = 0.01$
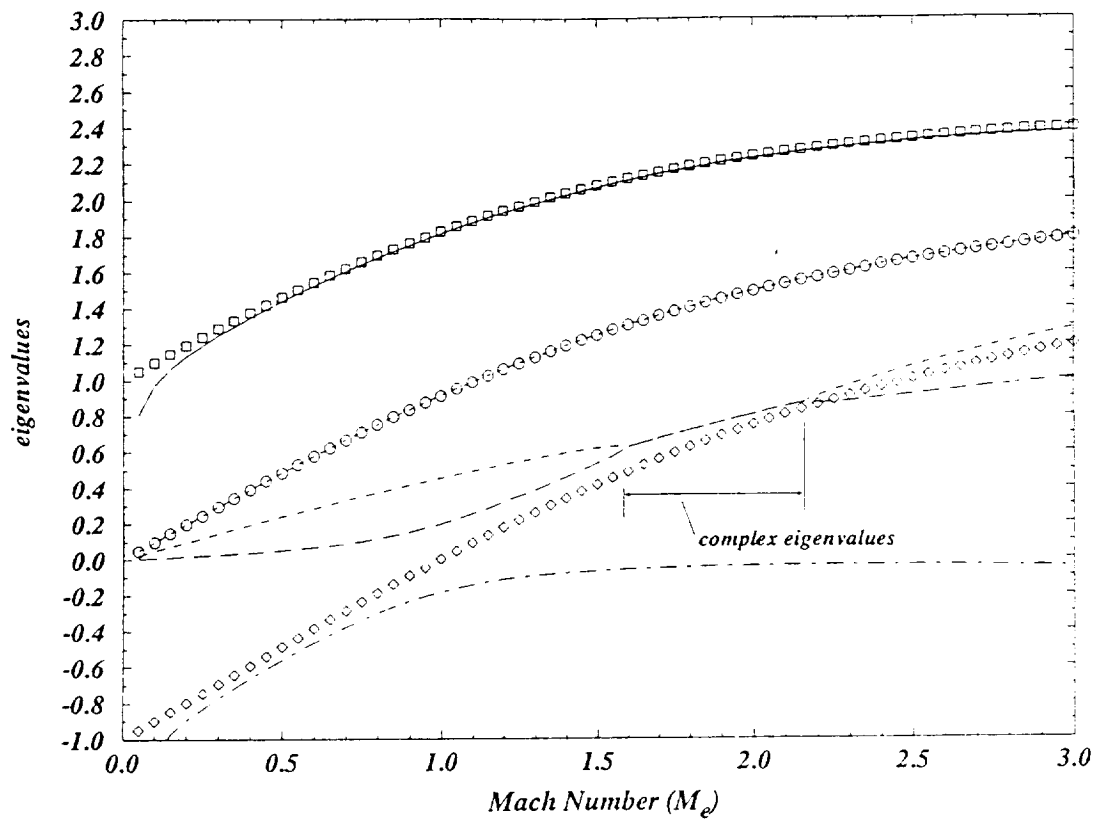
(j). $\bar{H} = 6.0$, $\theta = 0.01$
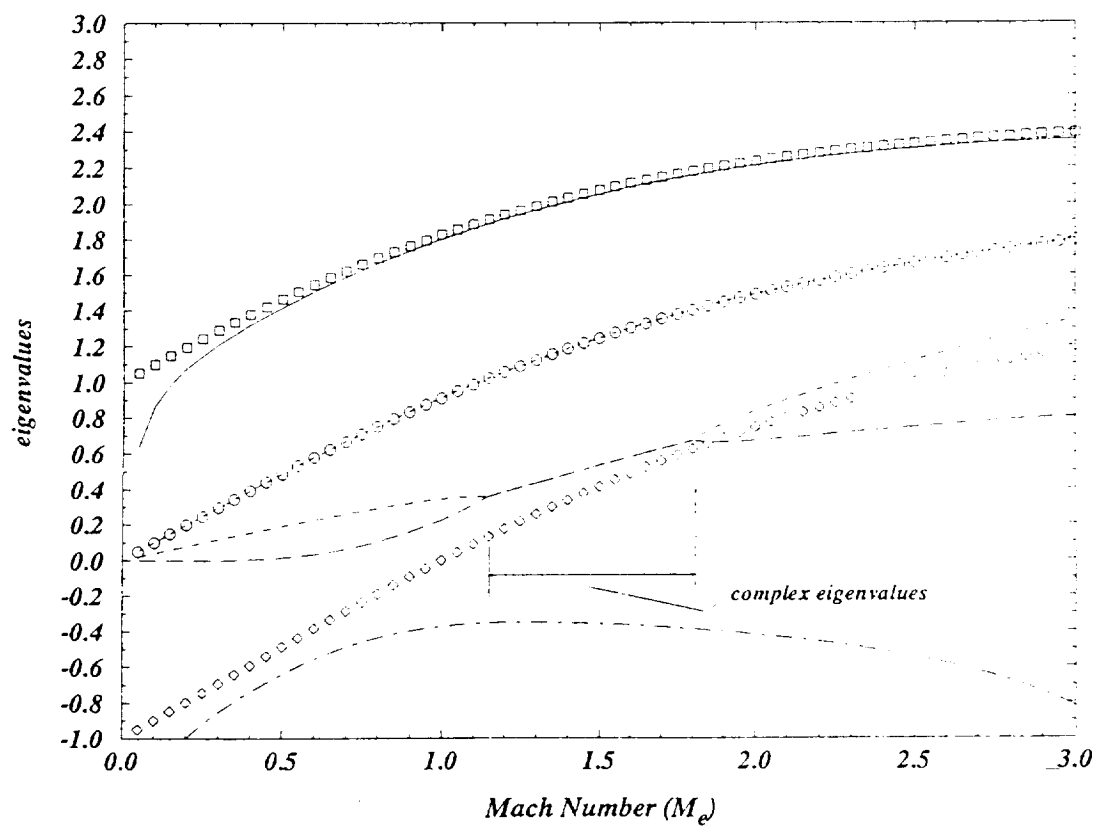
Figure 4. (Continued)

(k). $\bar{H} = 1.2$, $\theta = 0.1$
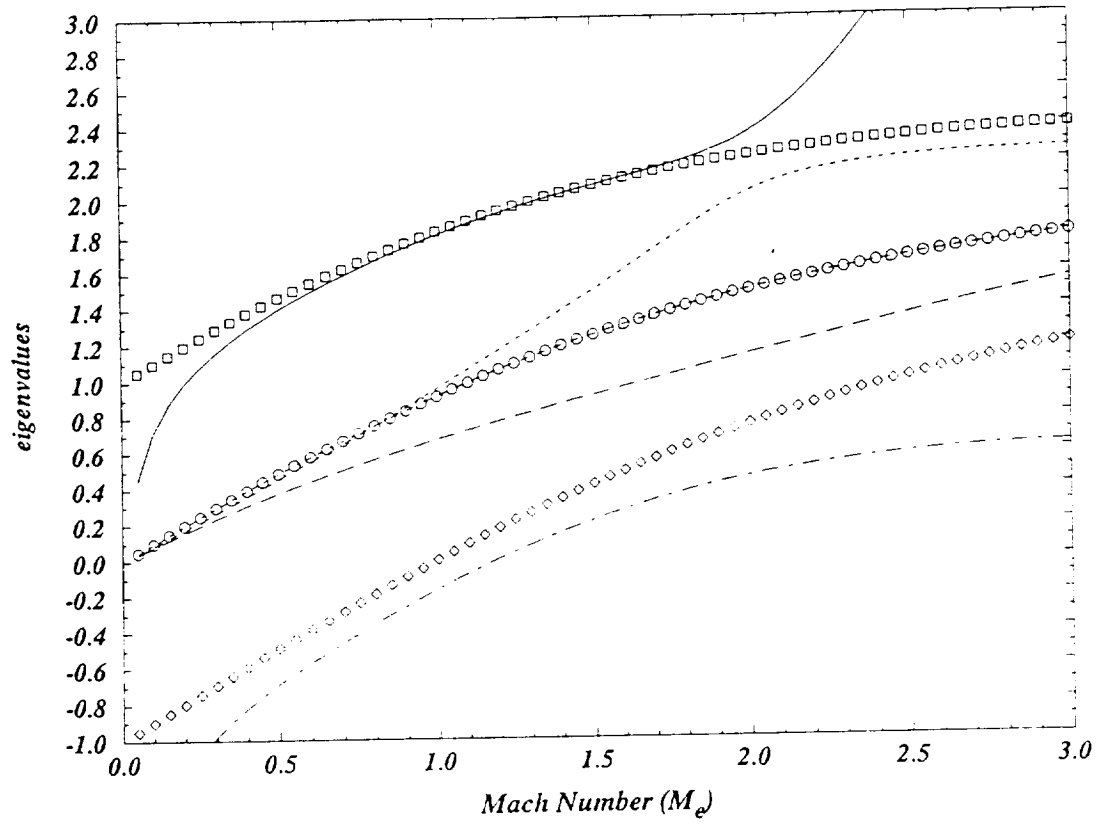
(l). $\bar{H} = 1.5$, $\theta = 0.1$
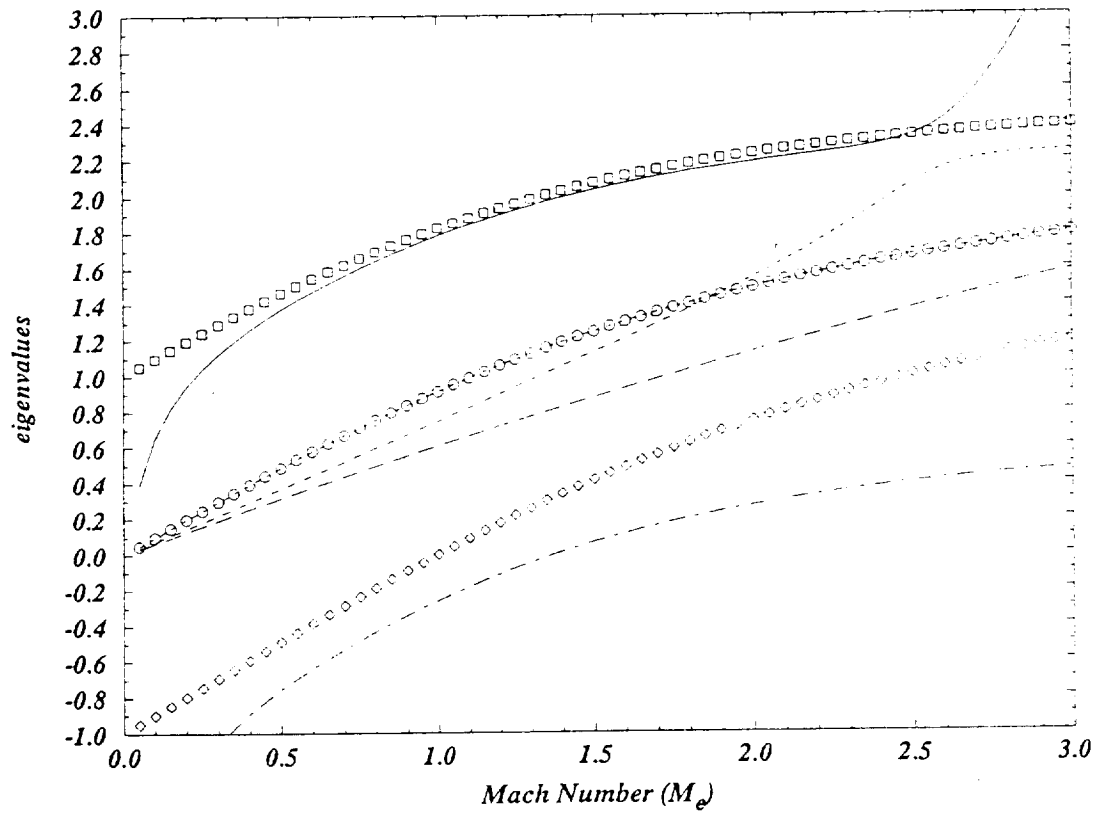
Figure 4. (Continued)

(m). $\bar{H} = 2.0$, $\theta = 0.1$
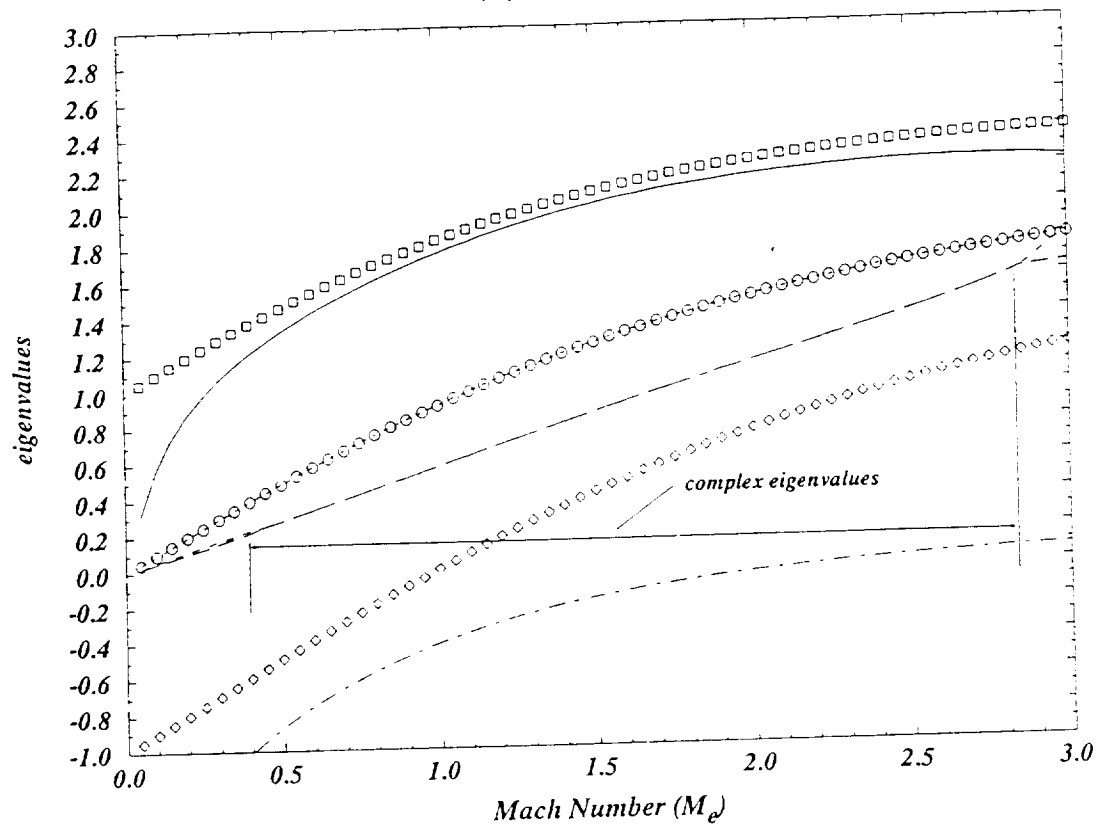
(n). $\bar{H} = 3.0$, $\theta = 0.1$
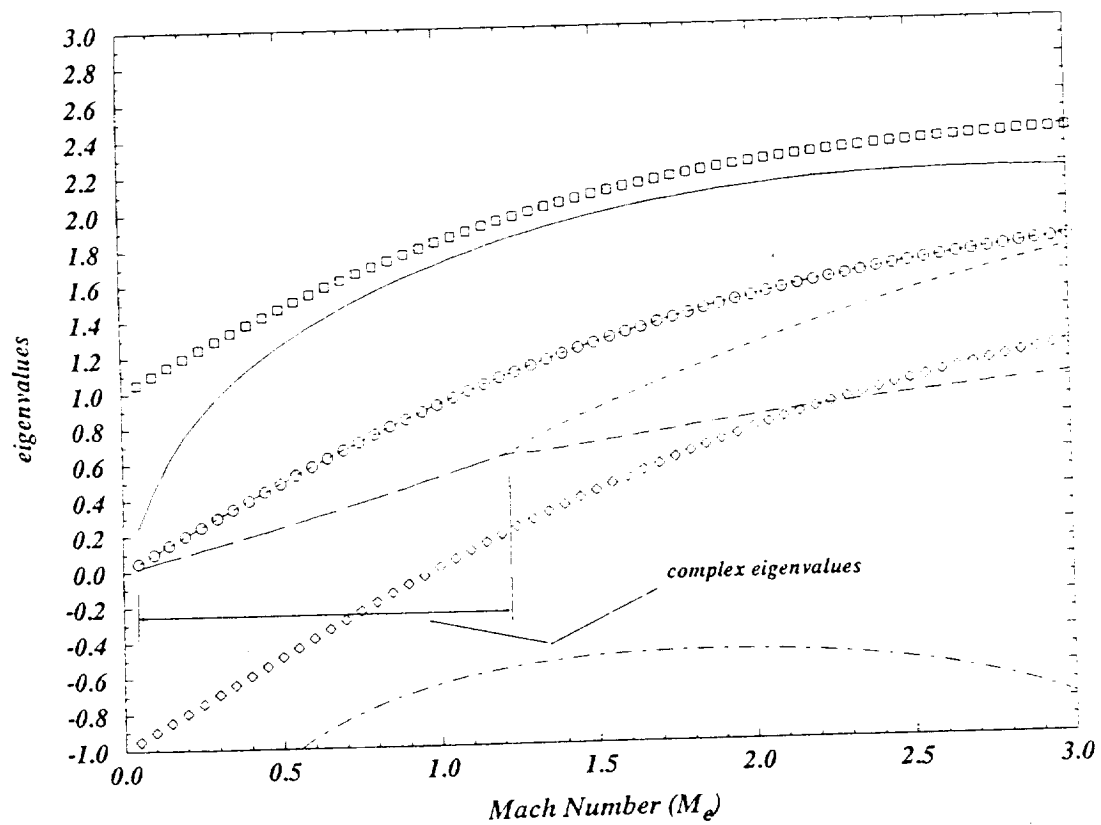
Figure 4. (Continued)

(o). $\overline{H} = 6.0$, $\theta = 0.1$
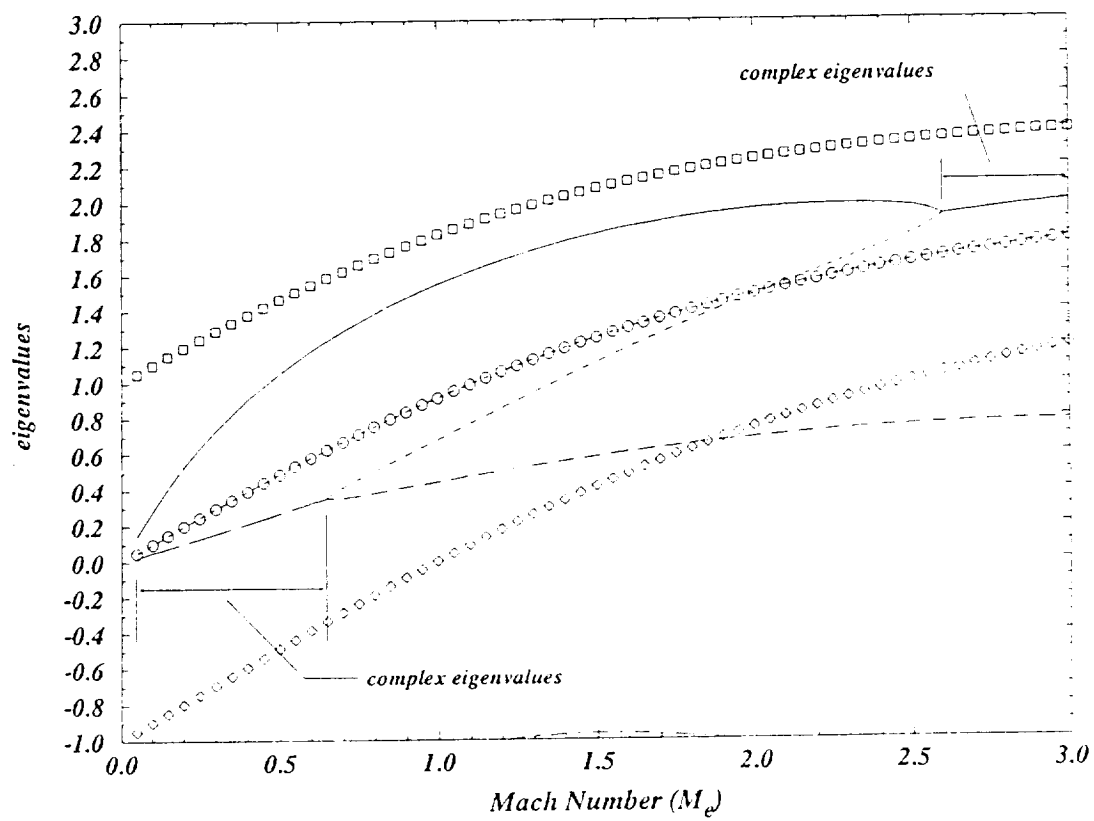
Figure 5. Measured and Computed Subsonic Diffuser Parameters
(Thinner Inlet Boundary Layer)

(a). Wall Static Pressure

(b). Incompressible Displacement Thickness
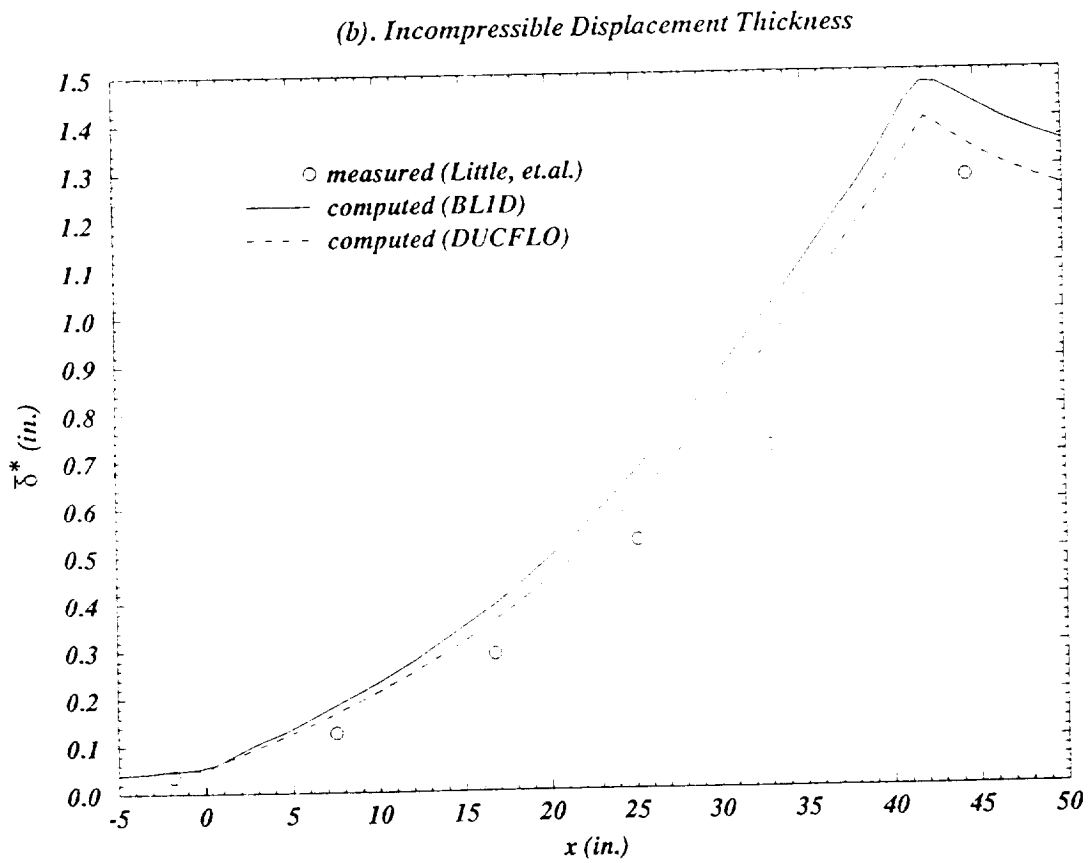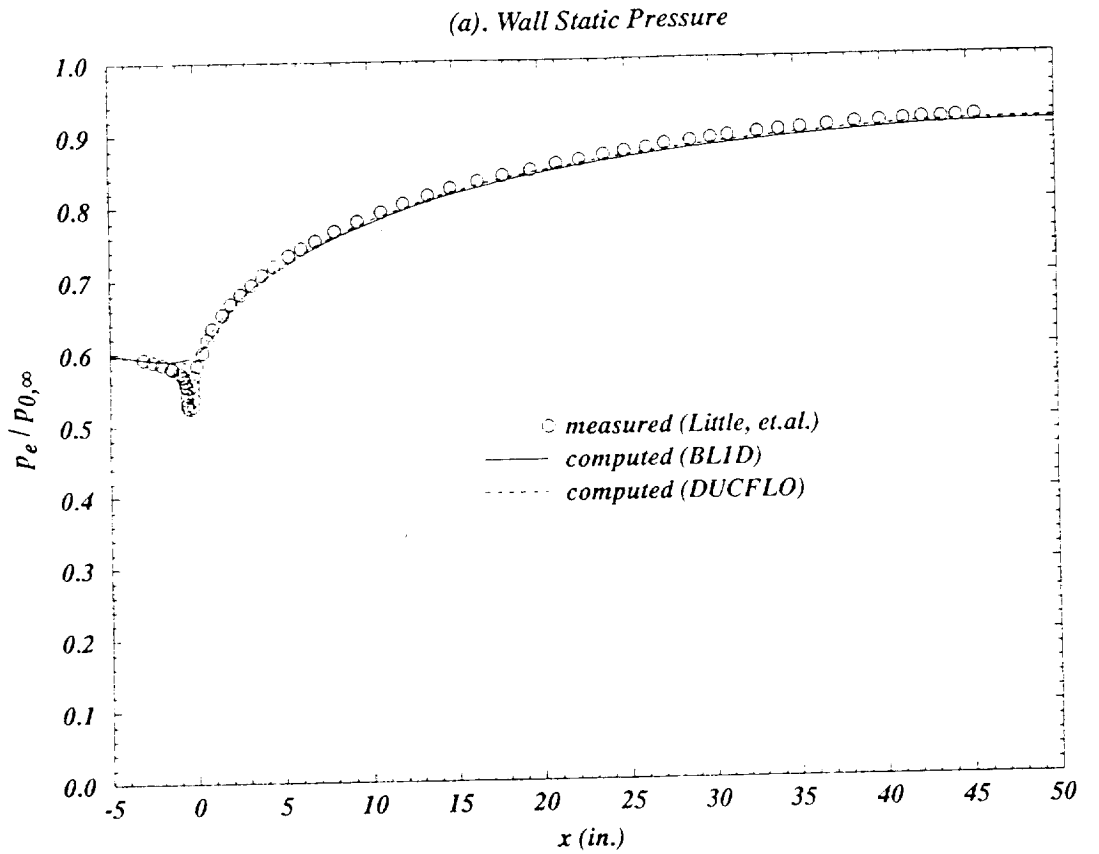
Figure 5. (Continued)

(c). Incompressible Momentum Thickness

(d). Incompressible Shape Factor

60
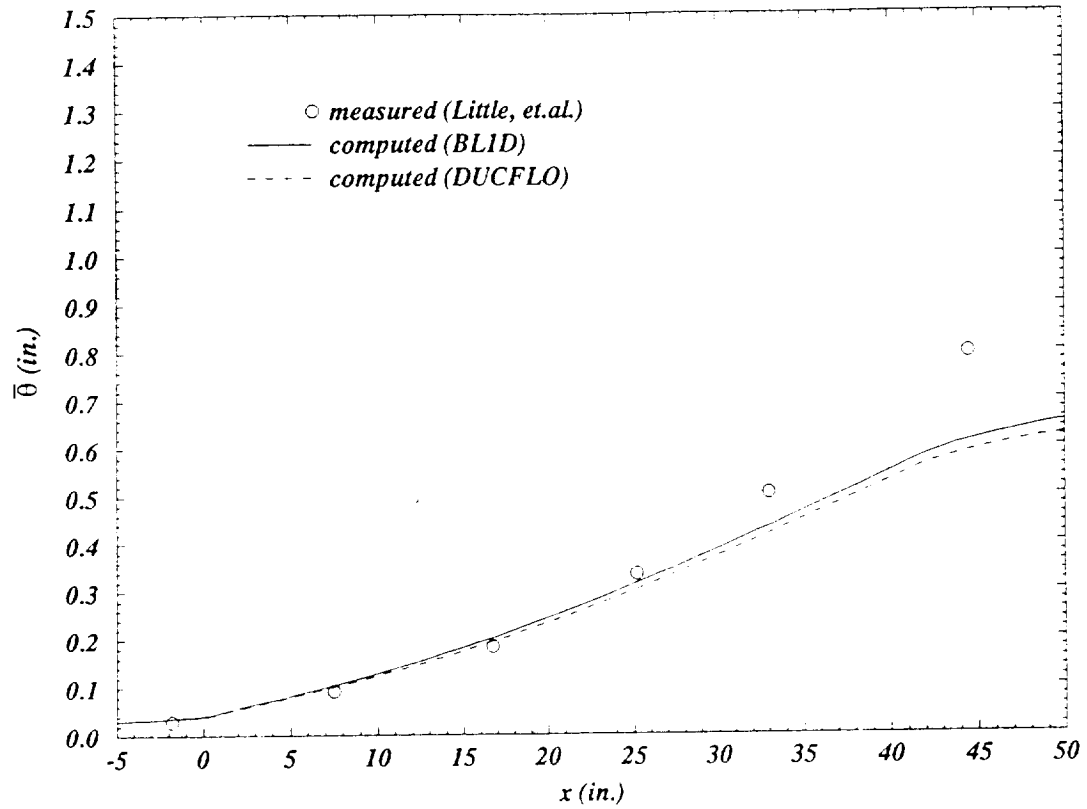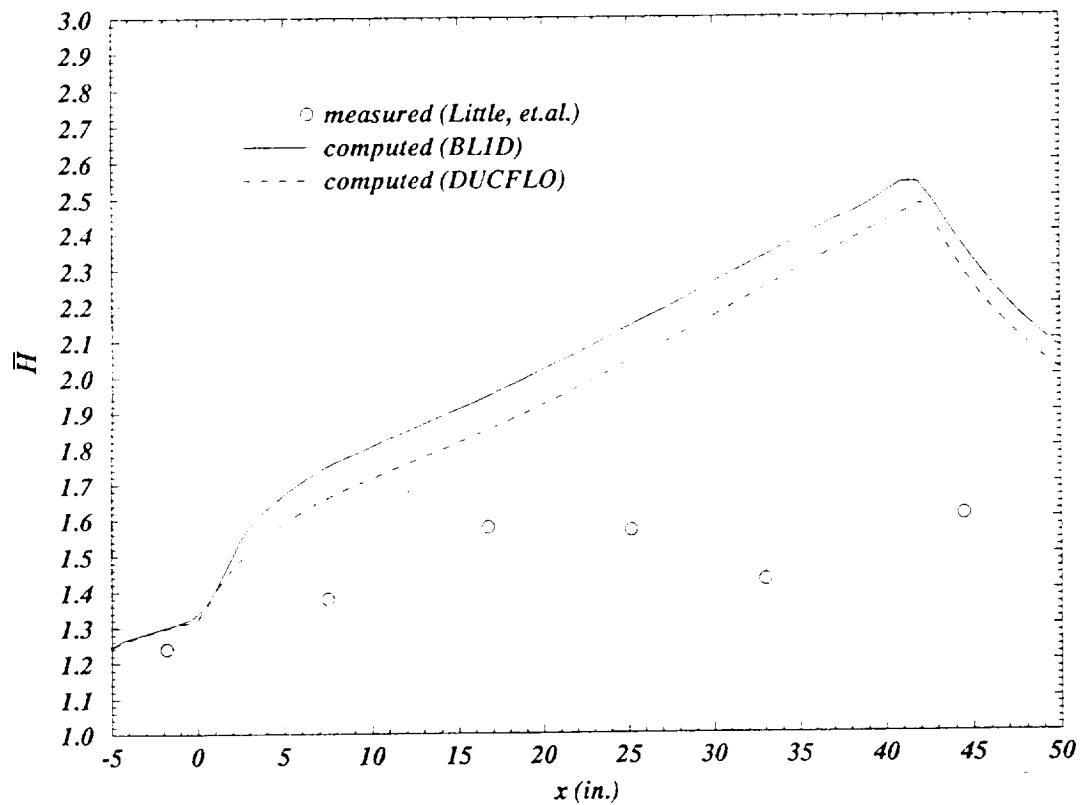
Figure 5. (Continued)

(e). Skin Friction
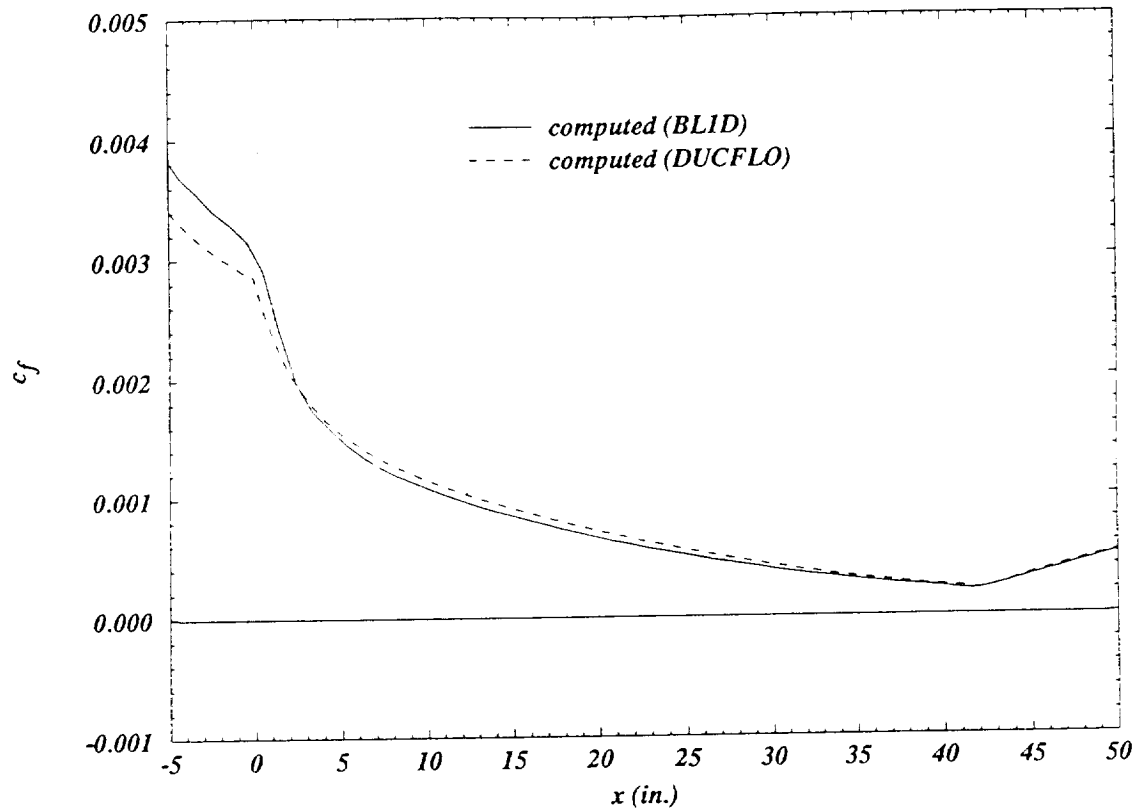
(f). Exit Velocity Profiles
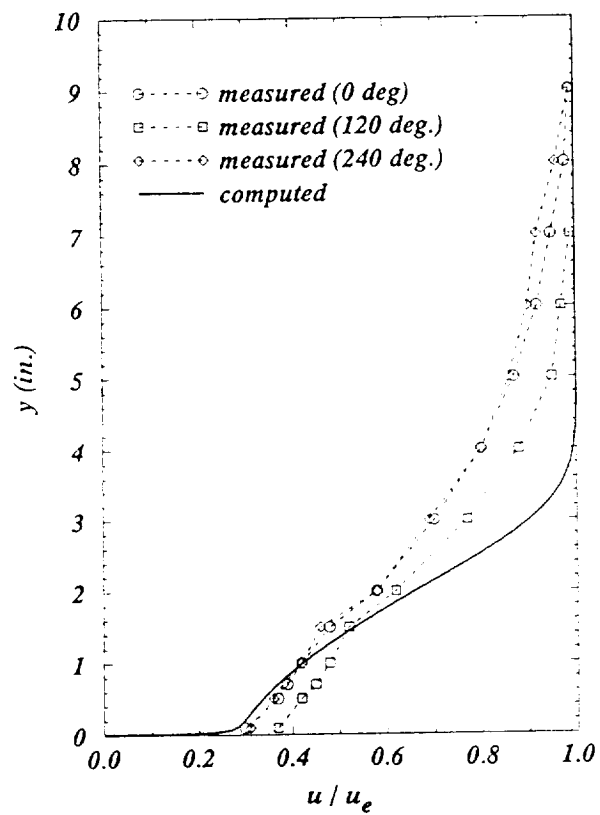
Figure 6. Measured and Computed Subsonic Diffuser Parameters
(Thicker Inlet Boundary Layer)

(a). Wall Static Pressure
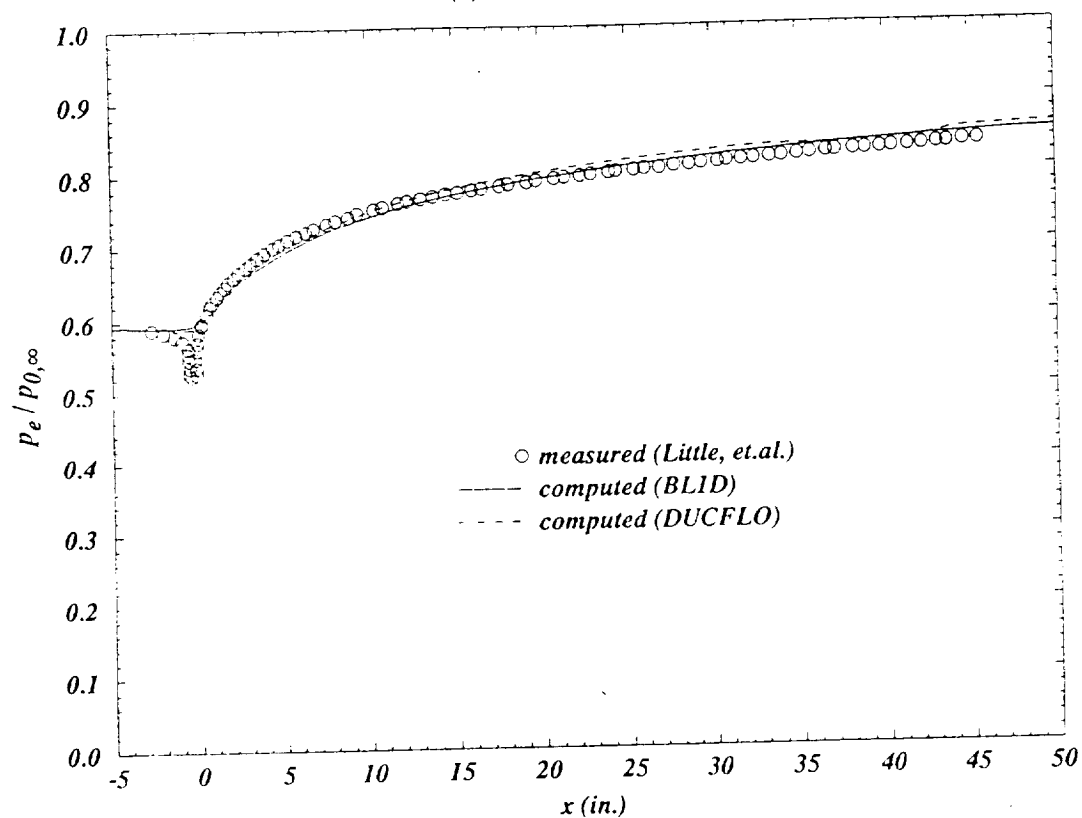
(b). Incompressible Displacement Thickness
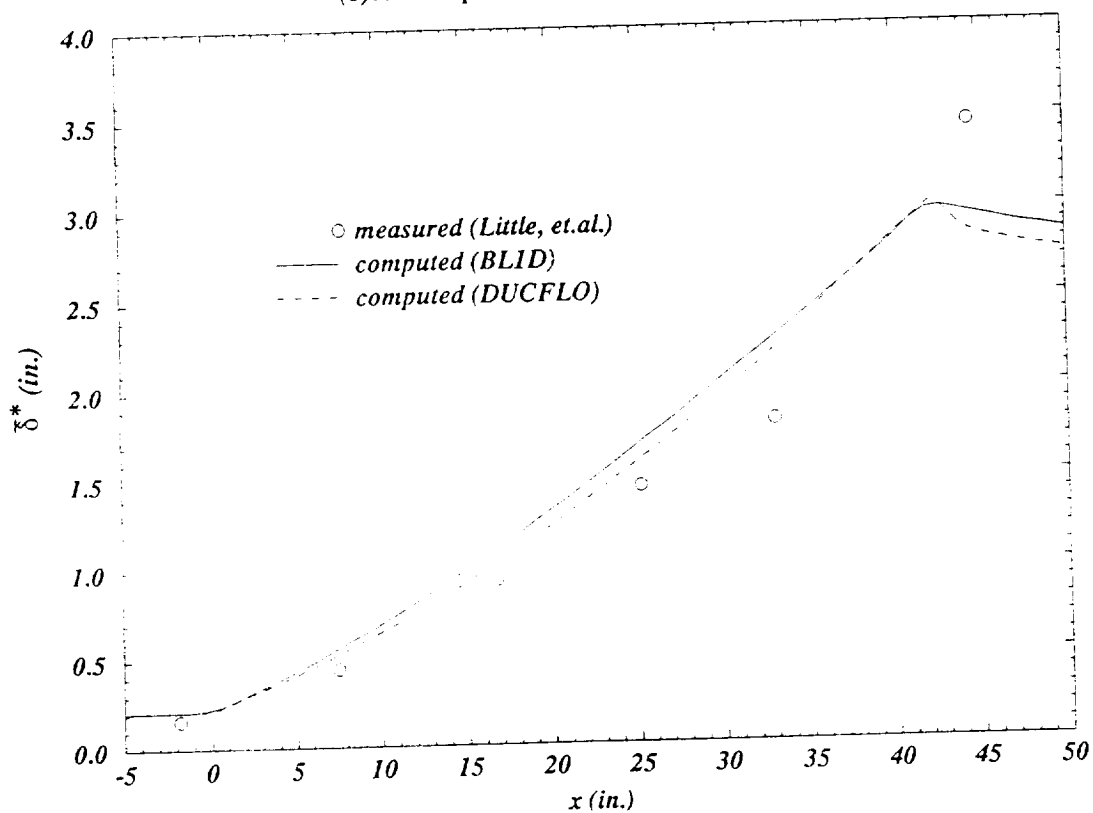
Figure 6. (Continued)

(c). Incompressible Momentum Thickness
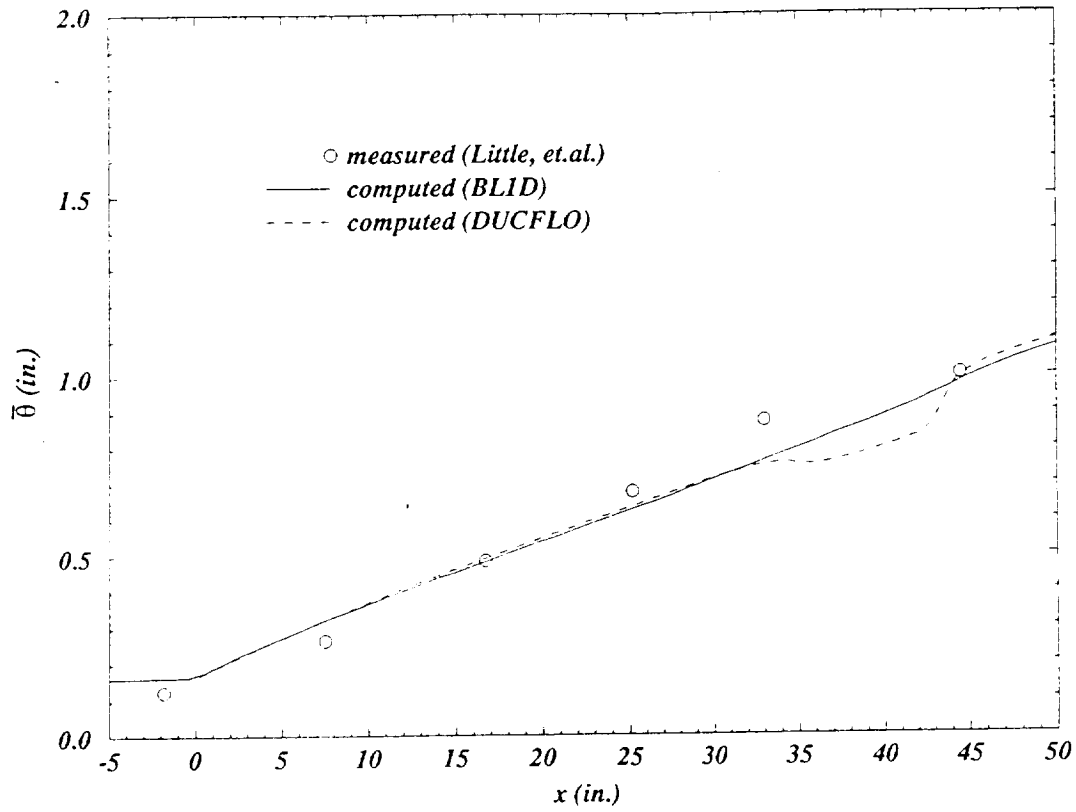
(d). Incompressible Shape Factor
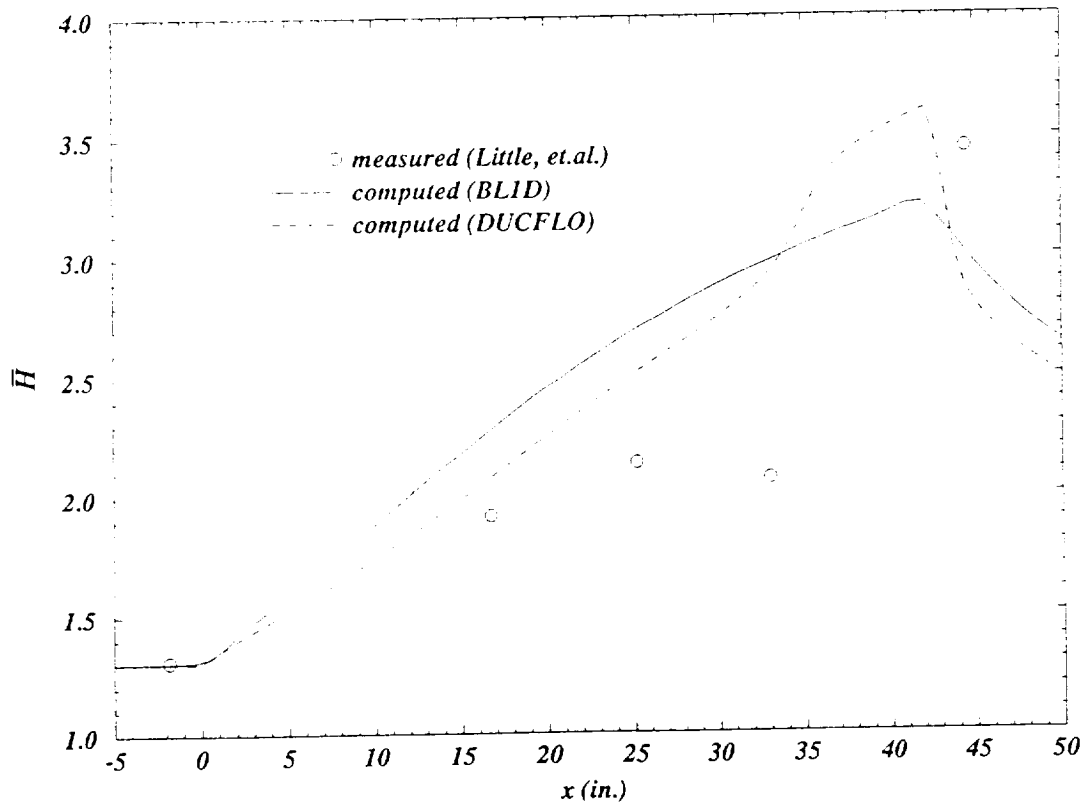
Figure 6. (Continued)

(e). Skin Friction
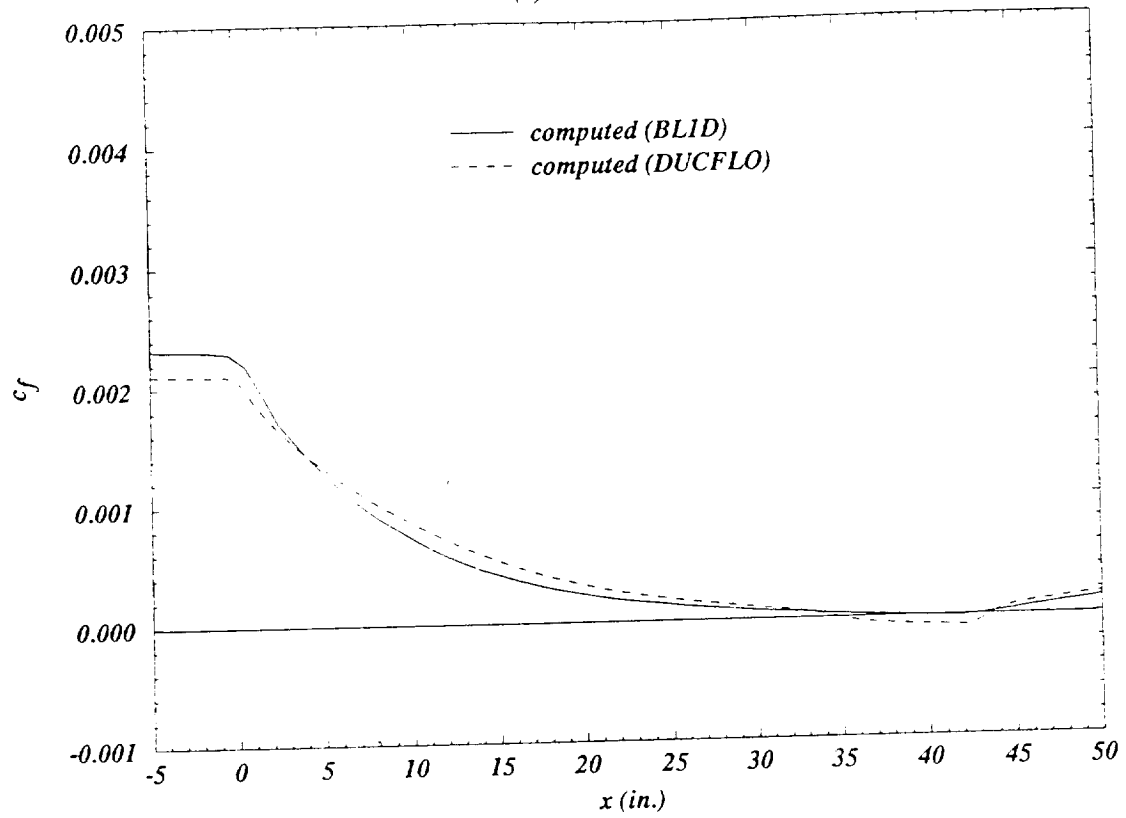
(f). Exit Velocity Profiles
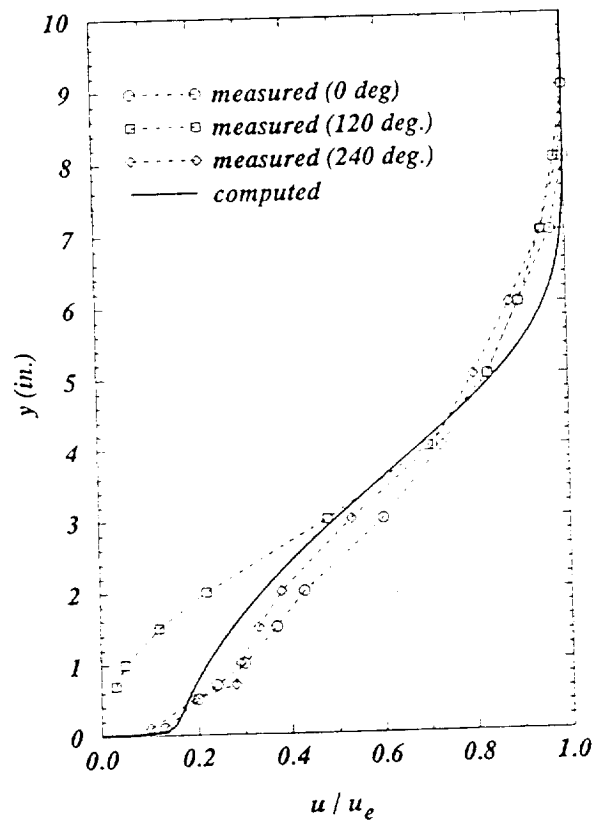
Figure 7. AGARD Geometry

(a). Test Apparatus
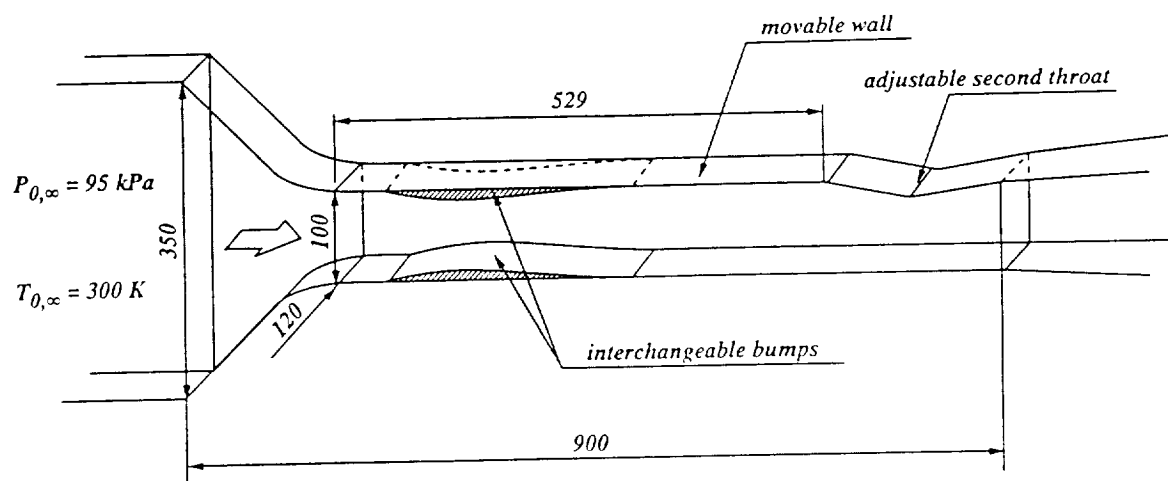
Note: All dimensions in mm

(b). Computational Grid and Boundary Conditions
(Navier-Stokes Simulation–Steady)
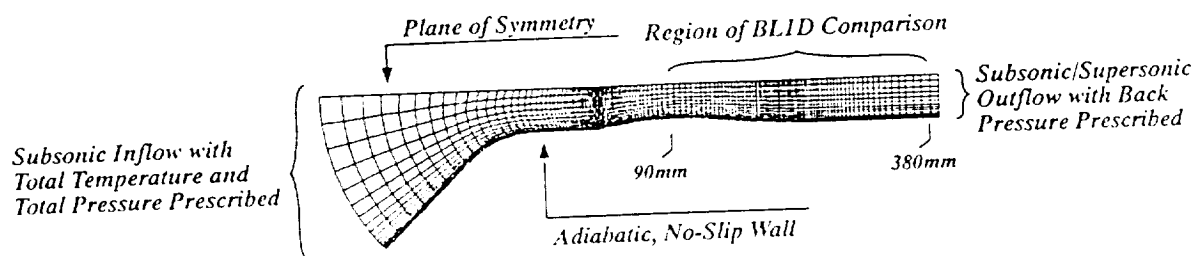
Figure 8. Navier-Stokes and BL1D Comparisons (Steady Case)

(a). Mach Number

(b). Density
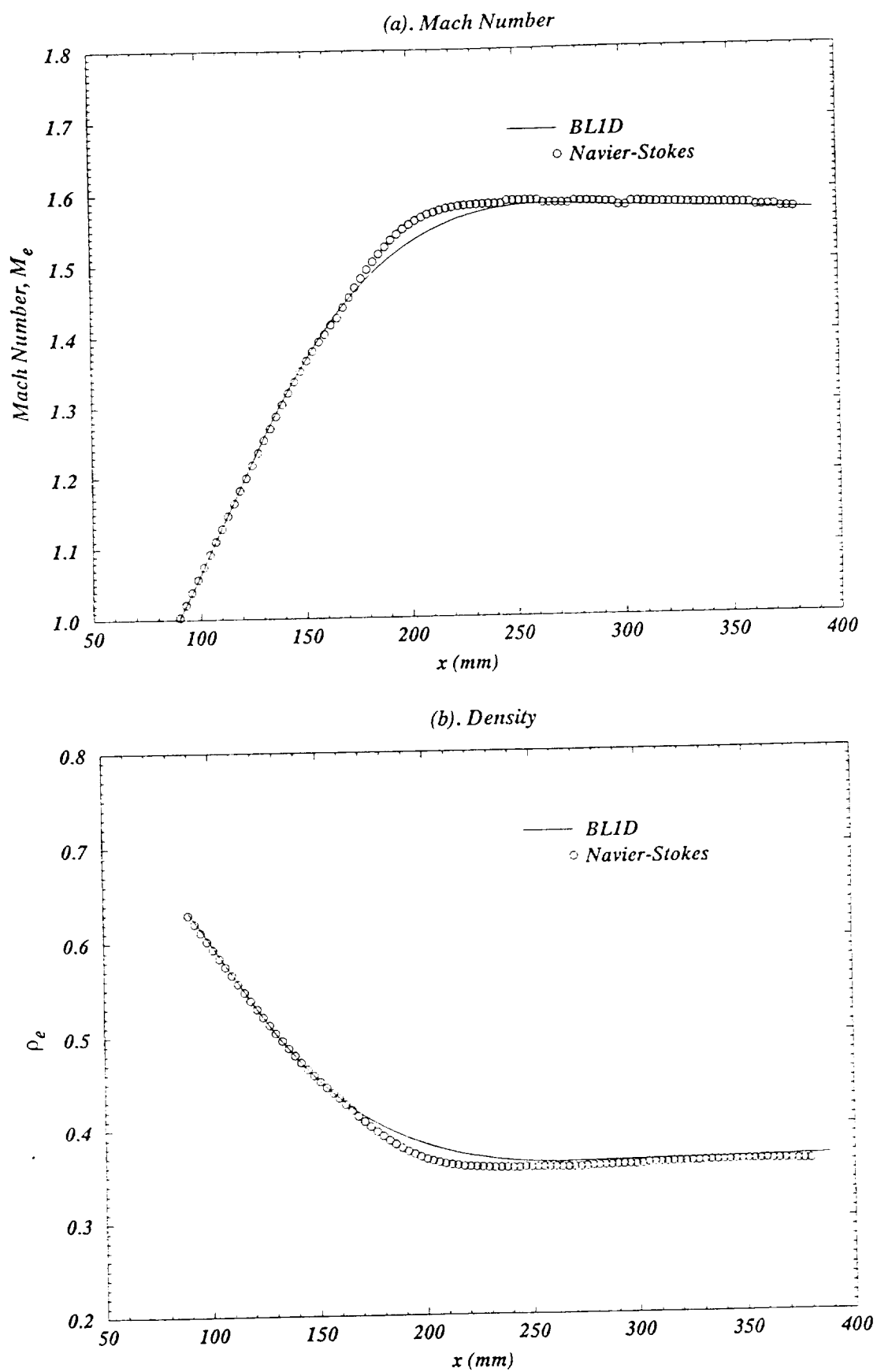
Figure 8. (Continued)

(c). Momentum Thickness
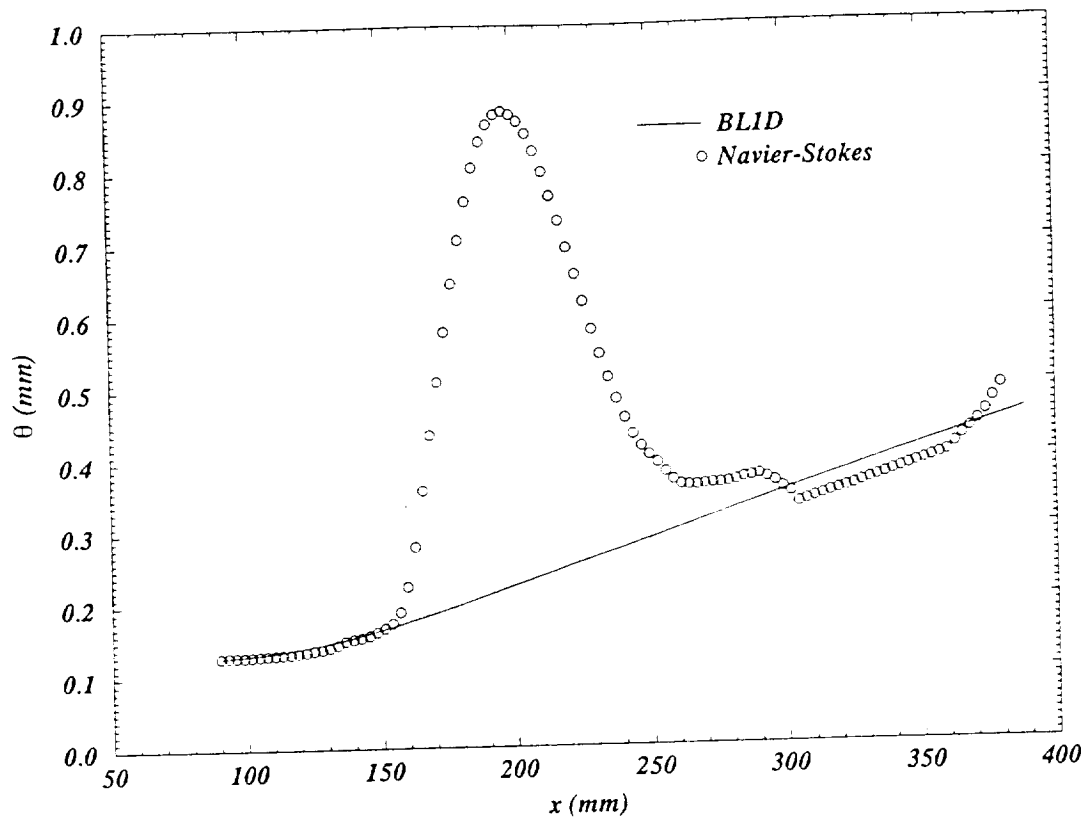
(d). Shape Factor
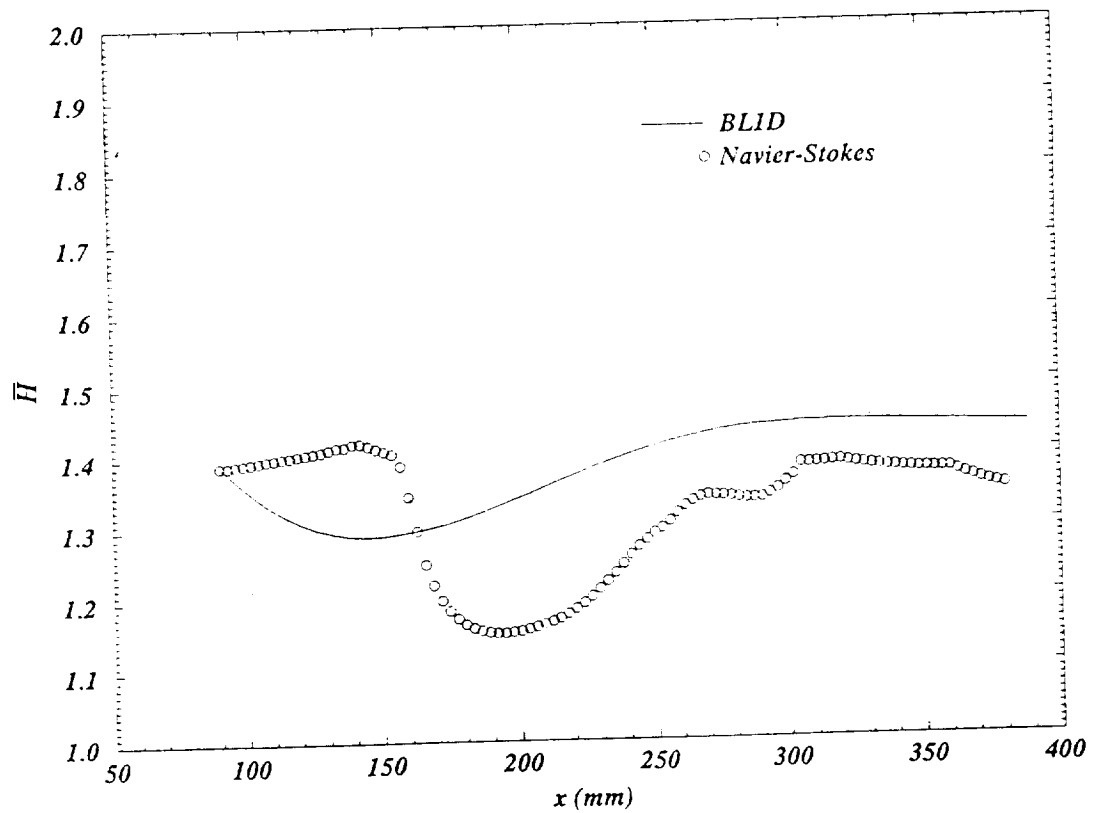
Figure 8. (Continued)

(e). Velocity Profiles in Nozzle Region
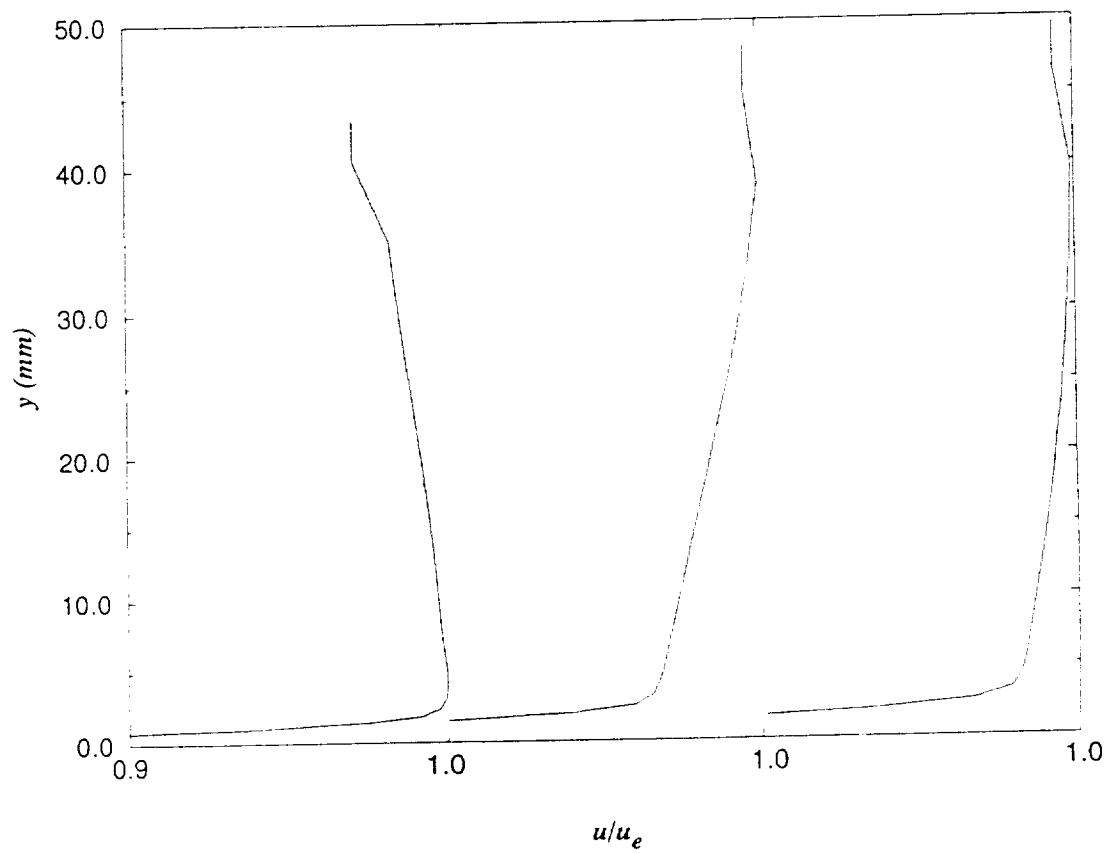
Figure 9. Computational Grid and Boundary Conditions for Modified AGARD Geometry (Navier-Stokes—Unsteady)

Plane of Symmetry

Region of BLID Comparison

300mm

750mm

Adiabatic, No-Slip Wall

Subsonic/Supersonic Outflow with Back Pressure Prescribed

Subsonic Inflow with Total Temperature and Total Pressure Prescribed

69
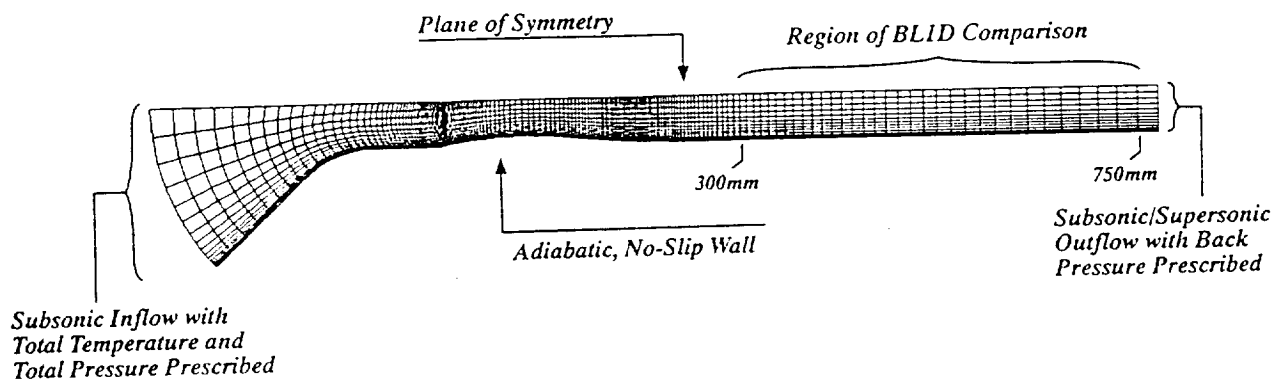
Figure 10. Time Variance of Navier-Stokes Parameters

(a). Reservoir Stagnation Pressure
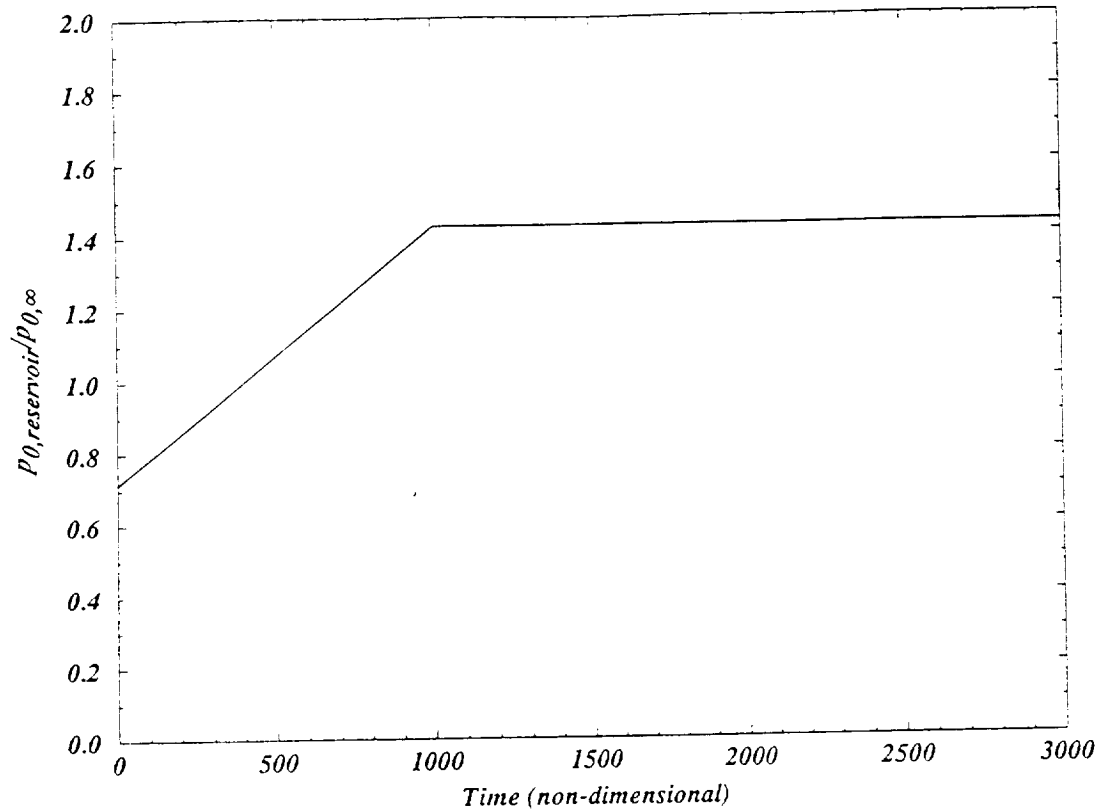
(b). Inviscid Core and Boundary Layer–Parameters at x=300mm
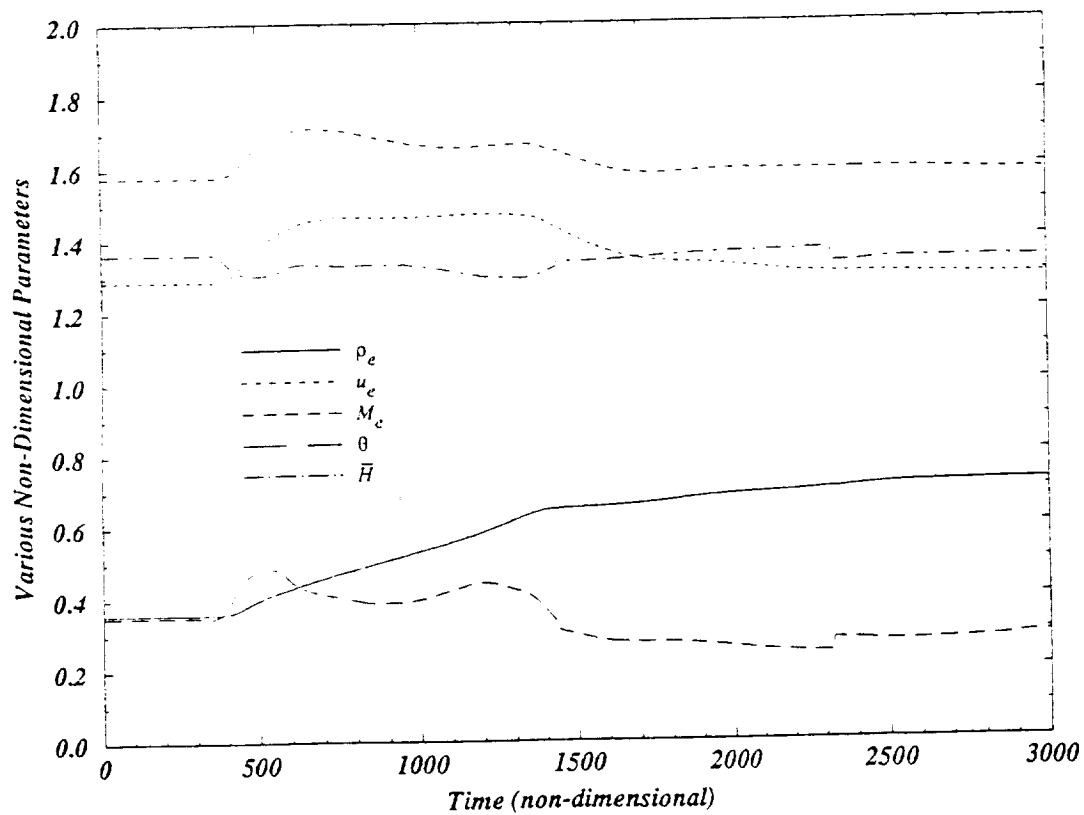
Figure 11. Navier-Stokes and BL1D Channel Parameters at $t \cong 500$
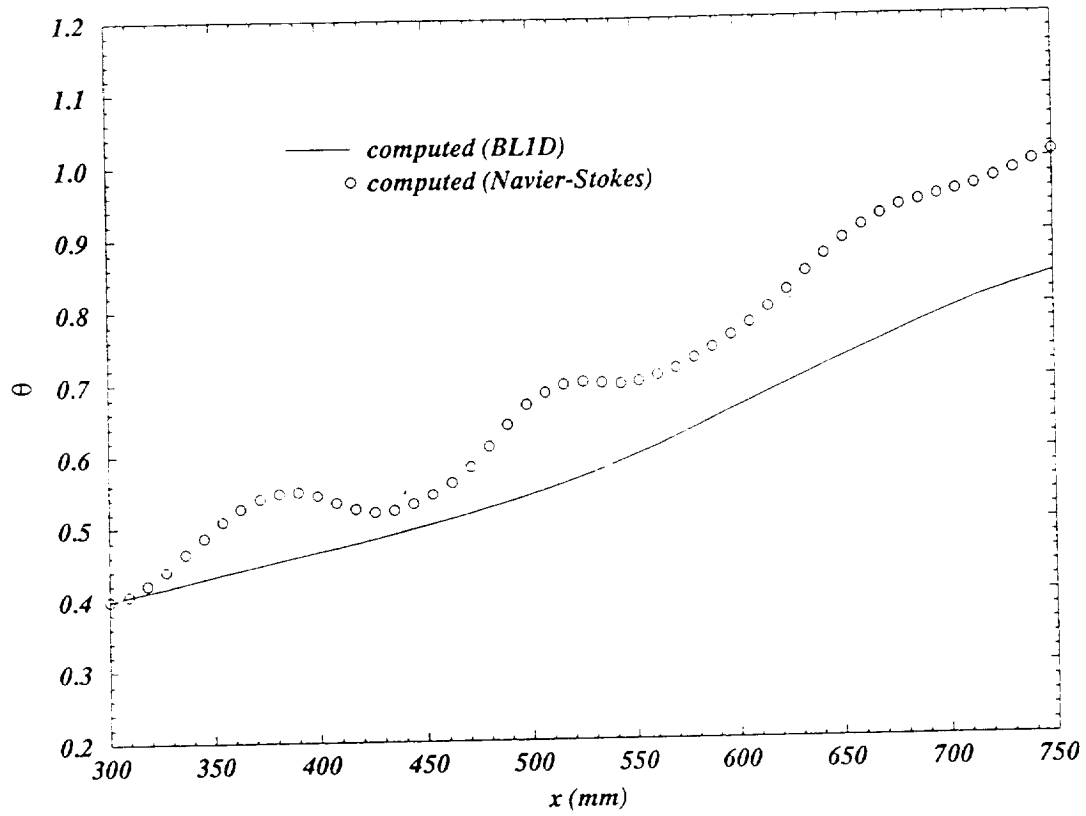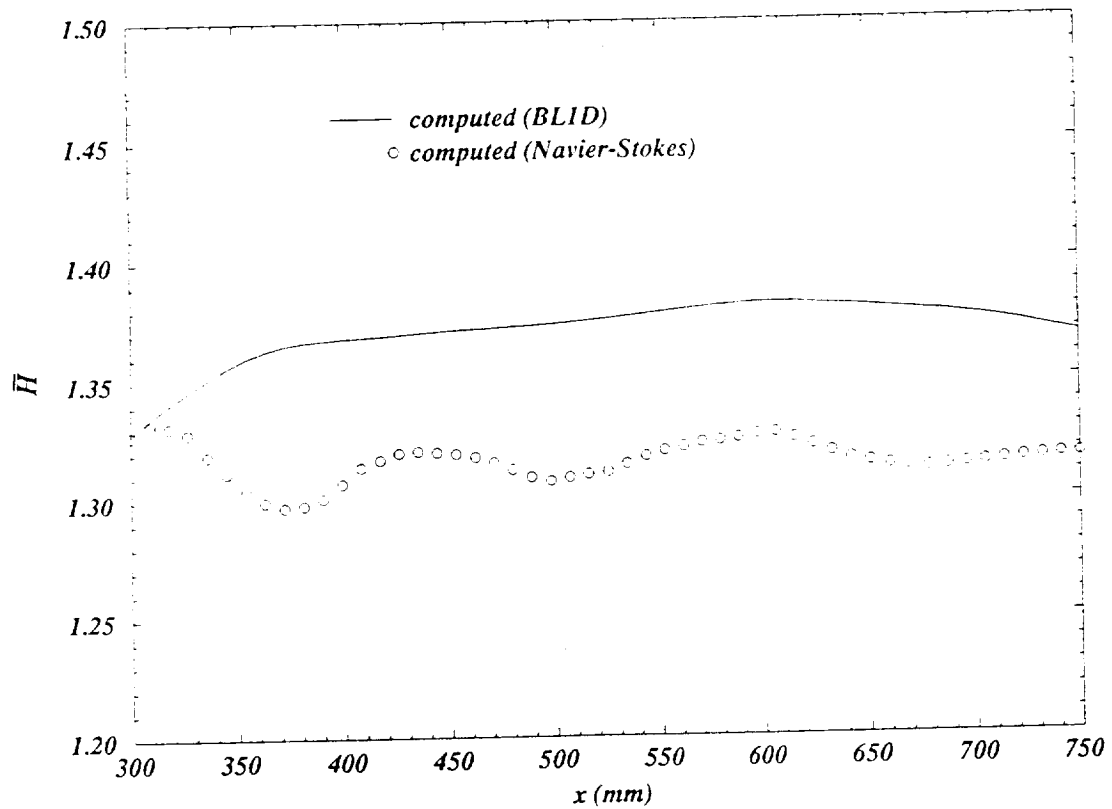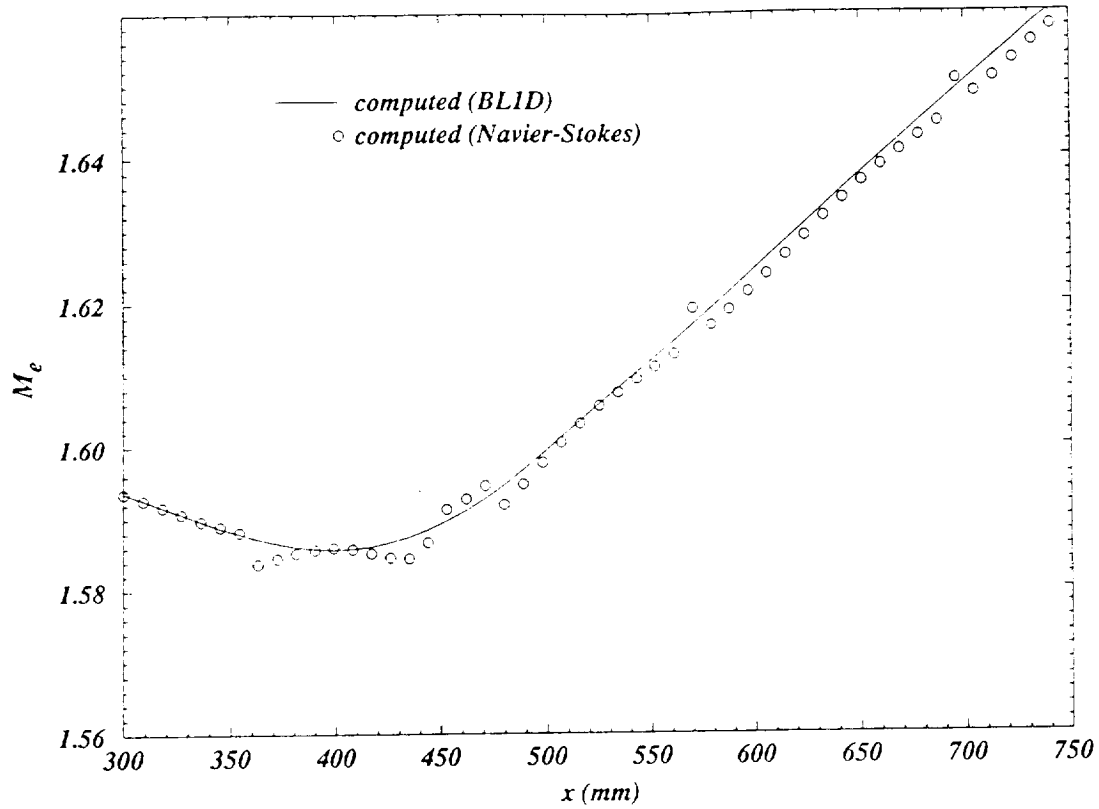
(a). Mach Number
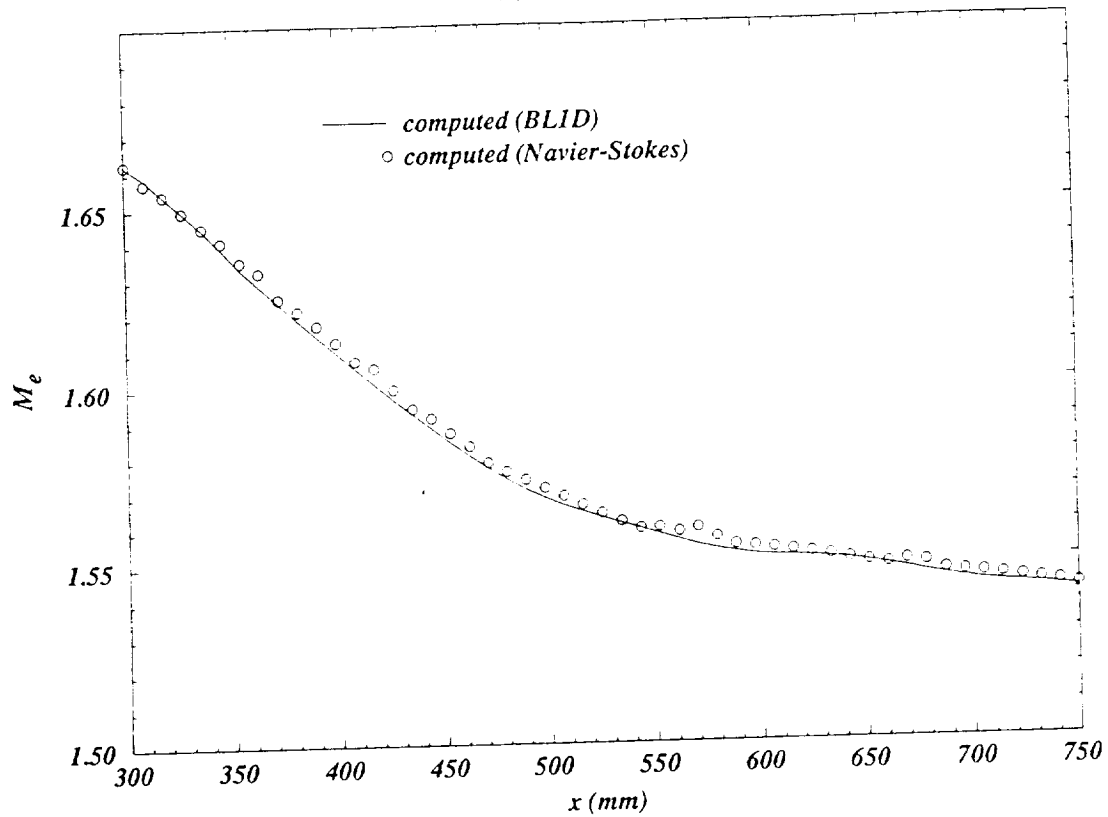
(b). Density
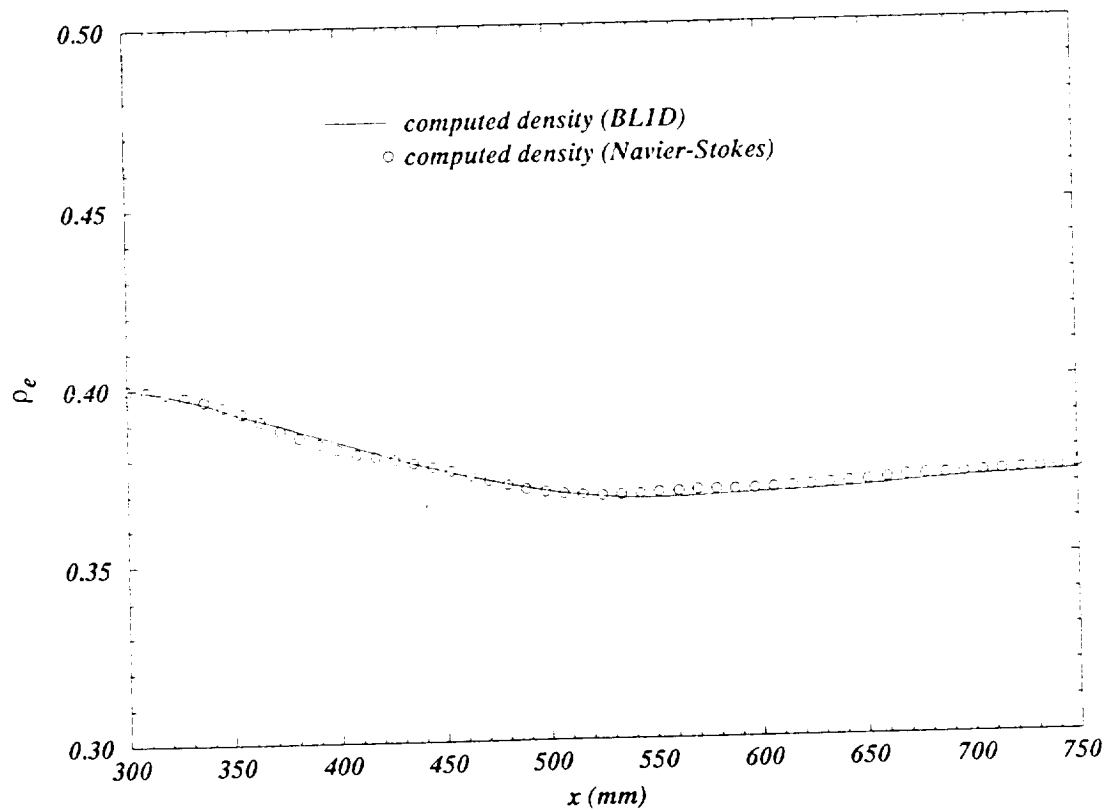
Figure 11. (Continued)

(c). Momentum Thickness
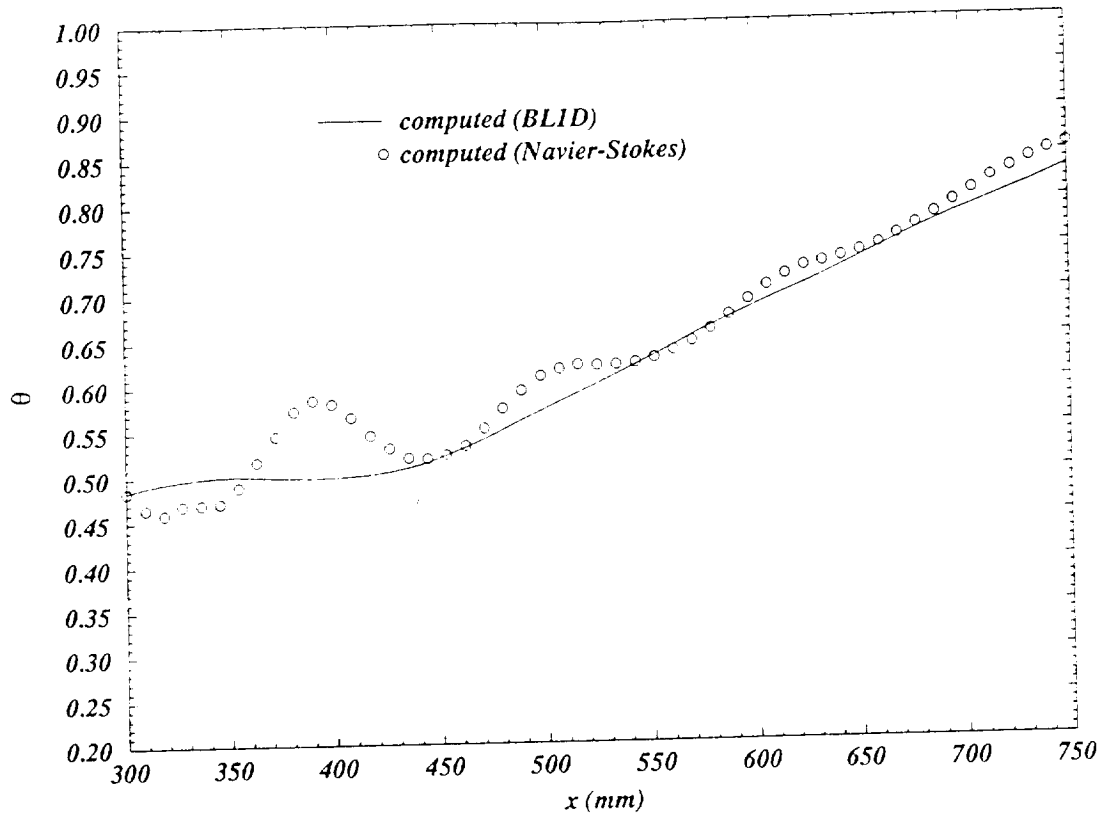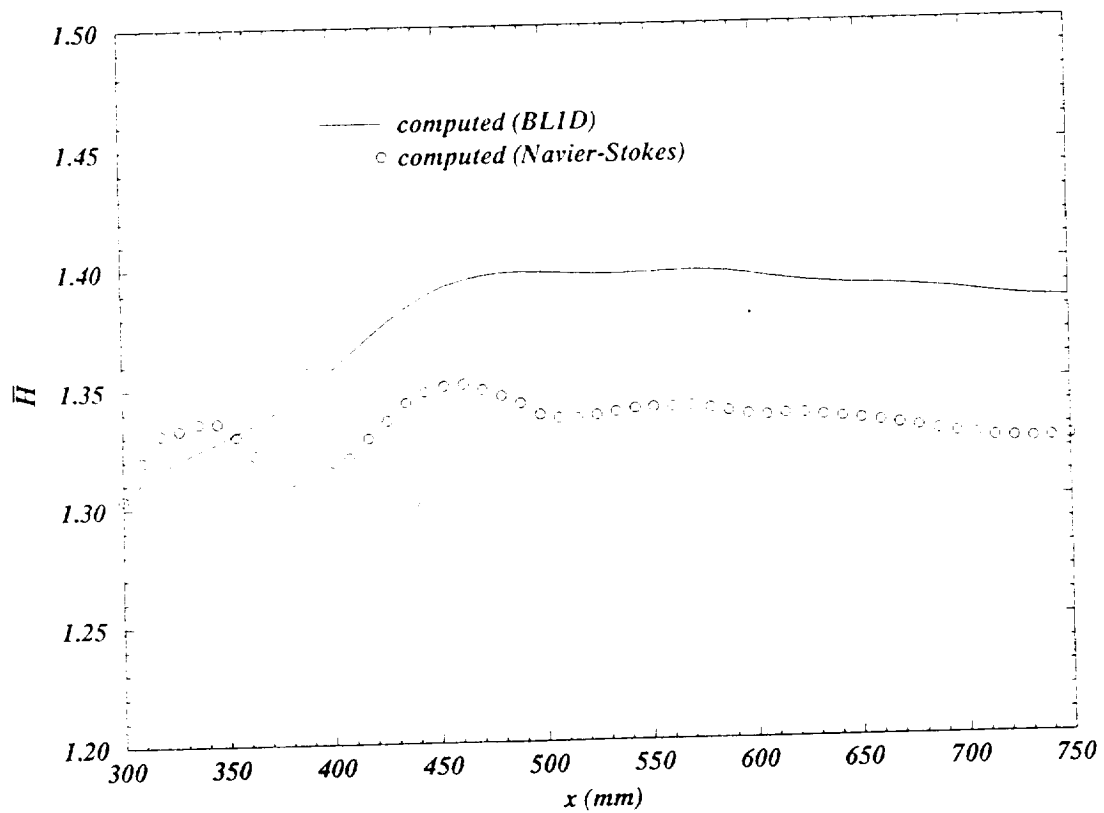
(d). Shape Factor

Figure 12. Navier-Stokes and BL1D Channel Parameters at $t \cong 1000$
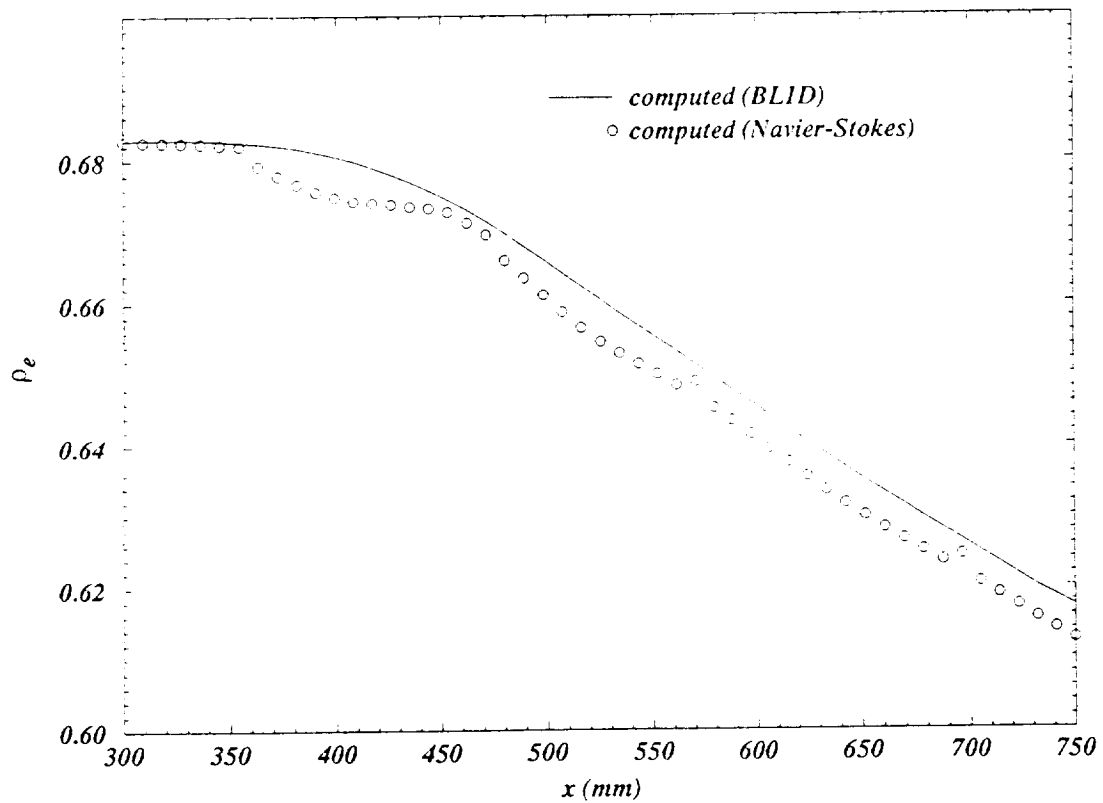
(a). Mach Number
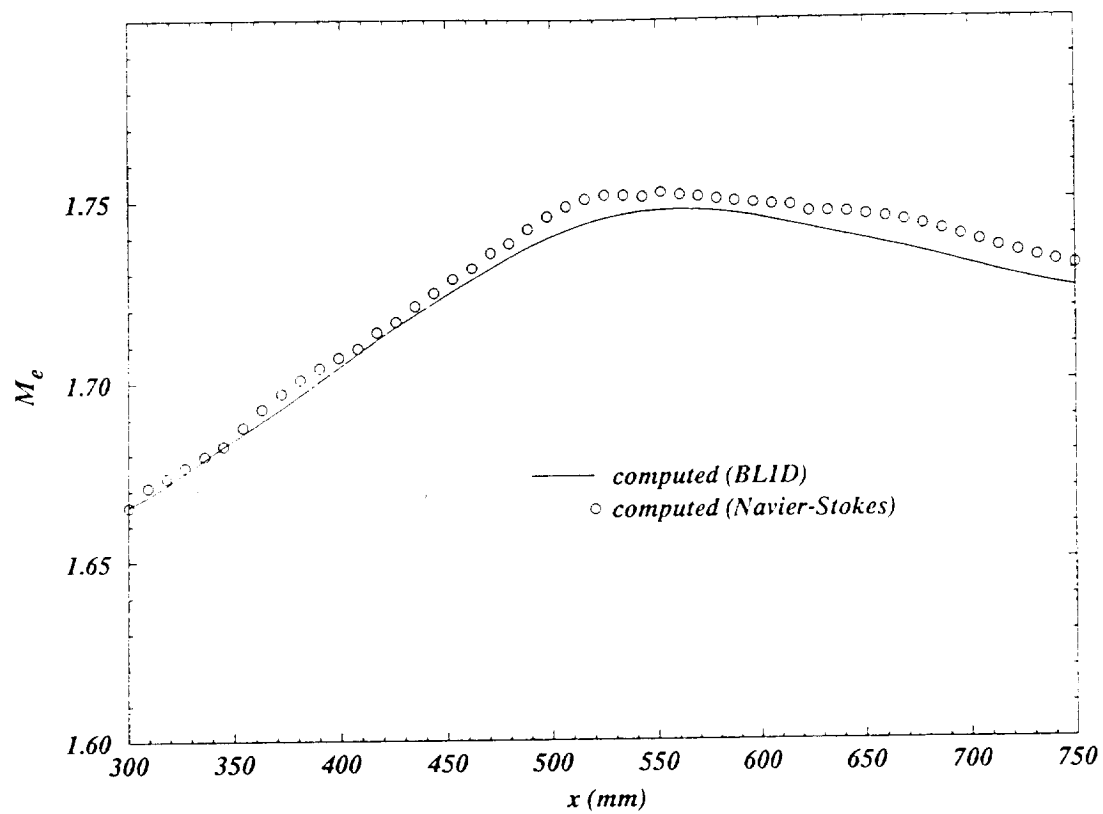
(b). Density
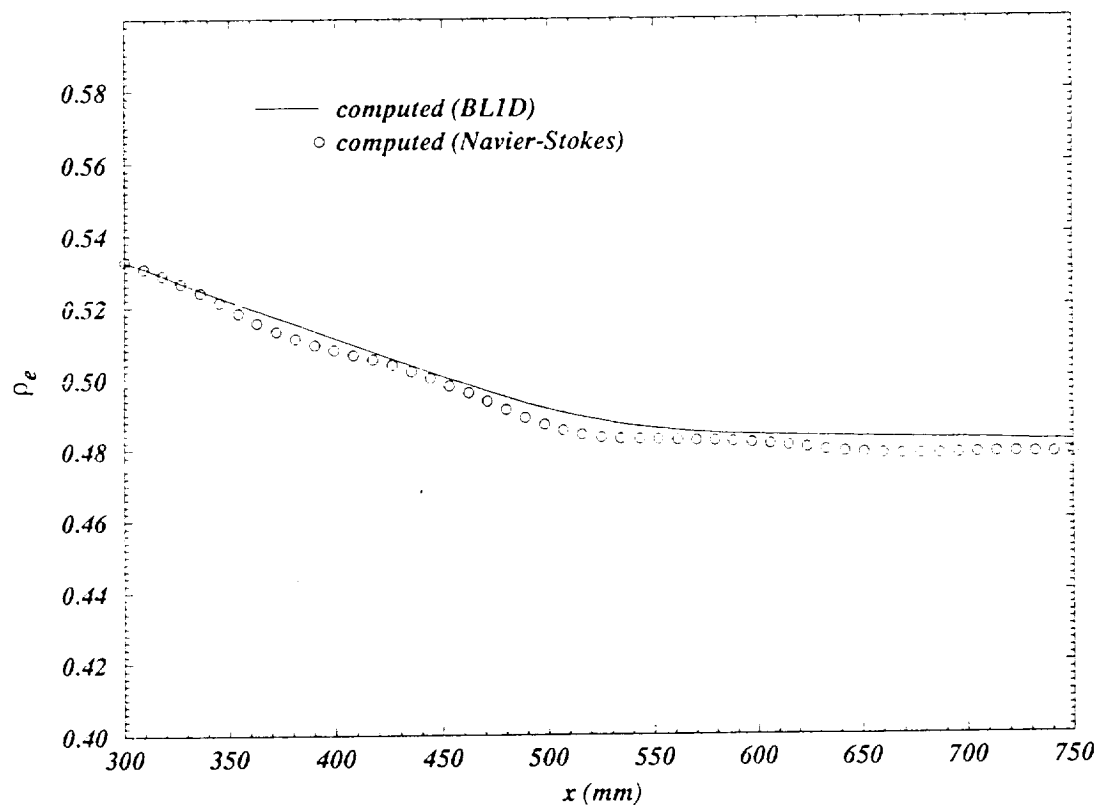
Figure 12. (Continued)

(c). Momentum Thickness

(d). Shape Factor

74

Figure 13. Navier-Stokes and BL1D Channel Parameters at $t \cong 2000$
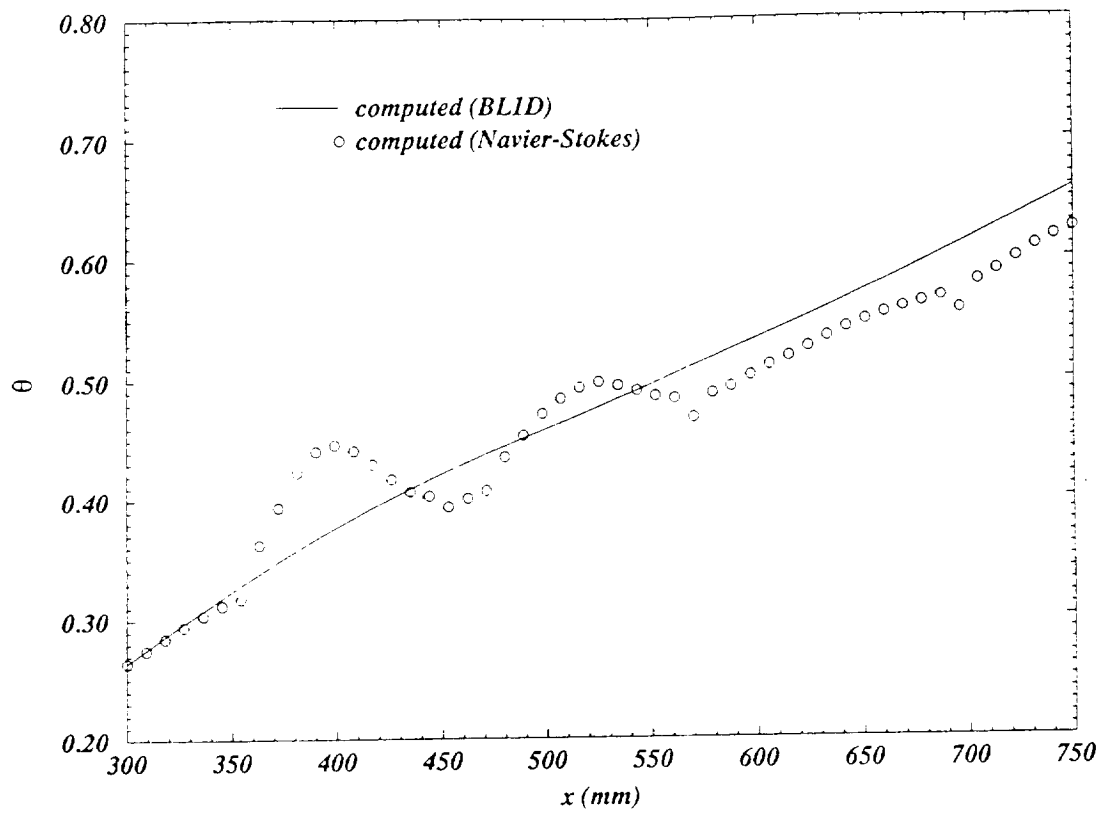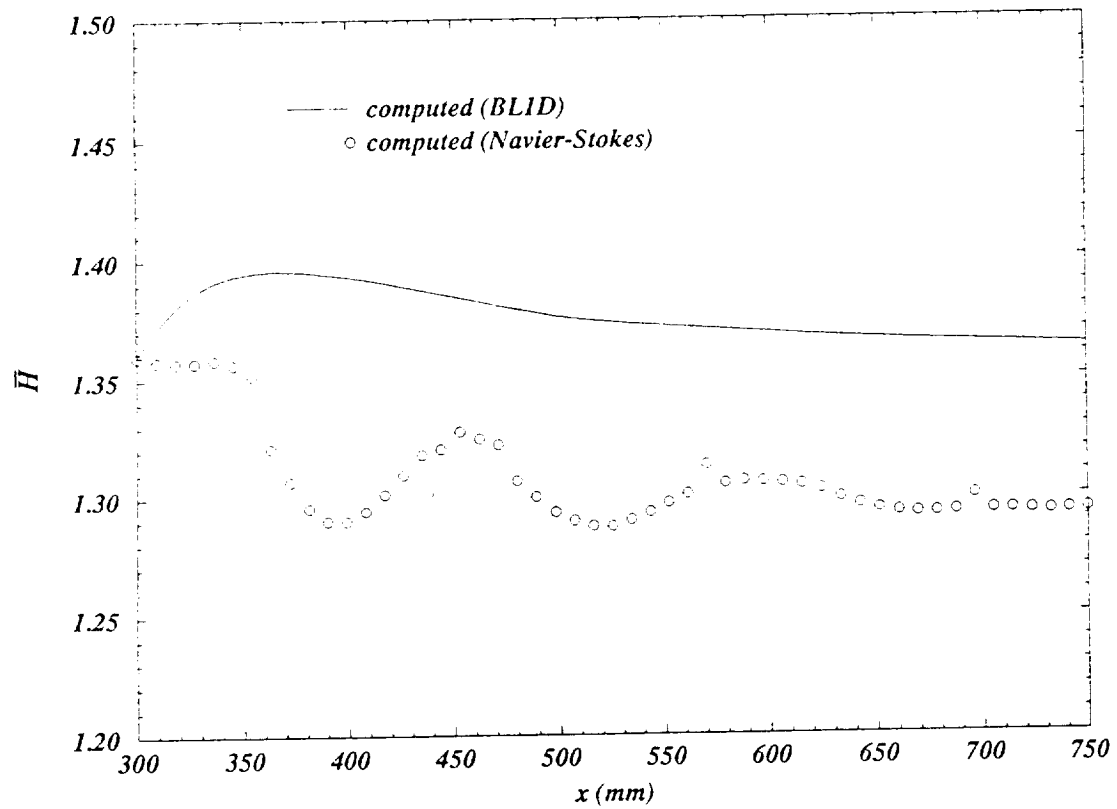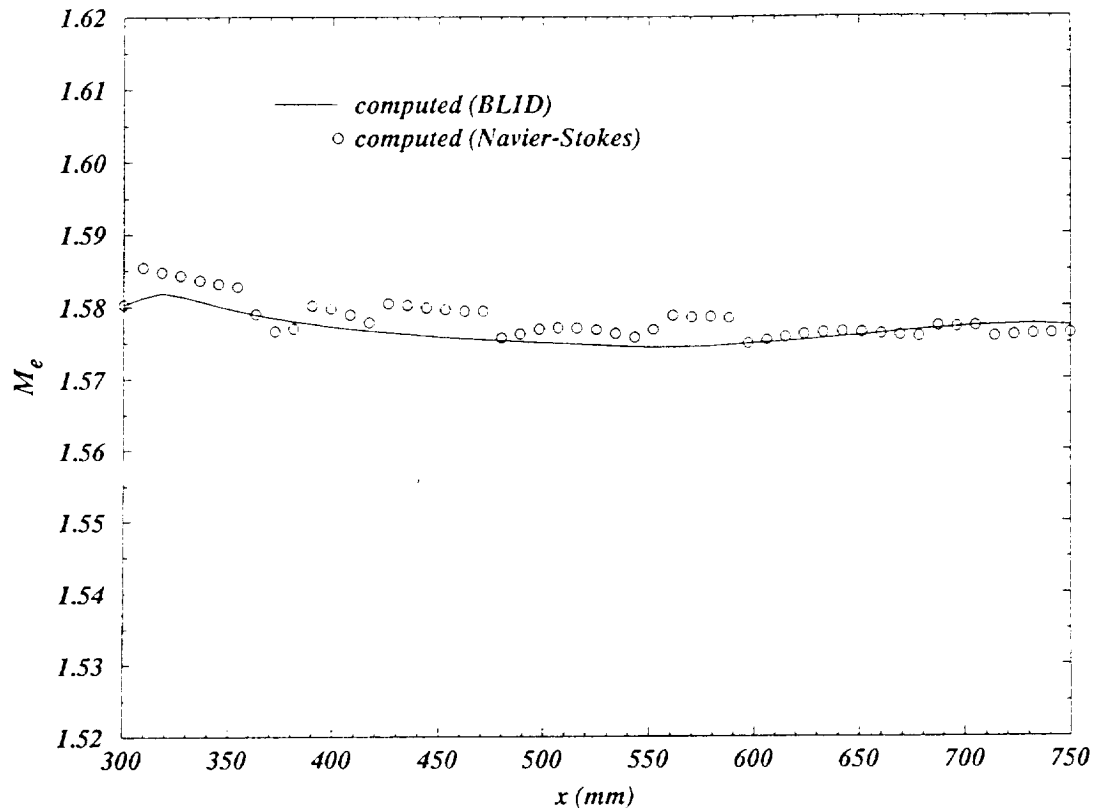
(a). Mach Number

(b). Density

Figure 13. (Continued)

(c). Momentum Thickness

(d). Shape Factor

76

Figure 14. Navier-Stokes and BL1D Channel Parameters at t ≅ 3000
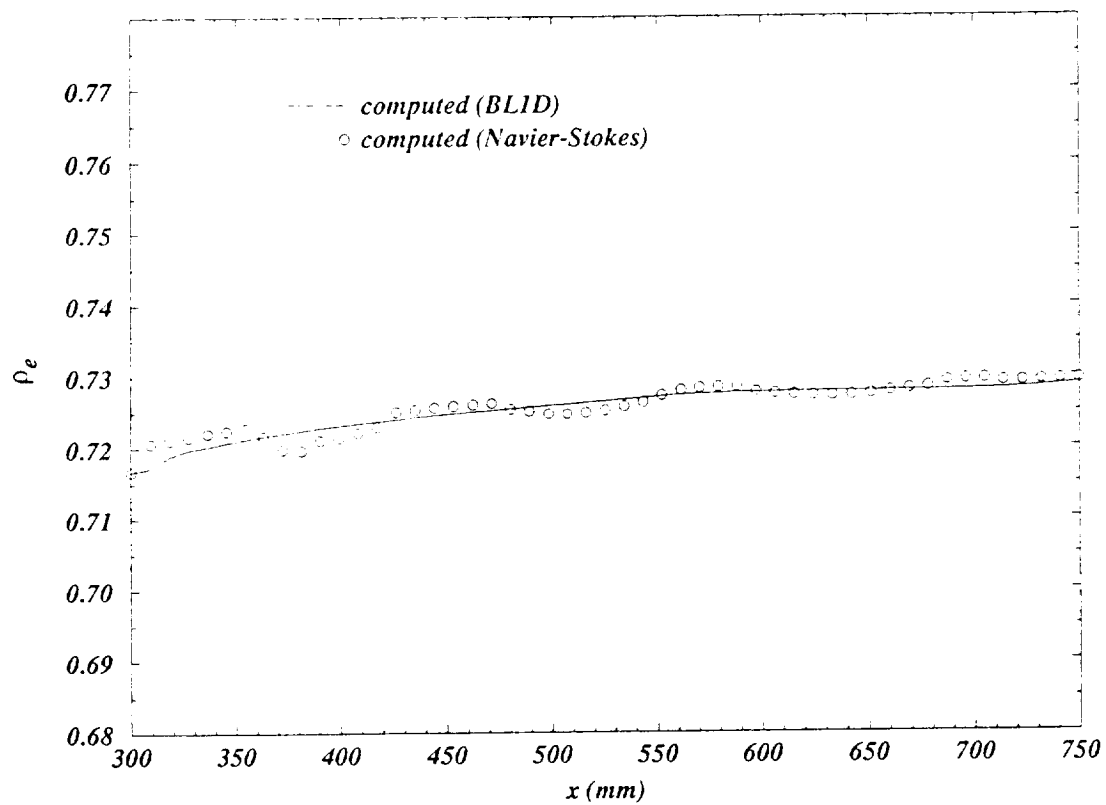
(a). Mach Number
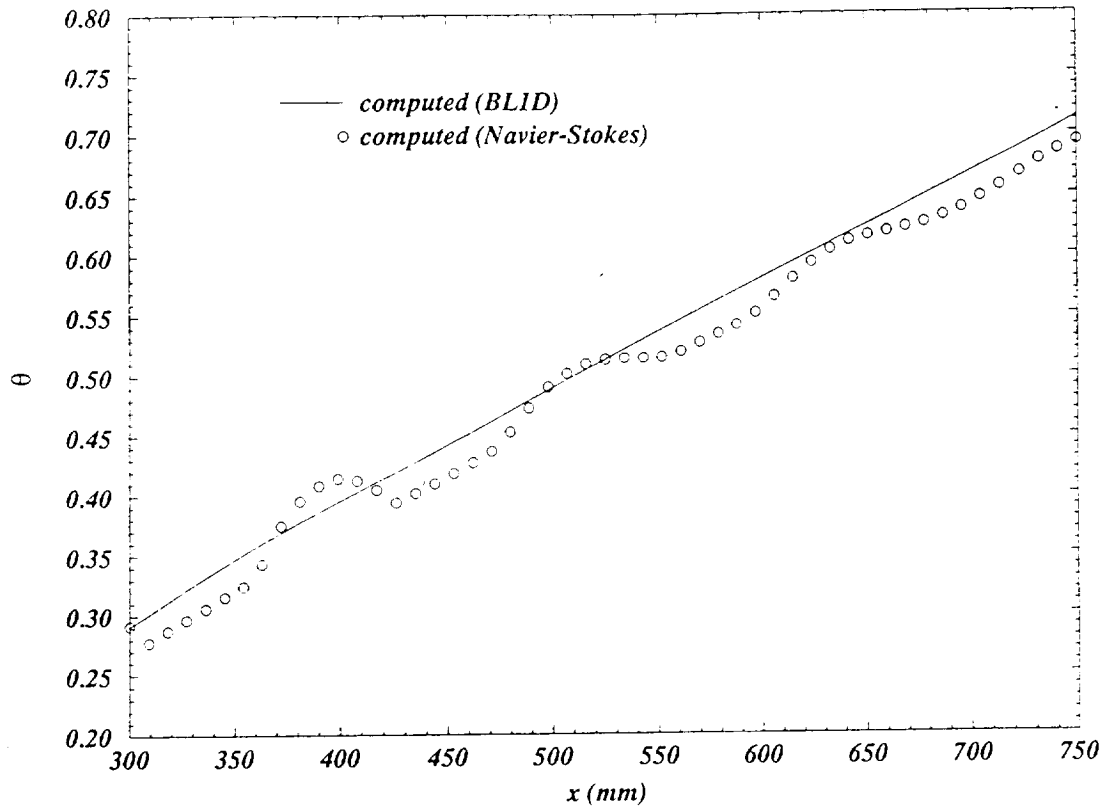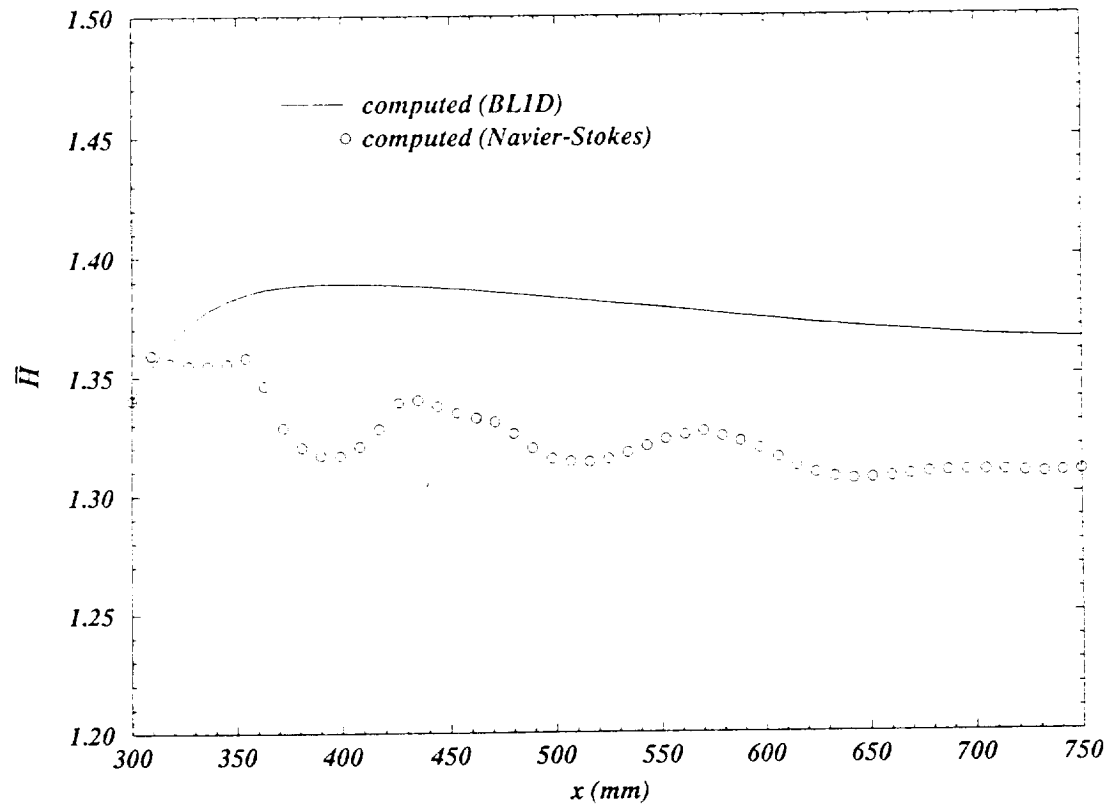

(b). Density

Figure 14. (Continued)

(c). Momentum Thickness

(d). Shape Factor

Figure 15. Momentum Thickness Distributions at $t \cong 1000$
(Navier-Stokes)
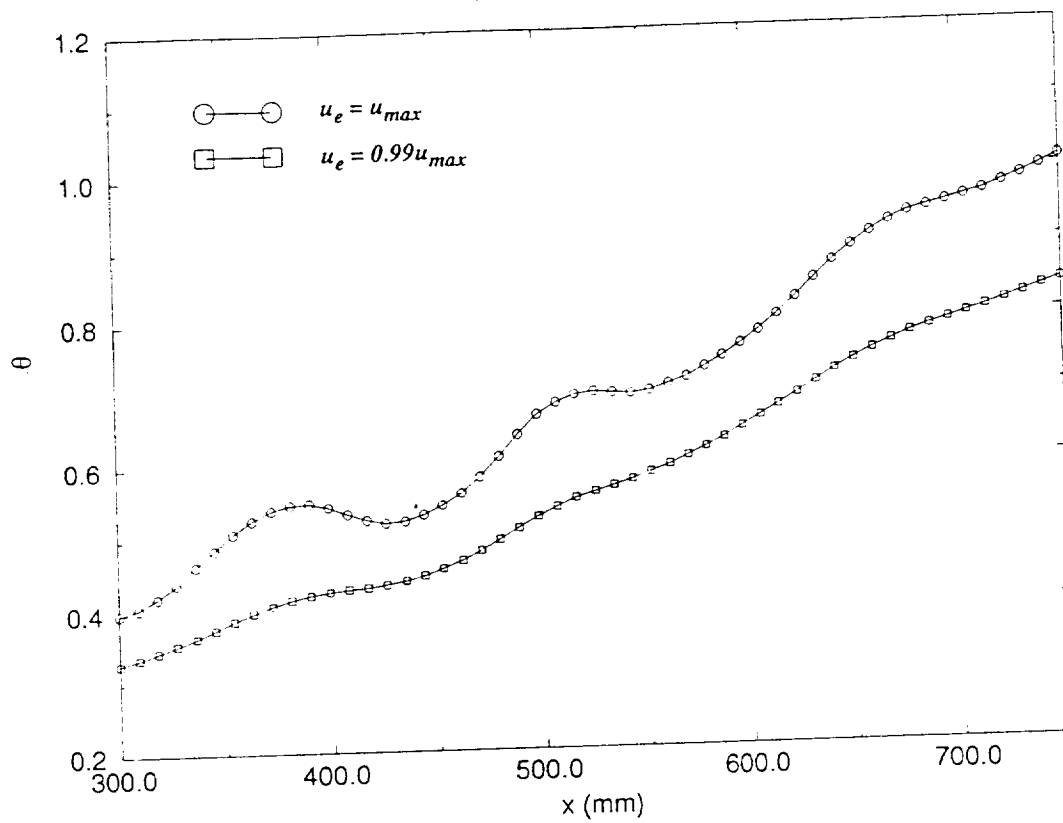
Figure 16. AGARD Test Case 1.2

(a). Experimental Test Configuration

35 pressure taps

60 pressure taps

100 x 120

9.997

2nd throat

72

88

346

443

Computational Domain

Note: All dimensions in mm

(b). Measured and Computed Wall Pressure

+   measured (AGARD)

⎯⎯⎯   computed (BL1D-I)

⎯ ⎯ ⎯   computed (inviscid)

$p_e/p_{0,\infty}$

x/h_t

80
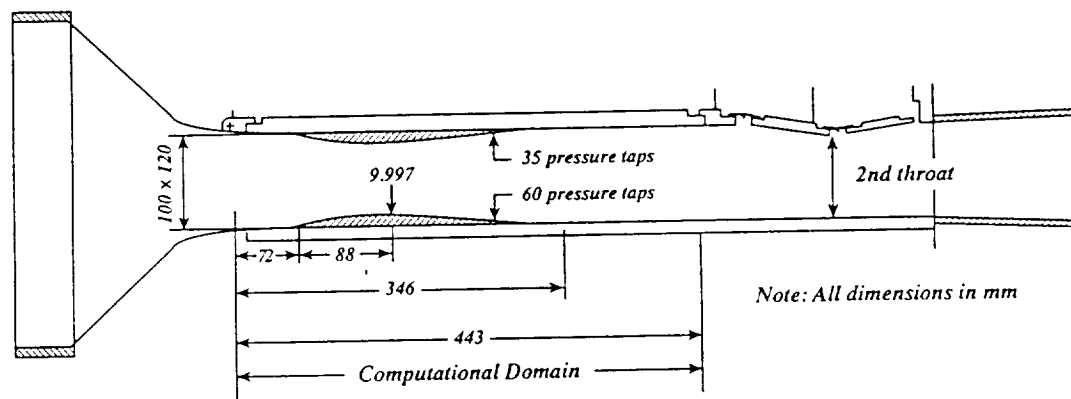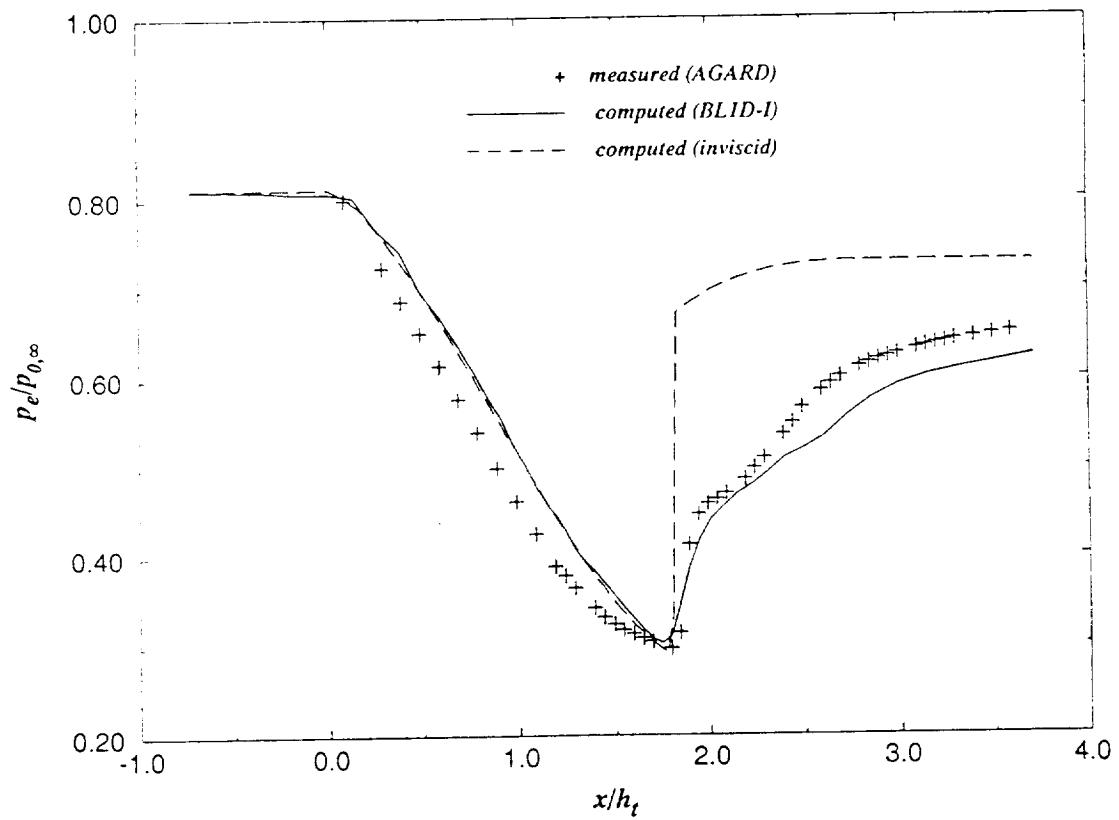
Figure 16. (Continued)

(c). Computed Skin Friction

(c). Computed Skin Friction

(d). Measured and Computed Boundary-Layer Shape Factor
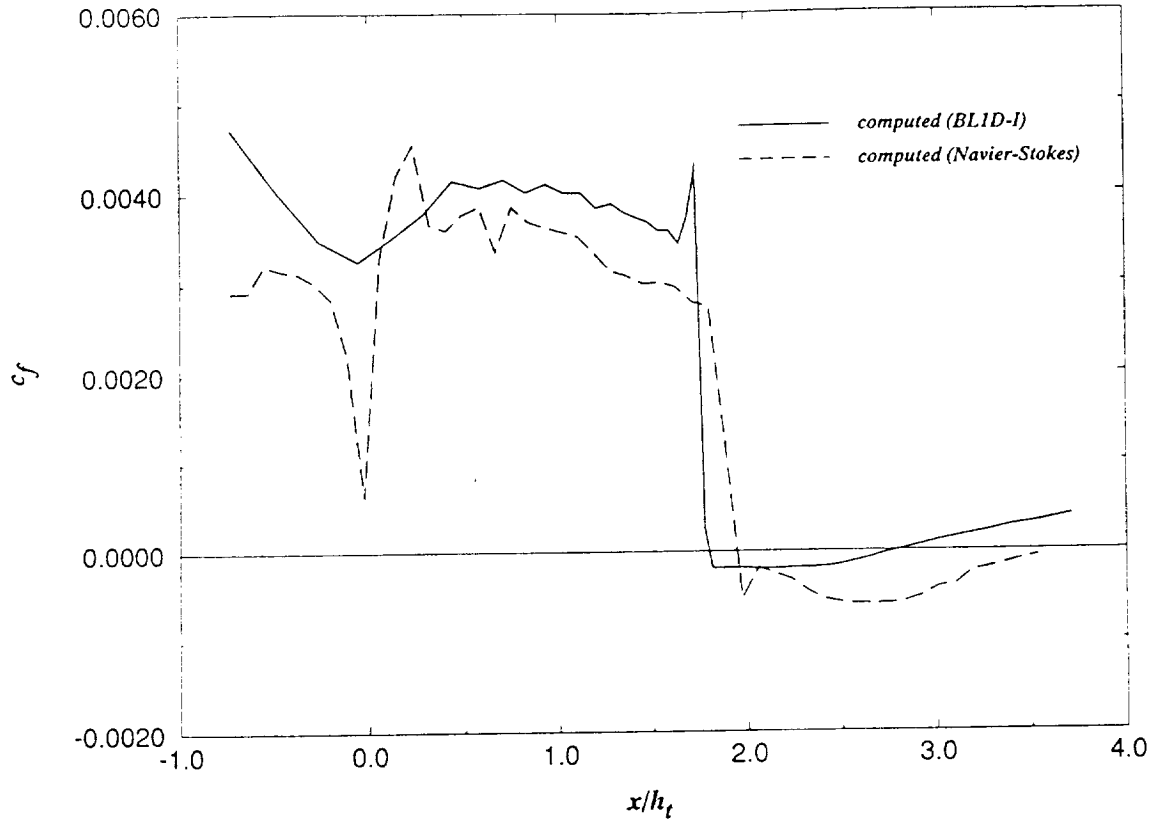
(d). Measured and Computed Boundary-Layer Shape Factor

Figure 16. (Continued)

(e). Measured and Computed Velocity Profiles at Various Axial Locations
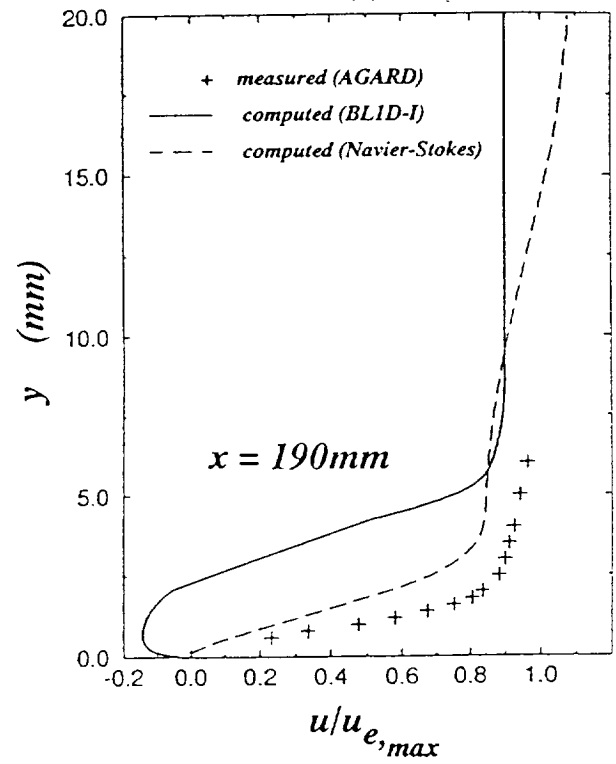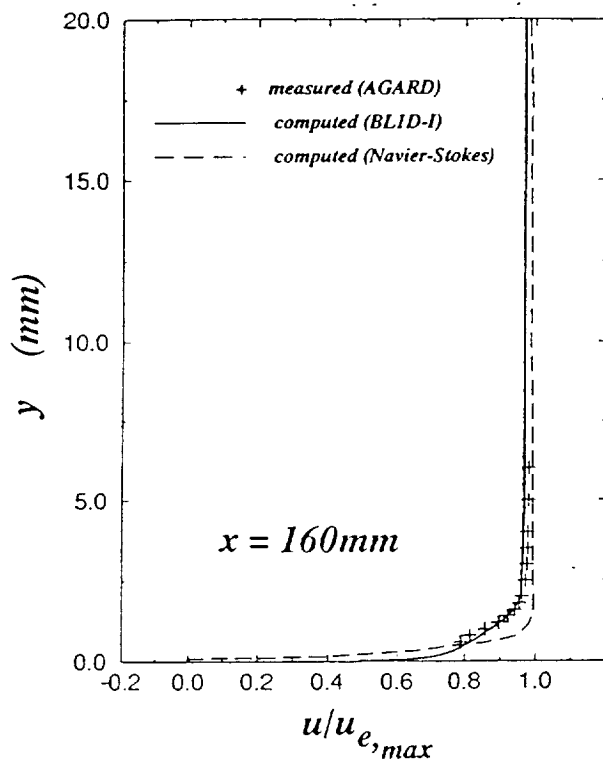
Figure 16. (Continued)

(f). Measured and Computed Displacement Surfaces

Figure 17. AGARD Test Case 1.3

(a.) Experimental Test Configuration

40 pressure taps on profile

21 taps on tunnel wall

2nd throat

995 x 120

78 — 186.37 — 100 — 74.34

Note: All dimensions in mm

Computational Domain
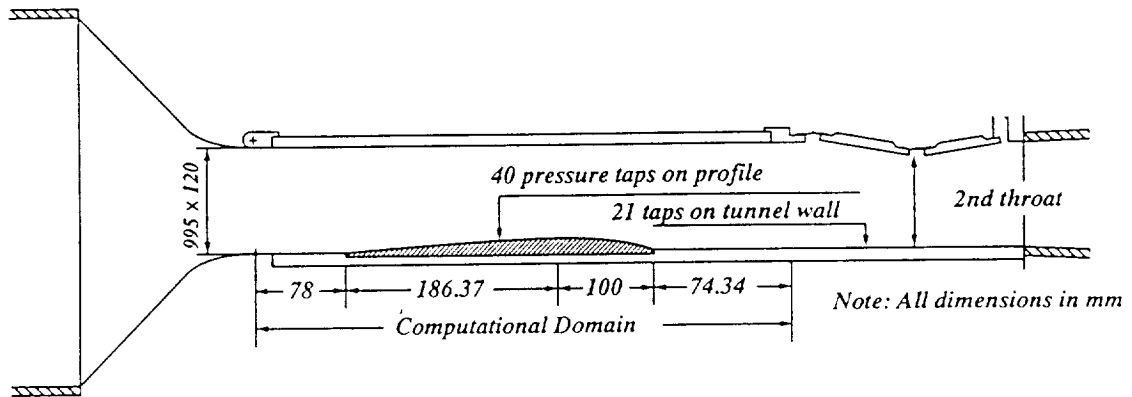
(b). Equivalent Wall Height Distribution

Actual Nozzle

Approximate Nozzle

y/R_{ref}

x/h_t
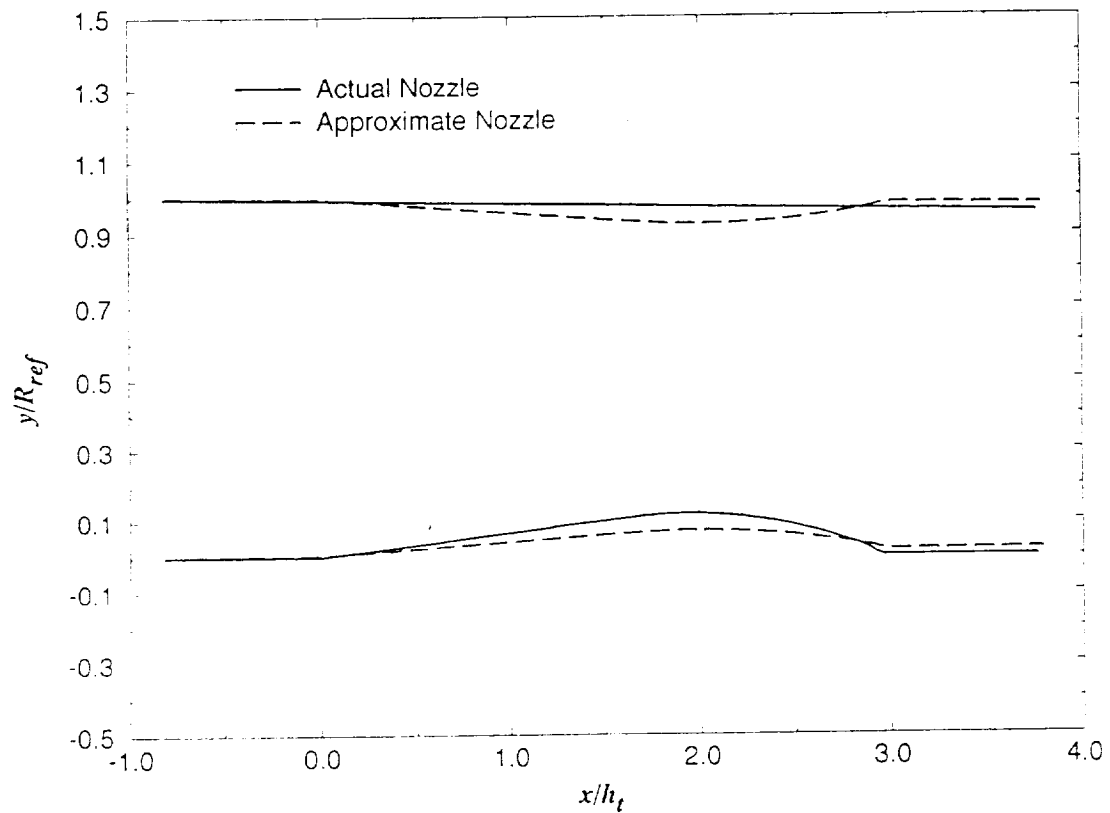
Figure 17. (Continued)

(c). Measured and Computed Wall Pressures (Measurements from Lower Wall Only)
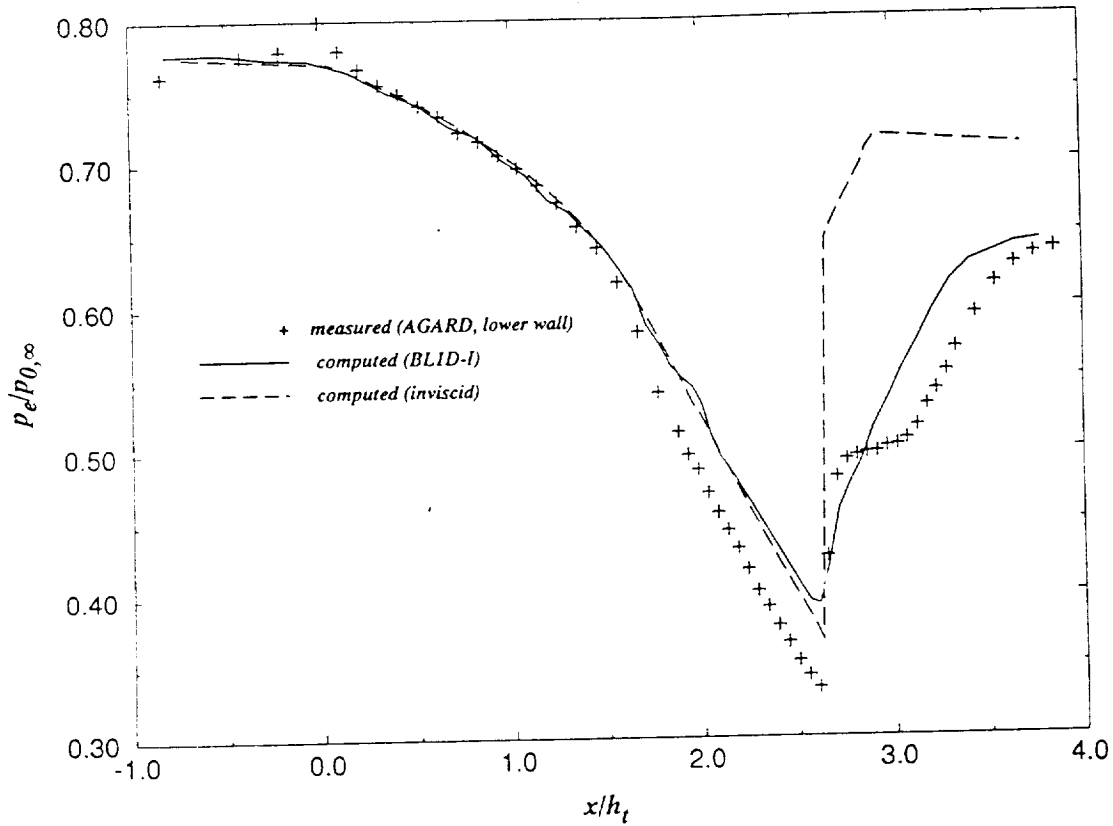
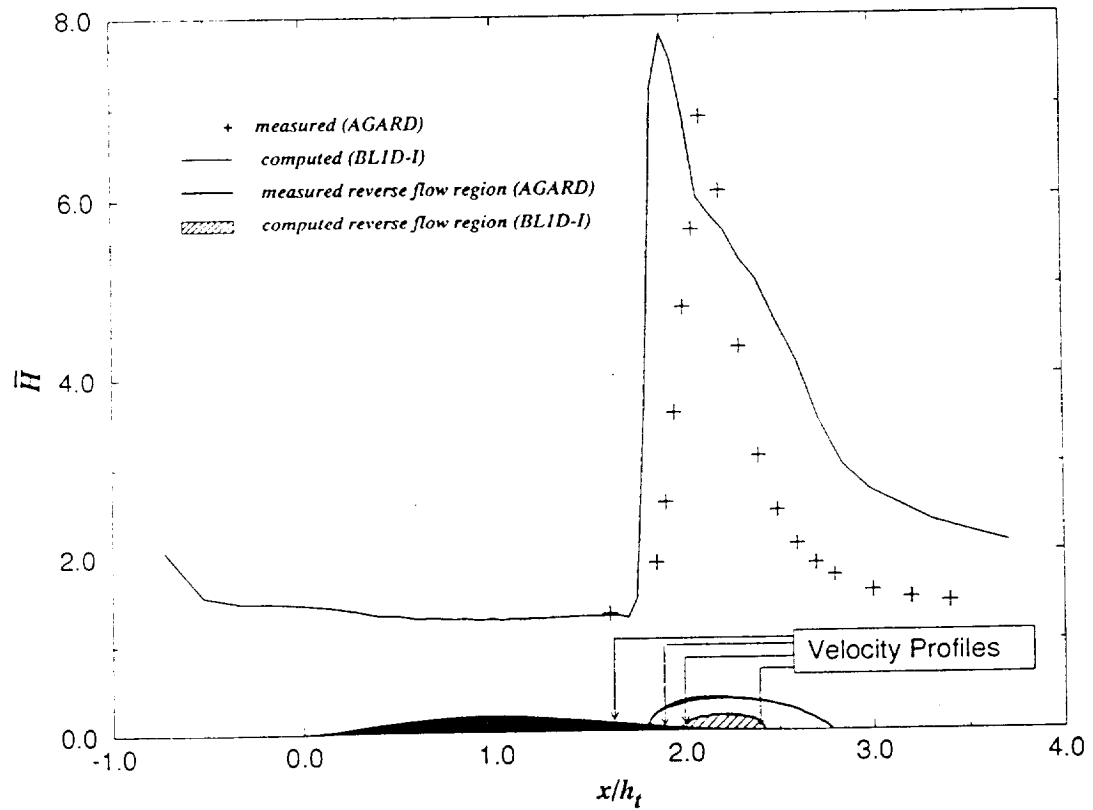*(d). Measured and Computed Wall Pressures (Measurements from Lower Wall Only)*
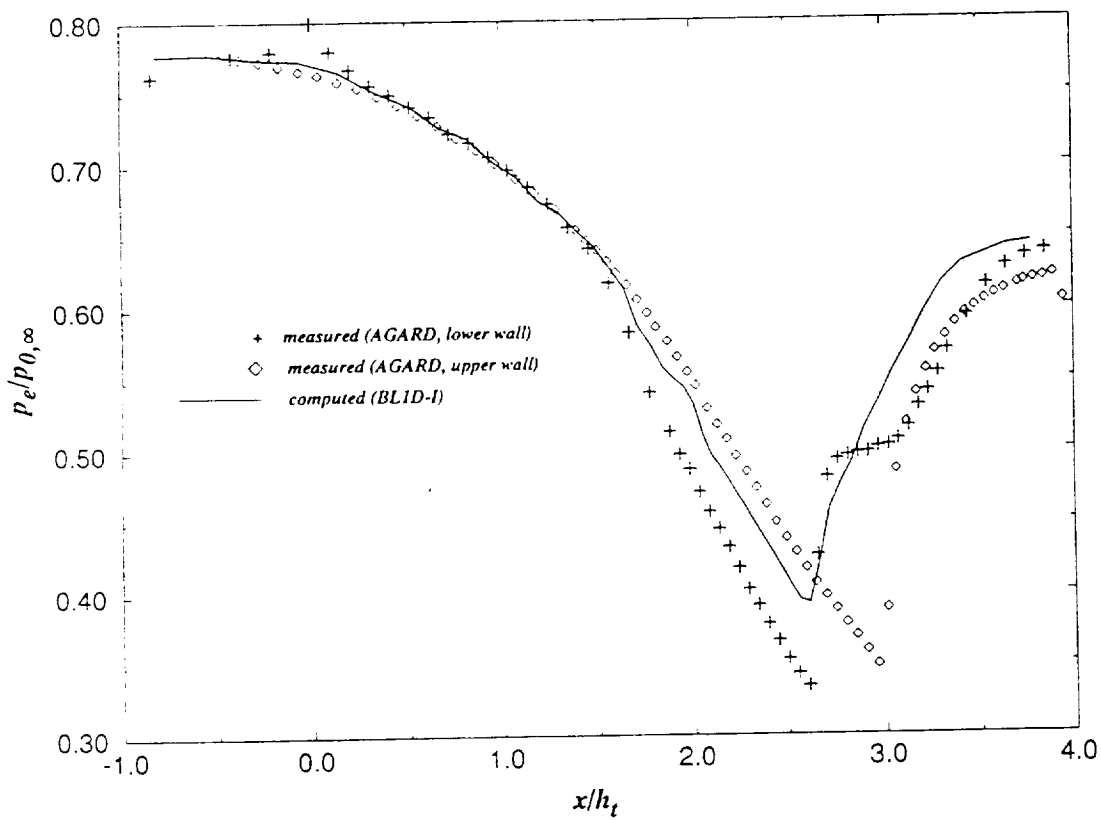
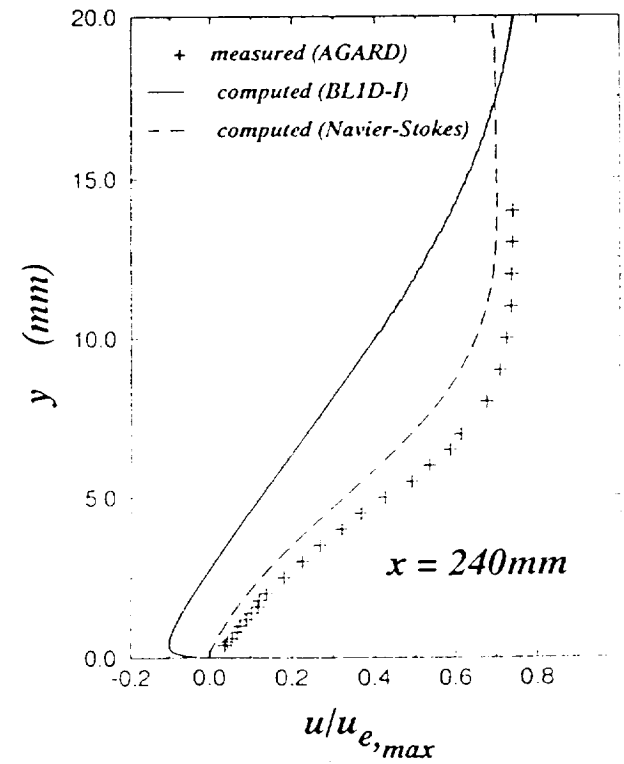## Figure 17. (Continued)

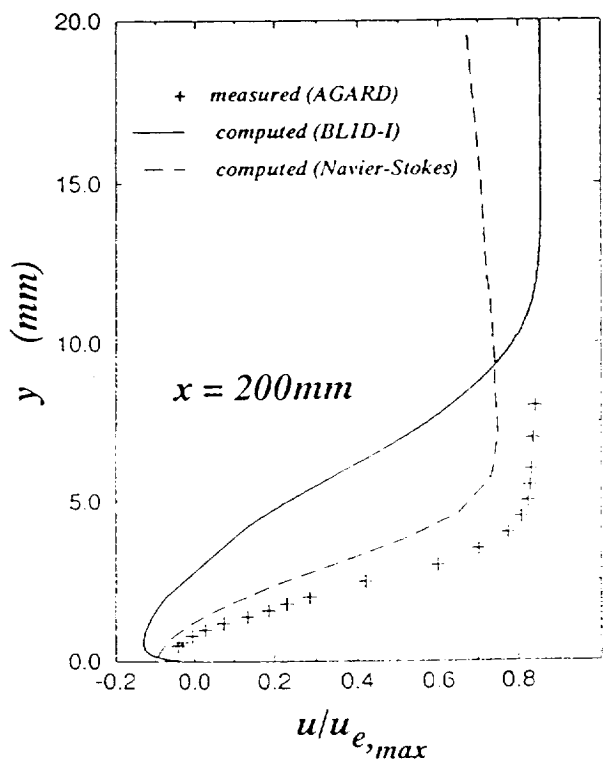### (e). Computed Skin Friction
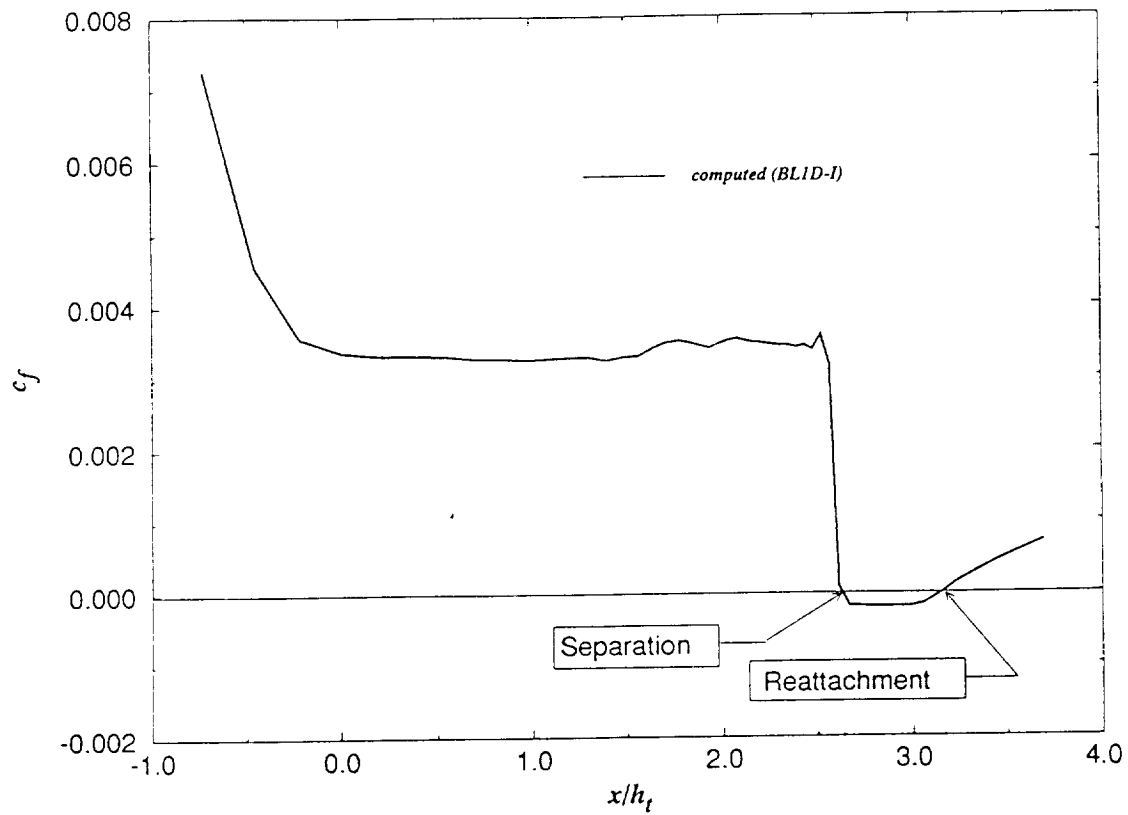
(f). Measured and Computed Boundary-Layer Shape Factor
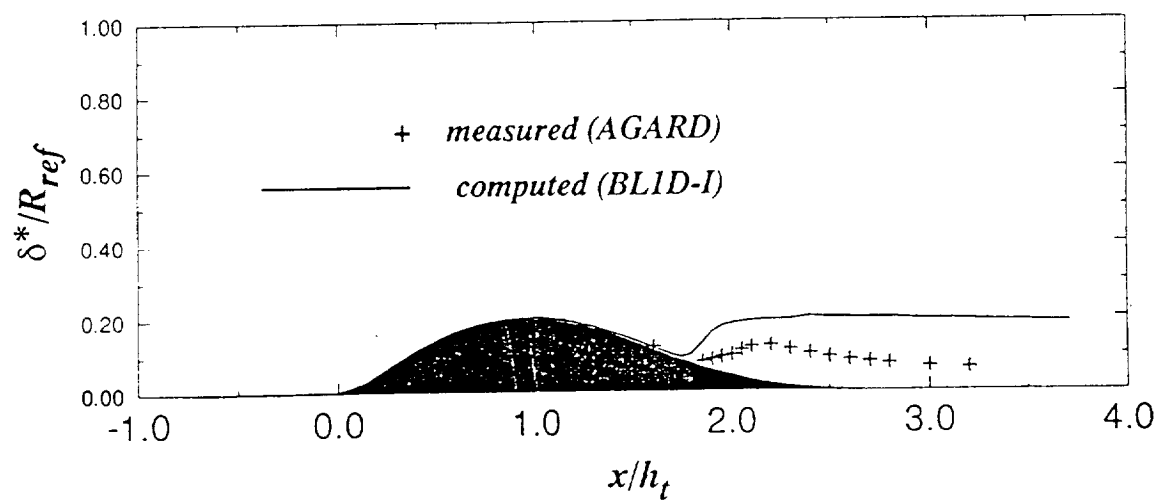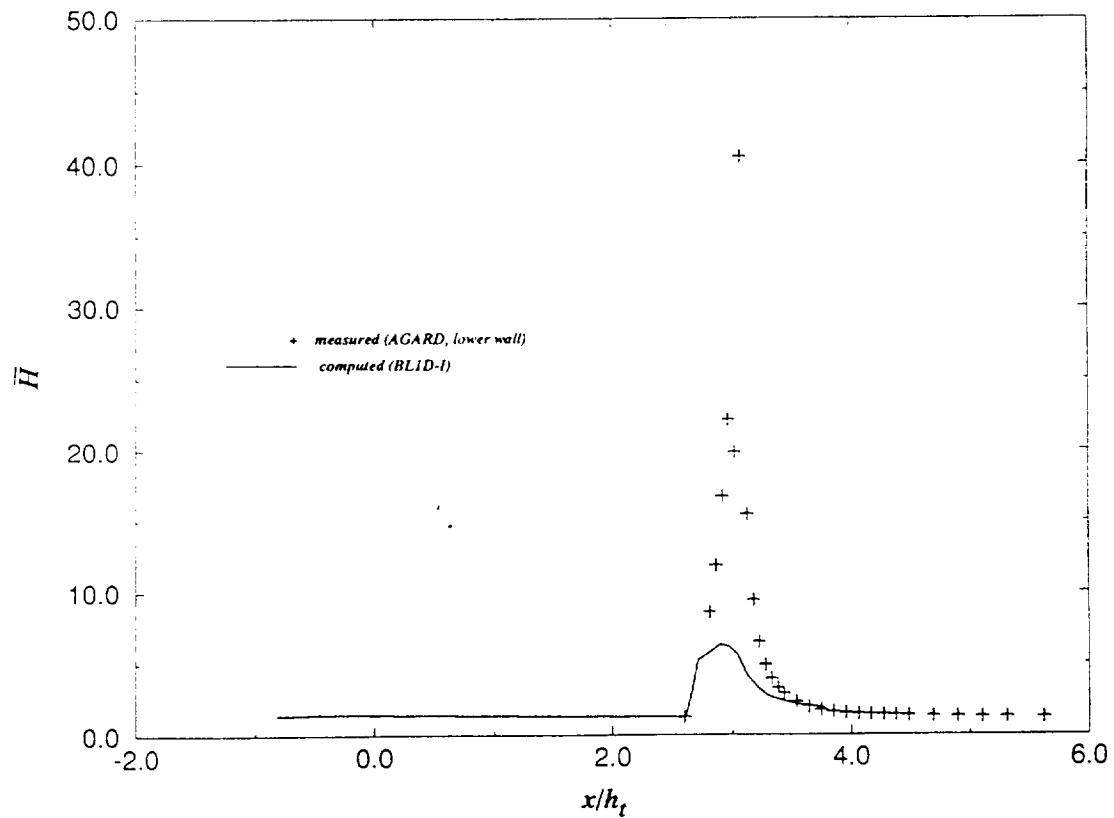
Figure 17. (Continued)

(g). Measured and Computed Velocity Profiles at Various Axial Locations
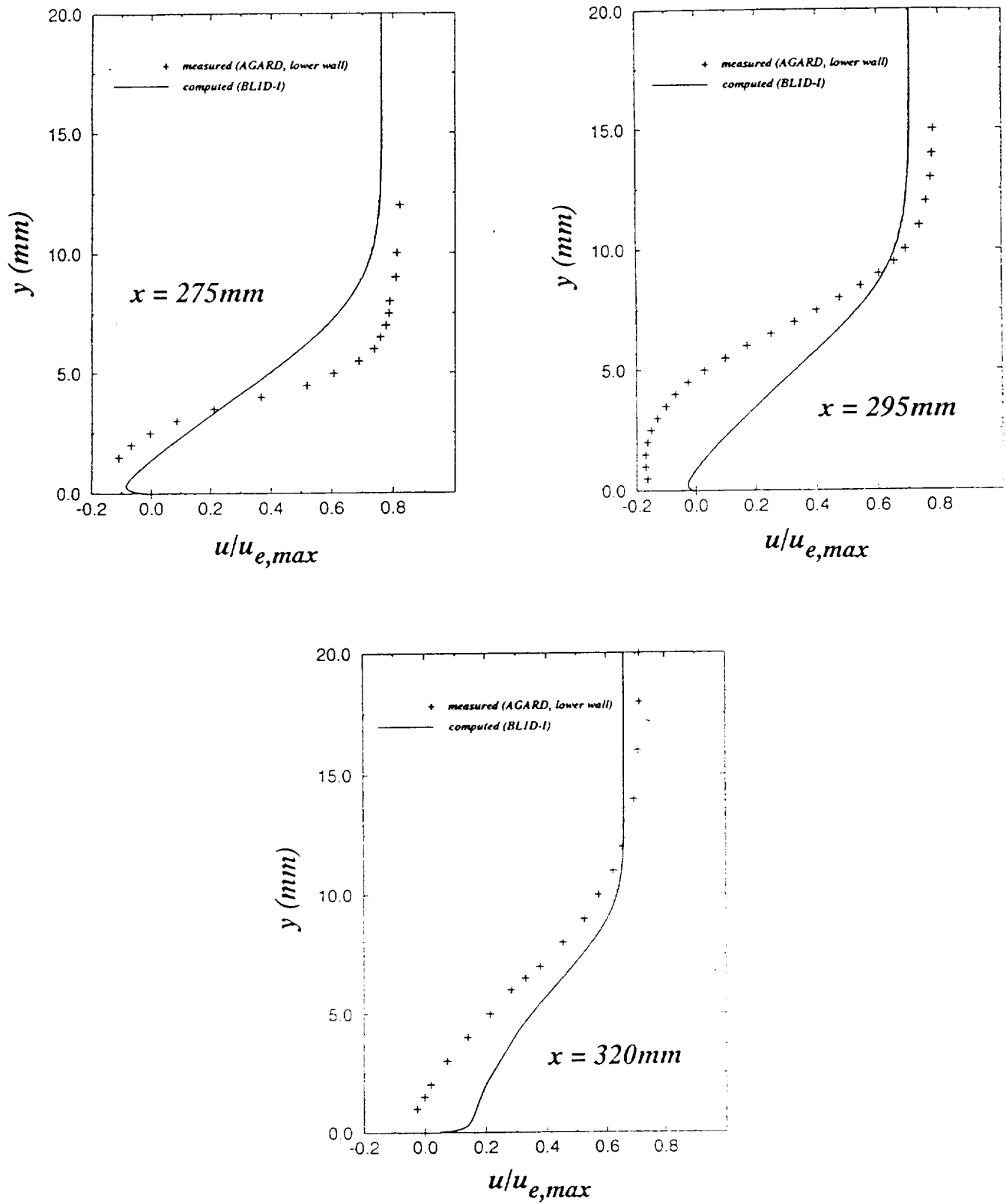
Figure 17. (Continued)

(h). Measured and Computed Displacement Surfaces

+ measured δ^*/R_{ref} (AGARD)

—— computed δ^*/R_{ref} (BL1D-I)

—— measured reverse flow region (AGARD)

---- computed reverse flow region (BL1D-I)

Velocity Profiles

δ^*/R_{ref}

x/h_t
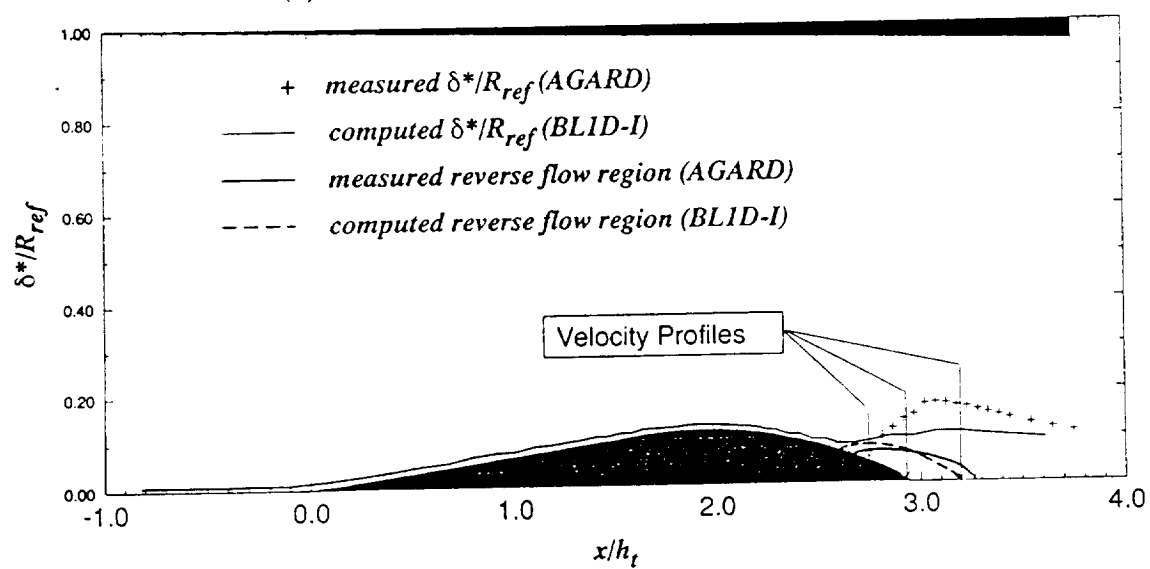
APPENDIX

I. Elements of the L and N Matrices

Recall that the system of equations can be written as

$$L\frac{\partial q}{\partial t} = b \tag{A.I.1}$$

or, in quasi–linear form,

$$L\frac{\partial q}{\partial t} + N\frac{\partial q}{\partial x} = d \tag{A.I.2}$$

Elements of the L and N matrices are given below for all formulations and were obtained using the auxiliary relations reported elsewhere in this Appendix. Each particular element is referred to by either lower case ℓ (for L) or n (for N) using double subscripts (ij), where i and j represent the specific matrix row and column, respectively.

Listed first are the L and N matrix elements resulting from the dependent variable vector given by

$$q = (\varrho_e \quad u_e \quad M_e \quad \theta \quad \overline{H})^T$$

Although the ratio $T_{0,e} = \hat{T}_{0,e}/\hat{T}_{0,\infty}$ appears in several terms, all computations using this formulation have been made using the assumption $T_{0,e} = 1$. It should be further noted that additional terms involving derivatives of this quantity were neglected in the original formulation, i.e.,

$$\frac{\partial T_{0,e}}{\partial t} = \frac{\partial T_{0,e}}{\partial x} = 0$$

L Matrix Using M_e as Dependent Variable ($T_{0,e}$ assumed constant)

$$l_{11} = u_e\theta \ (H_{\delta^*} - H_{\theta_\varrho})$$

$$l_{12} = \varrho_e\theta H_{\delta^*}$$

$$l_{13} = 2\varrho_e u_e M_e\theta \ (c_5\overline{H} + c_6)$$

$$l_{14} = \varrho_e u_e(H_{\delta^*} - H_{\theta_\varrho})$$

$$l_{15} = \varrho_e u_e\theta(1 + c_5 M_e^2)$$

$$l_{21} = \theta u_e^2(1 + H_{\delta^*} - H_{\theta_\varrho})$$

$$l_{22} = 2\varrho_e u_e\theta\left(1 + H_{\delta^*} - \frac{\delta_u^*}{\theta}\right)$$

$$l_{23} = 2\varrho_e u_e^2 M_e\theta(c_5\overline{H} + c_6)$$

89

$$l_{24} = \varrho_e u_e^2(1 + H_{\delta^*} - H_{\theta_\varrho})$$

$$l_{25} = \varrho_e u_e^2 \theta(1 + c_5 M_e^2)$$

$$l_{31} = A$$

$$l_{32} = 0$$

$$l_{33} = -2\varrho_e M_e \theta \overline{w} \ (c_1 \overline{H} + c_2)$$

$$l_{34} = \varrho_e \overline{w} H_{\delta^*}$$

$$l_{35} = -\varrho_e \theta \overline{w}(1 + c_1 M_e^2)$$

$$l_{41} = u_e A$$

$$l_{42} = \varrho_e A$$

$$l_{43} = -2\varrho_e u_e M_e \theta \overline{w} \ (c_1 \overline{H} + c_2)$$

$$l_{44} = -\varrho_e u_e \overline{w} H_{\delta^*}$$

$$l_{45} = -\varrho_e u_e \theta \overline{w}(1 + c_1 M_e^2)$$

$$l_{51} = A\left(\tilde{e}_e T_{0,e} + \frac{1}{2} u_e^2\right)$$

$$l_{52} = \varrho_e u_e A$$

$$l_{53} = -2(E_e + p_e)\overline{w}\theta M_e \ (c_1 \overline{H} + c_2) - \frac{A\varrho_e M_e T_{0,e}}{\gamma f_e^2}$$

$$l_{54} = -(E_e + p_e)\overline{w} H_{\delta^*}$$

$$l_{55} = -(E_e + p_e)\overline{w}\theta \ (1 + c_1 M_e^2)$$

N Matrix Using M_e as Dependent Variable ($T_{0,e}$ assumed constant)

$$n_{11} = \theta u_e^2$$

$$n_{12} = \varrho_e u_e \theta(H_{\delta^*} + 2)$$

$$n_{13} = 0$$

$$n_{14} = \varrho_e u_e^2$$

$$n_{15} = 0$$

$$n_{21} = \theta u_e^3 H_{\theta^*}$$

$$n_{22} = \varrho_e u_e^2 \theta\left(3H_{\theta^*} + 2H_{\delta^*} - 2\frac{\delta_u^*}{\theta}\right)$$

$$n_{23} = \varrho_e u_e^3 \theta \frac{\partial H_{\theta^*}}{\partial M_e}$$

$$n_{24} = \varrho_e u_e^3 H_{\theta^*}$$

C-2

$$n_{25} = \varrho_e u_e^3 \theta \frac{\partial H_{\theta^*}}{\partial \overline{H}}$$

$$n_{31} = u_e A$$

$$n_{32} = \varrho_e A$$

$$n_{33} = -2\varrho_e u_e M_e \theta \overline{w}(c_1 H + c_2)$$

$$n_{34} = -\varrho_e u_e \overline{w} H_{\delta^*}$$

$$n_{35} = -\varrho_e u_e \theta \overline{w}(1 + c_1 M_e^2)$$

$$n_{41} = A[(\gamma - 1)\bar{e}_e T_{0,e} + u_e^2]$$

$$n_{42} = 2\varrho_e u_e A$$

$$n_{43} = -2\varrho_e u_e^2 \theta M_e \overline{w}(c_1 \overline{H} + c_2) - \frac{\gamma - 1}{\gamma} \frac{A\varrho_e M_e}{f_e^2} T_{0,e}$$

$$n_{44} = -\varrho_e u_e^2 \overline{w} H_{\delta^*}$$

$$n_{45} = -\varrho_e u_e^2 \theta \overline{w}(1 + c_1 M_e^2)$$

$$n_{51} = u_e A\left(\gamma \bar{e}_e T_{0,e} + \frac{1}{2} u_e^2\right)$$

$$n_{52} = A(E_e + p_e + \varrho_e u_e^2)$$

$$n_{53} = -2(E_e + p_e)u_e \overline{w}\theta M_e(c_1 \overline{H} + c_2) - \frac{\varrho_e u_e M_e A}{f_e^2} T_{0,e}$$

$$n_{54} = -(E_e + p_e)u_e \overline{w} H_{\delta^*}$$

$$n_{55} = -(E_e + p_e)u_e \overline{w}\theta(1 + c_1 M_e^2)$$

Also, the following definitions have been used:

$$c_1 = 0.113$$
$$c_2 = 0.290$$
$$c_3 = 0.185$$
$$c_4 = 0.150$$
$$c_5 = c_1 - c_3$$
$$c_6 = c_2 - c_4$$
$$A = w(R - \delta^*)$$
$$w = \begin{cases} 2, \; planar \\ \frac{1}{2}(R - \delta^*), \; axisymmetric \end{cases}$$

91

$$\bar{w} = \begin{cases} w, \ planar \\ 2w, axisymmetric \end{cases}$$

$$e_e = \bar{e}_e T_{0,e} = \frac{T_{0,e}}{\gamma(\gamma - 1)f_e} = \frac{u_e^2}{\gamma(\gamma - 1)M_e^2} = \frac{T_e}{\gamma(\gamma - 1)}$$

$$E_e = \varrho_e\left(\bar{e}_e T_{0,e} + \frac{1}{2}u_e^2\right) = \varrho_e\left(\frac{T_e}{\gamma(\gamma - 1)} + \frac{1}{2}u_e^2\right)$$

$$p_e = \frac{\varrho_e T_e}{\gamma}$$

$$E_e + p_e = \varrho_e\left(\gamma e_e + \frac{1}{2}u_e^2\right)$$

$$f_e = 1 + \frac{\gamma - 1}{2}M_e^2$$

Listed next are the L and N matrix elements using Mach number as a dependent variable, where no assumption regarding $T_{0,e} = $ constant is made. For convenience, most elements are written in terms of those given previously. Matrix elements given below are written with superscript M to indicate that Mach number is used as the dependent variable and that stagnation temperature is not assumed constant.

L Matrix Elements Using Mach Number as Dependent Variable
($T_{0,e}$ not assumed constant)

$$l_{11}^M = l_{11}$$

$$l_{12}^M = l_{12}$$

$$l_{13}^M = l_{13}$$

$$l_{14}^M = l_{14}$$

$$l_{15}^M = l_{15}$$

$$l_{21}^M = l_{21}$$

$$l_{22}^M = l_{22}$$

$$l_{23}^M = l_{23}$$

$$l_{24}^M = l_{24}$$

$$l_{25}^M = l_{25}$$

$$l_{31}^M = l_{31}$$

$$l_{32}^M = l_{32}$$

$$l_{33}^M = l_{33}$$

$$l_{34}^M = l_{34}$$

$$l_{35}^M = l_{35}$$

$$l_{41}^M = l_{41}$$

$$l_{42}^M = l_{42}$$

$$l_{43}^M = l_{43}$$

$$l_{44}^M = l_{44}$$

$$l_{45}^M = l_{45}$$

$$l_{51}^M = Ak_M u_e^2$$

$$l_{52}^M = 2Ak_M \varrho_e u_e$$

$$l_{53}^M = -\frac{2A\varrho_e u_e^2}{\gamma(\gamma-1)M_e^3} - 2(E_e + p_e)\overline{w}\theta M_e(c_1\overline{H} + c_2)$$

$$l_{54}^M = l_{54}$$

$$l_{55}^M = l_{55}$$

N Matrix Elements Using Mach Number as Dependent Variable
($T_{0,e}$ not assumed constant)

$$n_{11}^M = n_{11}$$

$$n_{12}^M = n_{12}$$

$$n_{13}^M = n_{13}$$

$$n_{14}^M = n_{14}$$

$$n_{15}^M = n_{15}$$

$$n_{21}^M = n_{21}$$

$$n_{22}^M = n_{22}$$

$$n_{23}^M = n_{23}$$

$$n_{24}^M = n_{24}$$

$$n_{25}^M = n_{25}$$

93

$$n_{31}^M = n_{31}$$

$$n_{32}^M = n_{32}$$

$$n_{33}^M = n_{33}$$

$$n_{34}^M = n_{34}$$

$$n_{35}^M = n_{35}$$

$$n_{41}^M = Au_e^2 + \frac{Au_e^2}{\gamma M_e^2}$$

$$n_{42}^M = 2\varrho_e u_e A + \frac{2A\varrho_e u_e}{\gamma M_e^2}$$

$$n_{43}^M = -\frac{2A\varrho_e u_e^2}{\gamma M_e^3} - 2\varrho_e u_e^2 \overline{w}\theta M_e(c_1\overline{H} + c_2)$$

$$n_{44}^M = n_{44}$$

$$n_{45}^M = n_{45}$$

$$n_{51}^M = Au_e^3 \overline{k}_M$$

$$n_{52}^M = A(E_e + p_e + 2\varrho_e u_e^2 \overline{k}_M)$$

$$n_{53}^M = -\frac{2A\varrho_e u_e^3}{(\gamma - 1)M_e^3} - 2(E_e + p_e)u_e \overline{w}\theta M_e(c_1\overline{H} + c_2)$$

$$n_{54}^M = n_{54}$$

$$n_{55}^M = n_{55}$$

Note the following relations have been used:

$$k_M = \frac{1}{2} + \frac{1}{\gamma(\gamma - 1)M_e^2}$$

$$\overline{k}_M = \frac{1}{2} + \frac{1}{(\gamma - 1)M_e^2} = \frac{1}{2}(1 - \gamma) + \gamma k_M$$

Finally, the L and N matrix elements resulting from the dependent variable vector given by

$$q = (\varrho_e \quad u_e \quad p_e \quad \theta \quad \overline{H})^T$$

are listed. As previously discussed, no assumptions of constant stagnation temperature are required. Matrix elements listed below are written with superscript p to signify that pressure was used as a dependent variable. Again for convenience, most elements are written in terms of those previously listed.

L Matrix Elements Using Pressure as Dependent Variable ($T_{0,e}$ not assumed constant)

$$l^p_{11} = l_{11} + \frac{1}{2}l_{13}\frac{M_e}{\varrho_e}$$

$$l^p_{12} = l_{12} + l_{13}\frac{M_e}{u_e}$$

$$l^p_{13} = -\frac{1}{2}l_{13}\frac{M_e}{p_e}$$

$$l^p_{14} = l_{14}$$

$$l^p_{15} = l_{15}$$

$$l^p_{21} = l_{21} + \frac{1}{2}l_{23}\frac{M_e}{\varrho_e}$$

$$l^p_{22} = l_{22} + l_{23}\frac{M_e}{u_e}$$

$$l^p_{23} = -\frac{1}{2}l_{23}\frac{M_e}{p_e}$$

$$l^p_{24} = l_{24}$$

$$l^p_{25} = l_{25}$$

$$l^p_{31} = l_{31} + \frac{1}{2}l_{33}\frac{M_e}{\varrho_e}$$

$$l^p_{32} = l_{33}\frac{M_e}{u_e}$$

$$l^p_{33} = -\frac{1}{2}l_{33}\frac{M_e}{p_e}$$

$$l^p_{34} = l_{34}$$

$$l^p_{35} = l_{35}$$

$$l^p_{41} = l_{41} + \frac{1}{2}l_{43}\frac{M_e}{\varrho_e}$$

$$l^p_{42} = l_{42} + l_{43}\frac{M_e}{u_e}$$

$$l^p_{43} = -\frac{1}{2}l_{43}\frac{M_e}{p_e}$$

$$l^p_{44} = l_{44}$$

$$l^p_{45} = l_{45}$$

$$l^{p}_{51} = \frac{1}{2}Au_e^2 - \frac{M_e^2}{\varrho_e}(E_e + p_e)\overline{w}\theta(c_1\overline{H} + c_2)$$

$$l^{p}_{52} = \varrho_e u_e A - 2\frac{M_e^2}{u_e}(E_e + p_e)\overline{w}\theta(c_1\overline{H} + c_2)$$

$$l^{p}_{53} = \frac{A}{\gamma - 1} + \frac{M_e^2}{p_e}(E_e + p_e)\overline{w}\theta(c_1\overline{H} + c_2)$$

$$l^{p}_{54} = l_{54}$$

$$l^{p}_{55} = l_{55}$$

N Matrix Elements Using Pressure as Dependent Variable ($T_{0,e}$ not assumed constant)

$$n^{p}_{11} = n_{11}$$

$$n^{p}_{12} = n_{12}$$

$$n^{p}_{13} = n_{13}$$

$$n^{p}_{14} = n_{14}$$

$$n^{p}_{15} = n_{15}$$

$$n^{p}_{21} = n_{21} + \frac{1}{2}n_{23}\frac{M_e}{\varrho_e}$$

$$n^{p}_{22} = n_{22} + n_{23}\frac{M_e}{u_e}$$

$$n^{p}_{23} = -\frac{1}{2}n_{23}\frac{M_e}{p_e}$$

$$n^{p}_{24} = n_{24}$$

$$n^{p}_{25} = n_{25}$$

$$n^{p}_{31} = n_{31} + \frac{1}{2}n_{33}\frac{M_e}{\varrho_e}$$

$$n^{p}_{32} = n_{32} + n_{33}\frac{M_e}{u_e}$$

$$n^{p}_{33} = -\frac{1}{2}n_{33}\frac{M_e}{p_e}$$

$$n^{p}_{34} = n_{34}$$

$$n^{p}_{35} = n_{35}$$

$$n^{p}_{41} = Au_e^2 - u_e^2 M_e^2\theta\overline{w}(c_1\overline{H} + c_2)$$

$$n^{p}_{42} = 2\varrho_e u_e A - 2\varrho_e u_e M_e^2\theta\overline{w}(c_1\overline{H} + c_2)$$

$$n^{p}_{43} = A + \frac{\varrho_e u_e^2}{p_e}M_e^2\theta\overline{w}(c_1\overline{H} + c_2)$$

$$n^p_{44} = n_{44}$$

$$n^p_{45} = n_{45}$$

$$n^p_{51} = \tfrac{1}{2}Au_e^3 - \frac{u_e}{\varrho_e}M_e^2(E_e + p_e)\overline{w}\theta(c_1\overline{H} + c_2)$$

$$n^p_{52} = A(\varrho_e u_e^2 + E_e + p_e) - 2M_e^2(E_e + p_e)\overline{w}\theta(c_1\overline{H} + c_2)$$

$$n^p_{53} = \frac{\gamma}{\gamma - 1}Au_e + \frac{u_e}{p_e}M_e^2(E_e + p_e)\overline{w}\theta(c_1\overline{H} + c_2)$$

$$n^p_{54} = n_{54}$$

$$n^p_{55} = n_{55}$$

II. Auxiliary Relations

$$H_{\delta^*} = (1 + c_1M_e^2)\overline{H} + c_2M_e^2$$

$$H_{\theta_\varrho} = (c_3\overline{H} + c_4)M_e^2$$

$$(H_{\theta^*})_{M_e=0} = 1.48061 + 3.83781e^{-2\overline{H}} + 0.33 - \frac{1}{8.5484}\tan^{-1}\left[\frac{10^{7-\overline{H}} - 1}{1.23}\right]$$
$$- \left(0.33 - \frac{\pi}{17.1}\right)\tanh^{\frac{1}{2}}\left[(1.2874 \times 10^{-6})(10^{7-\overline{H}})^{1.45761}\right]$$

$$H_{\theta^*} = \frac{(H_{\theta^*})_{M_e=0} + 0.028M_e^2}{1 + 0.014M_e^2}$$

$$\overline{c}_f = \frac{0.3e^{-1.33\overline{H}}}{(\log_{10}\overline{Re}_\theta)^{1.74+0.31\overline{H}}} + (1.1 \times 10^{-4})\left[\tanh\left(4 - \frac{\overline{H}}{0.875}\right) - 1\right]$$

$$\frac{\theta}{\overline{\theta}} = 1 - \frac{0.92M_e^2}{7.09 + M_e^2}\tanh[1.49(\overline{H} - 0.9)]$$

$$\frac{\overline{c}_D}{2} = \frac{\left[-0.01167e^{-0.038\overline{H}^3} + 0.0115 + \frac{\Delta CFD}{1000} + (9.0 \times 10^{-8})e^{1.603\overline{H}}\right]}{(1 + 0.025M_e^{1.4})}$$

Note that in the above relation,

$$\Delta CFD = m\overline{Re}_\theta^n$$
$$m = 650\overline{H} - 743 \qquad \Big\} \qquad \overline{H} \leq 1.6$$
$$n = -1.59\overline{H} + 1.45$$

$$\Delta CFD = m e^{n \overline{Re}_\theta}$$

$$\left. \begin{array}{l} m = 3.25 e^{0.045 \overline{H}^2} \\[2mm] n = \dfrac{\overline{H}}{10000} - 0.0017 \end{array} \right\} \quad \overline{H} > 1.6$$

where

$$\frac{\mathrm{Re}_\theta}{\overline{\mathrm{Re}_\theta}} = \frac{\overline{c}_f}{\overline{\overline{c}}_f} = f_e^{\frac{1}{2}}$$

III. Details of Navier–Stokes Computational Procedure

The Navier–Stokes simulations of the AGARD transonic nozzle geometry were made by application of the Euler solver developed by Whitfield[24] and Arabshahi[26] modified to include viscous effects. Although this code was developed as a full Navier–Stokes code, streamwise viscous terms were neglected in these two–dimensional simulations.

The basic Euler solver is an implicit, finite–volume, formulation applying Roe's[27] approximate Riemann solver, and the higher–order extensions of Osher and Chakravarthy[28], to compute the inviscid flux terms. The implicit operator is formed using Steger's[29] flux vector splitting with the resulting system of equations inverted by application of Whitfield's[30] two–pass or modified two–pass algorithm. The modified two–pass algorithm was applied in this computation.

Viscous fluxes were added as an explicit source term patterned after the implementation in the PARC3D[21] Navier–Stokes code. The viscous portion of the Reynolds–averaged Navier–Stokes equations can be expressed in nondimensional conservation law form as

$$\frac{1}{\mathrm{Re}} \frac{\partial G_j}{\partial \xi_j}$$

As usual, the Reynolds number, Re, is defined by reference sound speed, length, density, and viscousity. The viscous flux vectors are defined as

$$G_j = J \begin{bmatrix} 0 \\ \tau_{ij} \\ u_k \tau_{jk} - q_j \end{bmatrix}$$

98

where J is the Jacobian of the coordinate transformation. The viscous stress tensor and the heat flux vector are defined as

$$\tau_{ij} = \mu \frac{\partial \xi_j}{\partial x_k}\left[\frac{\partial u_i}{\partial x_k} + \frac{\partial u_k}{\partial x_i}\right] + \lambda \frac{\partial \xi_j}{\partial x_i}\frac{\partial u_m}{\partial x_m}$$

$$q_j = -\frac{K}{(\gamma - 1)P_r}\frac{\partial \xi_j}{\partial x_k}\frac{\partial T}{\partial x_k}$$

The viscous flux is then approximated at each cell face in a series of directional sweeps with the result summed into the residual computed for the original Euler algorithm.

The turbulence model applied is also based upon the algebraic model implemented in the PARC3D Navier–Stokes code. In wall–bounded regions of the flow field, a Baldwin–Lomax[38] algebraic model of turbulent viscosity is applied. In regions not bounded by a solid surface, a vorticity based model, as developed by Thomas[39], is applied. In this algebraic model, viscosity and thermal conductivity are modified as a function of turbulent viscosity as

$$\mu_{total} = \mu + \mu_T$$

$$\frac{K_{total}}{P_r} = \frac{K}{P_r} + \frac{\mu_T}{P_{rT}}$$

$$\mu_T = \mathrm{Re}\varrho l^2 \omega$$

where μ_T is the turbulent viscosity, P_{rT} is the turbulent Prandtl number, l is a turbulent length scale, and ω is the local vorticity.

NOMENCLATURE

a	speed of sound
A	area
b	right–hand–side vector
c_f	skin friction
c_v	constant volume specific heat
C	function used in dissipation model; also used as constant for inflow boundary conditions
D	dissipation integral
e	internal energy
E	total energy
f	scalar function
F	vector function
G	function used in dissipation model; also denotes viscous flux vector
h	channel half–height
$\overline{H}$	"incompressible" shape factor $\overline{\delta^*}/\overline{\theta}$
H_{δ^*}	shape factor, δ^*/θ
H_{θ_ϱ}	shape factor, θ_ϱ/θ
H_{θ^*}	shape factor, θ^*/θ
K	thermal conductivity
L	temporal derivative coefficient matrix
ℓ_{ij}	$(ij)^{th}$ element of L matrix
M	Mach number
N	spatial derivative coefficient matrix
N_{max}	total number of grid points
n_{ij}	$(ij)^{th}$ element of N matrix
p	pressure
Pr	Prandtl number
q	dependent variable vector; also denotes heat flux vector in Navier–Stokes code
r	function used in dissipation model
R	radius; also used to denote perfect gas constant
Re	Reynolds number
t	time coordinate
T	temperature
u	velocity
u_τ	friction velocity ($u_\tau^2 = \tau_w/\varrho$)

x	axial coordinate; also used to denote dependent variable in Section III.a
y	coordinate normal to wall
y^+	boundary–layer coordinate $\left(y^+ = \dfrac{\varrho y u_\tau}{\mu}\right)$
γ	ratio of specific heats
δ^*	displacement thickness
$\overline{\delta^*}$	"incompressible" displacement thickness
δ_u^*	$\overline{\delta^*}$
Δ	forward difference operator
∇	backward difference operator
θ	momentum thickness
$\overline{\theta}$	"incompressible" momentum thickness
θ^*	energy thickness
θ_ϱ	density thickness
λ	eigenvalue; also denotes second coefficient of viscosity
μ	absolute viscosity
ν	CFL number
ξ	parameter used in grid stretching; also denotes curvilinear coordinate used in Navier–Stokes code
ϱ	density
τ	shear stress
ϕ	function used in dissipation model
ω	vorticity

Subscripts

e	boundary–layer "edge", or inviscid core value
i	axial index
m	iteration parameter
max	denotes a maximum value
n	denotes the nth equation or dependent variable; also denotes time level
ref	reference condition
T	denotes a turbulent quantity
0	stagnation condition
w	wall
∞	reference condition

Superscripts

k	0 for planar flow, 1 for axisymmetric

101

M   signifies Mach number used as dependent variable and $T_{0,e} \neq$ constant

p   signifies pressure used as dependent variable and $T_{0,e} \neq$ constant

$\wedge$ dimensional quantity